論文 / 著書情報
Article / Book Information

題目(和文)	
Title(English)	Plasma Synthesis of Freestanding Doped Silicon Nanocrystals and Their Optical Properties
著者(和文)	ZHOUSHU
Author(English)	Shu Zhou
出典(和文)	学位:博士（工学）, 学位授与機関:東京工業大学, 報告番号:甲第10312号, 授与年月日:2016年9月20日, 学位の種別:課程博士, 審査員:野﨑 智洋,平田 敦,赤坂 大樹,因幡 和晃,山本 貴富喜
Citation(English)	Degree:, Conferring organization: Tokyo Institute of Technology, Report number:甲第10312号, Conferred date:2016/9/20, Degree Type:Course doctor, Examiner:,,,,
学位種別(和文)	博士論文
Type(English)	Doctoral Thesis

Plasma Synthesis of Freestanding Doped Silicon Nanocrystals and Their Optical Properties

A DISSERTATION
SUBMITTED TO THE FACULTY OF THE GRADUATE SCHOOL OF
SCIENCE AND ENGINEERING
OF TOKYO INSTITUTE of TECHNOLOGY
BY

Shu Zhou

IN PARTIAL FULFILLMENT OF THE REQUIREMENTS
FOR THE DEGREE OF
DOCTOR OF ENGINEERING

Advisor
Prof. Tomohiro Nozaki

June 2016

Abstract

Doping bulk silicon (Si) has greatly contributed to the development of semiconductor industry in the past few decades. Given the critical role that dopant plays in bulk Si, doping is expected to be promising in designing the properties of Si nanocrystals (NCs) in addition to tuning the NC size and surface chemistry. Here we employ an integrated nonthermal plasma system to doping freestanding Si NCs with Boron (B) and Phosphorous (P), which are actually the most employed acceptor and donor impurity in Si materials. We demonstrate that Si NCs can be hyperdoped to a concentration exceeding the solubility limits of B and P in Si by plasma. Tuning the dopant concentration in a fairly wide range is achieved by adjusting the fractional flow rate of dopant precursor in the plasma. The dopant-concentration-dependent optical properties of B- and P-doped Si NCs are investigated. It is found that both B- and P- doped Si NCs can exhibit tunable localized surface plasmon resonance in the mid-infrared range. Different from P-doping, the B-doping also leads to apparent redshift of both the direct and indirect optical absorption of Si NCs. The B-doping provides long term colloidal stability in air, which is not observed in P-doped Si NCs. Finally, we develop a cost-effective method to synthesize freestanding doped Si NCs by using economical and safe precursors and employ these Si NCs in organic/inorganic hybrid photovoltaics.

Acknowledgements

There are so many people I have to thank during my study in Tokyo Tech. This thesis would not be finished without their egoless contributions.

Firstly, I would like to thank my advisor Prof. Nozaki for his superb mentorship and guidance over the years. Despite the strong assistance in research, I am also grateful for his kind support of my life when I first come to Tokyo.

Additionally, I want to acknowledge Prof. Murakami from department of mechanical science and engineering, Prof. Matsumoto from department of polymer science and engineering, Prof. Yoshihisa Sei from the analysis support center of Tokyo Tech for providing research equipment and assistance in the measurements which are surely important for the completion of this thesis.

It is really a pleasure for me to have the experience working in Prof. Nozaki's laboratory. I would like to thank Dr. Ding Yi who has worked as a postdoctoral scholar in Nozaki Lab during my time in Tokyo Tech. I also want to highly appreciate the excellent fellow members of Nozaki Lab, Michihiro Sugaya, Seigo Kameshima, Keishiro Tamura, Kaori Iwazumi, Firman B. Juangsa, Yasunori Asano, Ryo Mizukami, Yoshiki Mori, Lukman A. Prananto, Yoshiki Muroya, Takumi Yamazaki and Naoaki Koda for assistance in both experimental research and courses study. I will keep all the warm scenes we stay together in my find.

This thesis is made possible by a fruitful collaboration with Prof. Deren Yang and Prof. Xiaodong Pi from Zhejiang University of China. Besides, I have also collaborated with Prof. Shiomi from the University of Tokyo and Prof. Christophe Delerue from the CNRS of France. The professors together with their students are greatly acknowledged for their contributions to this thesis.

I greatly appreciate my thesis examination committee: Prof. Tomohiro Nozaki, Prof. Atsushi Hirata, Prof. Hiroki Akasaka, Prof. Takatoki Yamamoto and Prof. Kazuaki Inaba for reading this long document.

To my best family, dear Mom and Dad, I know you will always understand me whatever decision I have made. I would never be the person I am without your continuous support and encouragement.

Shu Zhou

June 2016

Tokyo Tech

Table of Contents

List of Figures

List of Tables

List of Publications

1. S. Zhou, Z. Y. Ni, Y. Ding, M. Sugaya, X. D. Pi and T. Nozaki, "Ligand-Free, Colloidal, and Plasmonic Silicon Nanocrystals Heavily-Doped with Boron". *ACS Photonics,* 3, 415-422, (2016).

2. Y Ding, S Zhou, F B Juangsa, M Sugaya, X Zhang, Y Zhao and T Nozaki, "Double-parallel-junction hybrid solar cells based on silicon nanocrystalsn". *Organic Electronics*, 30, 99-104, (2016).

3. Z. Y. Ni, X. D. Pi, S. Zhou, T. Nozaki, B. Grandidier and D. Yang, "Size-dependent Structures and Optical Absorption of Boron-Hyperdoped Silicon Nanocrystals". *Advanced Optical Materials,* 4, 700-707, (2016).

4. Y. Ding, S. Zhou, F. B. Juangsa, M. Sugaya, X. Zhang, Y. Zhao and T. Nozaki, "Optical, Electrical and Photovoltaic Properties of Silicon Nanoparticles with Different Crystallinity". *Applied Physics Letters,* 107, 233108, (2015).

5. S. Zhou, X. D. Pi, Z. Y. Ni, Y. Ding, Y. Y. Jiang, C. H. Jin, C. Delerue, D. Yang and T. Nozaki, "Comparative Study on the Localized Surface Plasmon Resonance of Boron- and Phosphorous-Doped Silicon Nanocrystals". *ACS Nano,* 9, 378-386, (2015).

6. Y. Ding, R. Gresback, S. Zhou, X. D. Pi and T. Nozaki, "Silicon Nanocrystals Synthesized by Very High Frequency Nonthermal Plasma and Their Application in Photovoltaics". *Journal of Physics D: Applied Physics*, 48, 314011-314017, (2015).

7. A. Miura, S. Zhou, T. Nozaki and J. Shiomi, "Crystalline-Amorphous Hybrid Nanostructures for Bulk Silicon Thermoelectric Materials with Very Low Thermal Conductivity", *ACS Applied Materials & Interfaces,* 7, 13484-13489, (2015).

8. S. Zhou, X. D. Pi, Z. Y. Ni, Q. B. Luan, Y. Y. Jiang, C. H. Jin, T. Nozaki and D. Yang, "Boron- and Phosphorus-Hyperdoped Silicon Nanocrystals", *Particle and Particle Systems Characterization, 32, 213-221* (2015).

9. Z. Y. Ni, X. D. Pi, M. Ali, S. Zhou, T. Nozaki and D. Yang, "Freestanding Doped Silicon Nanocrystals Synthesized by Plasma", *Journal of Physics D: Applied Physics,* 48, 314006-314019, (2015).

10. Y. Ding, R. Gresback, Q. M. Liu, S. Zhou, X. D. Pi and T. Nozaki, "Silicon Nanocrystal Conjugated Polymer Hybrid Solar Cells with Improved Performance", *Nano Energy*, 9, 25-31 (2014).

11. S. Zhou, Y. Ding, X. D. Pi and T. Nozaki, "Doped Silicon Nanocrystals from Organic Dopant Precursor by A $SiCl_4$-Based High Frequency Nonthermal Plasma", *Applied Physics Letters*, 105, 183110, (2014).

12. Y. Ding, M. Sugaya, Q. M. Liu, S. Zhou and T. Nozaki, "Oxygen Passivation of Silicon Nanocrystals: Influences on Trap States, Electron Mobility, and Hybrid Solar Cell Performance". *Nano Energy*, 10, 322-328, (2014).

13. Y. Ding, R. Yamada, R. Gresback, S. Zhou, X. D. Pi and T. Nozaki, "Parametric study of Non-thermal Plasma Synthesis of Silicon Nanoparticles from Chlorinated Precursor". *Journal of Physics D: Applied Physics*, 47, 485202-485210, (2014).

Chapter 1: Introduction

1.1 Overview

As the human society steps into information age, semiconductor technology becomes particularly indispensable because of its critical role in advancing the technical innovations in every aspect of modern industry. As one of the most important technical important semiconductors, Silicon (Si) has been widely employed in various fields including microelectronics, integrated circuits and photovoltaics.[1-3] It is well-known that Si is nontoxic and abundant in nature. Si is also easily purified and can be grown defect free single crystal. The excellent mechanical properties and reasonable good electronic properties of Si produce a variety of devices with excellent performance, making Si better positioned than other semiconductors.

Nevertheless, in contrast to its mechanical and electronic properties, the optical property of Si is not so outstanding given the fact that Si is actually an indirect band-gap semiconductor.[4] The inefficient emission and absorption of light seriously limits the advances of Si-based photonics and optoelectronics. However, this can be readily confronted with the rise of nanotechnology because nanomaterial is well regarded to behave vastly different from its bulk form. The most popular term in the nano word is the quantum confinement effect which is essentially due to changes in the atomic structure as a result of direct influence of ultra-small length scale on the energy band structure. Quantum confinements become prominent when the dimension of a semiconductor material is below the Bohr exciton radius of the bulk semiconductor which makes the properties of materials size-dependent. Besides, the surface effect becomes significant when the size of semiconductor materials is reduced down to the nanometer size regime. Engineering the surface should also contribute to the improvement of

nanomaterial properties. Moreover, due to its ready compatibility with modern semiconductor technology, Si nanomaterial holds great promise for integrating high-performance photonic and optoelectronic devices.

1.2 Silicon Nanocrystals

Since the first observation of photoluminescence (PL) of porous Si in the visible range,[5] Si-based nanostructures have received increasing attentions in the past few decades. As one of the most important Si-based nanostructures, Si nanocrystals (NCs) are promising in various fields ranging from optoelectronics to bio-imaging given the abundance and non-toxicity of Si.[6,7] To fully deploy the potential application of Si NCs in these fields, the synthesis of Si NCs is always critical.

Almost all kinds of approaches have been established for synthesizing Si NCs. Tilly et al. report a liquid-phase synthetic approach to produce highly monodisperse Si NCs by reducing $SiCl_4$ with hydride reducing agents in the presence of in anhydrous toluene and tetraocty-lammonium bromide (TOAB).[8] Kauzlarich et al. synthesize Si NCs by reacting SiCl4 with Zintl compound (KSi, Mg_2Si et al.) in ethylene glycol dimethyl ether (glyme).[9] The average NC size depends on the reflux time of Mg_2Si with $SiCl_4$, which provides NCs with an average size of 2-5 nm. Korgel et al. develop a supercritical fluid method to produce various metal and semiconductor nanostructures including nanowires and nanoparticles.[10] The synthesis of Si NCs is carried out by thermally degrading the Si precursor (diphenylsilane) in the presence of octanol at 500 ℃ and 345 bar. Highly crystalline, monodisperse and organic-monolayer passivated Si NCs with an average size ranging from 15 to 40 Å in diameter could be obtained in significant quantities. In contrast to the above-mentioned wet-chemical route, Kortshagen and Wiggers et al.

employed a gas-phase approach to make freestanding Si NCs by plasma.[11,12] The NC size and crystallinity can be controlled by adjusting the residence time in plasma and the power applied to the plasma respectively. CO_2 laser induced pyrolysis of SiH_4 was used to produce silicon nanoparticles by Swihart et al.[13] The average diameter of Si nanoparticles could be controlled down to as small as 5 nm at high rates (up to 200 mg/h).

A great deal of efforts has been made to tailor the properties of the synthesized Si NCs. By reducing the size of Si NCs to less than 5 nm, strong quantum confinement occurs, giving rise to a blue-shift of the bandgap energy of Si NCs, which enables expanding the PL of Si NCs to the whole visible spectrum (Figure 1.1).[14]

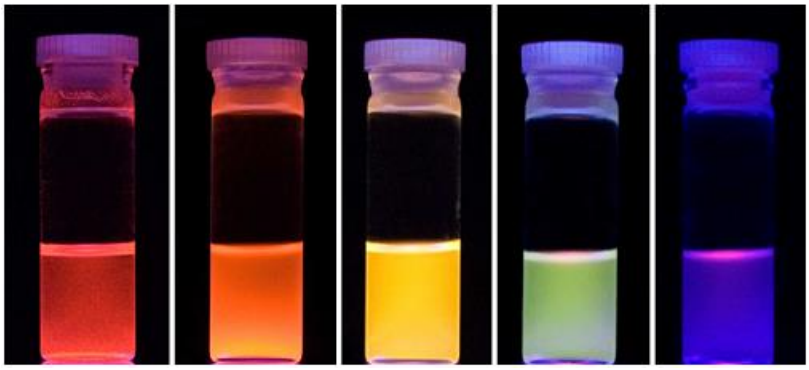

Figure 1.1. Photographs of deep red (740 nm), red (675 nm), yellow (592 nm), green (572 nm) and blue (441 nm) light emission from Si-NCs. [14]

Despite the PL energy, the ability to emit light efficiently is also critical. Through tuning the surface chemistry of Si NCs via functionalization the PL quantum yields of Si NCs could be significantly improved to be above 60%, on par with direct-bandgap semiconductor NCs (Figure 1.2).[16] The functionalization also allows modifying the NC surface to be either hydrophilic or hydrophobic, making them suitable for wet-chemical processing.

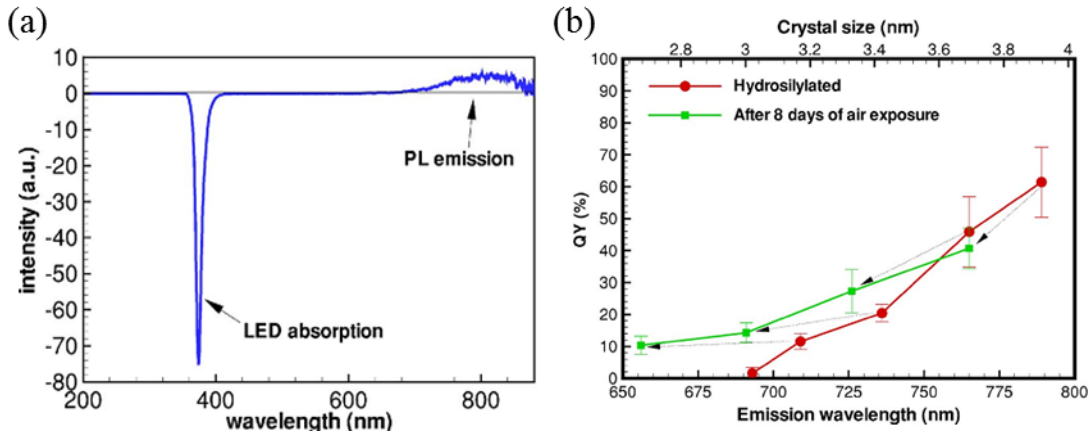

Figure 1.2. (a) Silicon nanocrystal absorption of the 380 nm LED and PL emission. This particular sample has a quantum yield of 62 % ± 11%. (b) Measured PL quantum yields of the air-free hydrosilylated samples measured immediately after wet-chemical reaction（red symbols）and after 8 days of exposure to air. [16]

1.3 Doping Silicon Nanocrystals

In addition to the NC size and surface chemistry, doping serves another promising way in designing the properties of Si NCs. Si NCs may be doped by attaching a molecule or electrochemical cell to the NC surface. Wolf et al. reported p-type doping of Si NCs that are functionalized with NH_4Br or allylamine examined by using scanning tunneling spectroscopy.[17] This p-type behavior is interpreted to be caused by combined contributions of the ligands' dipole moments and charge transfer between a Si-NC and its surface groups. Wheeler et al. have also found heavy doping in Si NCs that are terminated by Cl.[18] Because of the large bond polarization induced by Cl, a hypervalent interaction is induced between the NC surface and hard donor molecules, leading to doping of Si NCs. Nevertheless, the doping level of Si NCs is unlikely to be accurately controlled by the remote doping. However, problem may be confronted by extrinsically inserting impurities into Si NCs. Up to now, a variety of dopants have been employed for doping Si NCs. These dopants can be divided into two categories according to their

energy level positions in Si. Metal impurities with deep energy levels, e.g. erbium, manganese, iron et al., have been used to dope Si NCs for combined properties of Si NCs and the metal dopant.

Er-doped Si NCs that are embedded in glass matrix have been synthesized by sputtering.[19] The Er-doped Si NCs can emit near-infrared PL at around 1.54 μm which corresponds to the absorption minimum in silica-based glass fibers (Figure 1.3).

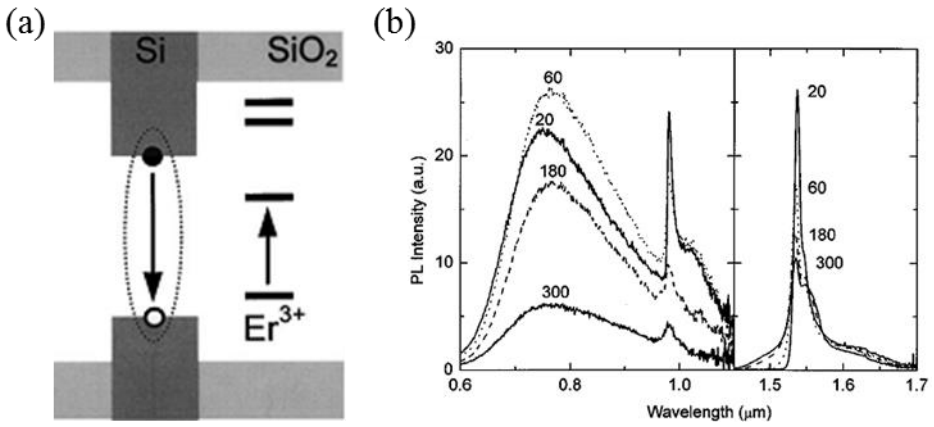

Figure 1.3. (a) Schematic Er excitation model, showing the electronic band structure of Si nanocrystal-doped SiO_2 and the Er 4f energy levels. (b) Photoluminescence spectra at 20, 60, 180, and 300 K showing abroad nanocrystal spectrum in the range 600–1100 nm, and two clear Er luminescence lines at 982 and 1536 nm. [19]

Manganese (Mn)-doped Si NCs have been synthesized by using Mn-doped Zintl salts as precursors via a wet-chemical method.[20] The Mn-doped Si NCs possess combination of paramagnetic and optical properties that do not exist in undoped Si NCs (Figure 1.4).

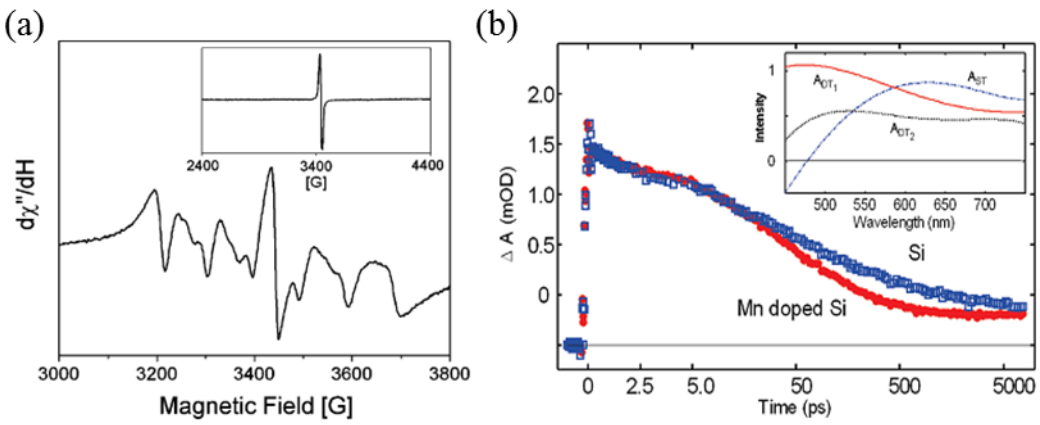

Figure 1.4. (a) EPR spectrum of the Mn^{2+} doped Si nanoparticles. The inset shows EPR spectrum of the undoped Si nanoparticles. (b) Transient absorption spectroscopy probed at 525 nm in Mn-doped Si and undoped Si nanoparticles. [20]

Iron-doped Si NCs have also been synthesized from an iron-doped sodium silicide precursor.[21] The iron-doped Si NCs show strong and stable PL with high quantum yield in water and are also of low toxicity, demonstrating great promise for bio-imaging applications.

Compared with the above-mentioned metal-doped Si NCs, Si NCs that are doped with shallow energy level impurities such as B and P have attracted more attention given the fact that they are actually the most widely employed acceptor and donor impurities in Si materials. The B and P doping not only significantly change the concentration of free carriers that are confined in Si NCs, but also induce localized states (impurity level) in the band gap of Si NCs, giving rise to added freedom in tuning the optical absorption and emission of Si NCs. Significantly, the dopants induced localized states usually result in the red-shift of optical bandgap while quantum confinement effect always causes the bandgap to blue-shift. That means the B- and P-doping essentially enables expanding both the optical absorption and emission of Si NCs to below the bandgap of bulk Si for broadband light harvesting across the whole solar spectrum which is

particularly demanded in a variety of solar applications such as third generation solar cells.

Doped Si NCs are either freestanding or embedded in a matrix. Here we will mainly focus on freestanding Si NCs that are doped with B and P.

1.4 Freestanding Boron- and Phosphorous-Doped Si NCs

1.4.1 Synthetic Methods

The doping of Si NCs is usually adapted from the synthesis of intrinsic Si NCs by including the dopant precursors into the synthesis system. For preparing freestanding doped Si NCs, gas precursors are frequently used. Wiggers et al. employ a micro-plasma reactor to make freestanding P-doped Si NCs.[22] In this synthesis approach, the Si precursor (SiH_4) and dilute gases (Ar and H_2) are injected into the reaction chamber together with dopant gas (PH_3). The microwave energy is used to ignite the plasma and NCs are formed by nucleation and growth processes in the plasma. Except micro plasma, Kortshagen et al. synthesize freestanding B- and P-doped Si NCs by using nonthermal plasma. Figure 1.5 schematically shows a nonthermal plasma reactor with a digital image of the Ar-SiH_4 plasma for synthesizing freestanding intrinsic Si NCs.[11] By introducing dopant precursors (e.g. B_2H_6 and PH_3) into the Ar-SiH_4 plasma, freestanding doped Si NCs can be readily obtained. Control over the crystallinity, size and doping level of Si NCs is achieved by modulating the power coupled into plasma, the residence time of NC in plasma and fractional flow rate of dopant precursor, respectively.[23]

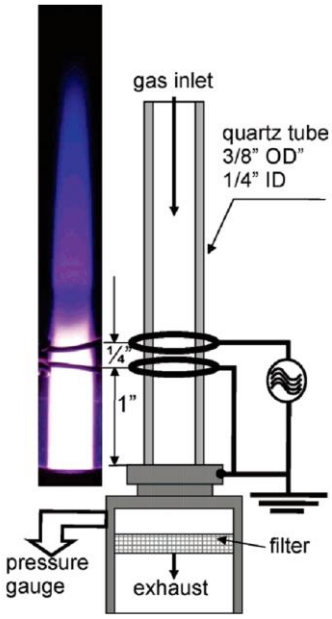

Figure 1.5. Schematic of the nonthermal plasma reactor with a digital image of the argon-silane plasma. [11]

1.4.2 Optical Property

Doping of either B or P impurities will quench the optical emission of Si NCs because of the strong Auger interaction between photo-excited carriers and those induced by doping. Besides, the size mismatch between a dopant and a Si atom causes considerable strain in doped Si NCs, which may further quench the light emission from Si-NCs. Figure 1.6 shows the influence of B and P doping on the PL of freestanding Si NCs with diameters of about 3.6 nm.[23] The PL intensity of Si NCs decreases with increasing B concentration, suggesting strong Auger recombination and strain-induced defect states in B-doped Si NCs. Different from B doping, the PL intensity of Si-NCs initially increases when the concentration of P is small, e.g. 0.06%. The enhancement of the PL intensity may suggest a P atom would first passivate the dangling bond at the surface of a Si NC, which is believed to be the non-radiative recombination center of the Si NC. It is worth to note that, in contrast to B, strain-induced defect states may be negligible in P-doped Si NCs because the atomic size difference between P and Si is small. When the

concentration of P exceeds 0.4%, the PL intensity starts to decrease because of the P-doping induced Auger recombination.

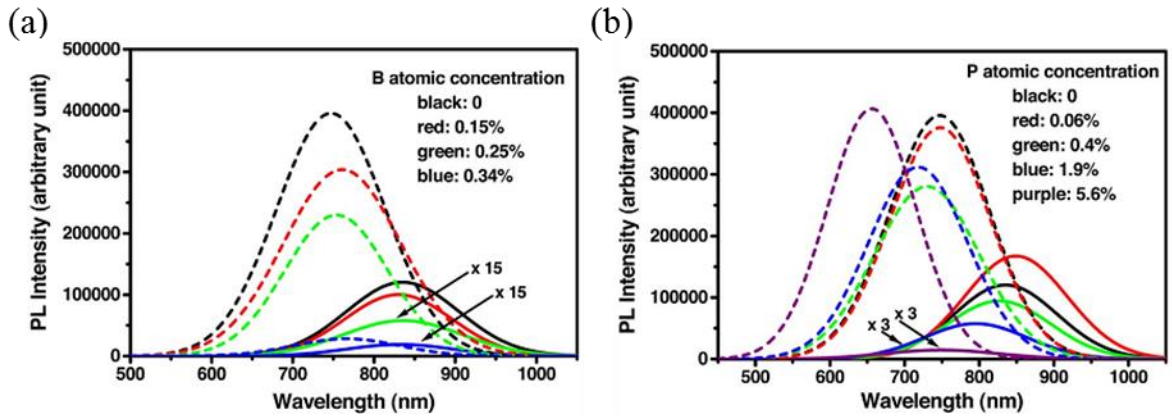

Figure 1.6. (a) PL spectra from as-synthesized intrinsic and B-doped Si-NCs (solid lines) and the same Si-NCs after five-day exposure to air at room temperature (dashed lines). The B-doped Si-NCs are labeled according to B atomic concentrations obtained from ICP-AES measurements. The intensity of PL from as-synthesized Si-NCs with B concentrations of 0.25% and 0.34% is magnified by a factor of 15. (b) PL spectra from as-synthesized intrinsic and P-doped Si-NCs(solid lines) and the same Si-NCs after five-day exposure at air at room temperature (dashed lines). The P-doped Si-NCs are labeled according to P atomic concentrations obtained from ICP-AES measurements. The intensity of PL from as-synthesized Si-NCs with P concentrations of 1.9% and 5.6% is magnified by a factor of 3. [23]

Compared with single B or P-doped Si NCs, the Auger quenching of the PL may be impaired when B and P impurities are doped simultaneously and compensated. PL below the band gap energy of bulk Si crystal is observed in B and P co-doped Si NCs, providing alternative route to tailor the PL energy of Si NCs without losing the intensity very much. By combining the impurity control with the quantum confinement effect, i.e., the size control, the energy range of photoluminescence can be widely extended from infrared to visible range.[24]

1.4.3 Electronic Property

It is well known that only dopants that are electrical activated can produce free carriers in Si NCs. The electrical activity of B in Si NCs can be investigated by means of Fano effect, which concerns the coupling between discrete optical phonons and the continuum of interband hole excitation in p-type Si. Raman scattering measurements allows the direct observation of Fano broadening of Si optical phonon peaks caused by B doping in Si NCs. Figure 1.7(a) shows the Raman spectra for both undoped and B-doped Si NCs that are embedded in a SiO_2 matrix.[25] The Si optical phonon peak at ~519 cm^{-1} for undoped Si NCs shows an asymmetric spectral shape with a long tail toward the low wavenumbers due to the phonon confinement effect. By contrast, the Si optical phonon peak is broadened toward high wavenumbers after B doping because of the Fano effect. In addition to the Fano broadening, two peaks at ~618 and 640 cm^{-1}, which can be assigned to the local vibrational modes of ^{11}B and ^{10}B in Si crystal, were identified only for the B-doped Si NCs (Figure 1.7(b)). The intensity ratios of these two peaks is usually calculated to be approximately 4:1, corresponding to the natural abundance of two isotopes of ^{11}B (80.2%) and ^{10}B (19.8%). The Fano broadening also dependents on the excitation wavelength employed in the Raman measurements. They are both characteristics of Fano effect. The Raman results directly evidence that B atoms are heavily doped into the substitute site of Si NCs and electrically activated in Si NCs.

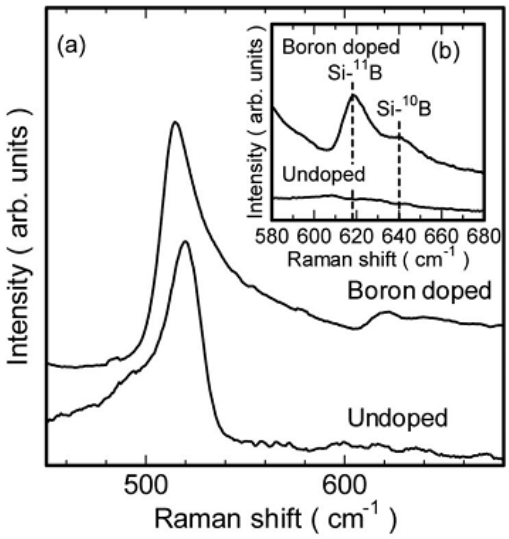

Figure 1.7. (a) Raman spectra for undoped and B-doped Si NCs. Inset shows the Raman spectra of local vibrational modes of B in undoped and B-doped Si NCs. (b) Raman spectra of Si NCs hyperdoped with B at the concentration of 7% obtained with the excitation of 532 and 785 nm lasers. [25]

The mass of P and Si atoms are very similar, rendering it difficult to detect the local vibrational mode of P atoms in Si NCs by using Raman scattering measurements. However, electron spin resonance (ESR) is a sensitive method to probe single electron states, e.g. P donors and conduction electrons, in P-doped Si NCs. Figure 1.8 shows the ESR spectra for both undoped and P-doped Si NCs.[26] The spectrum of undoped Si NCs displays a single broad resonance centered at g=2.006, due to the non-bonding electrons on the three-coordinated Si atoms, named Si dangling bonds at the NC surface. For the Si-NCs doped with $P=1.3\times10^{18}$ cm^{-3}, a resonance centered at g=1.998 originating from the exchange-coupled P atoms at the substitutional sites of a Si-NC core appears. Besides, a pair of lines, denoted [hf(^{31}P)], located symmetrically at the high and low field side of the g=1.998 resonance with a magnetic field splitting of 4.1 mT are observed. This is the typical hyperfine signature of substitutional P in crystalline Si (c-Si), where the Zeeman states of the donor electron are split by interaction with

the ^{31}P nucleus (I =1/2). The P-related EPR resonances clearly evidence the existence of substitutional P atoms that are electrically activated in Si NCs.

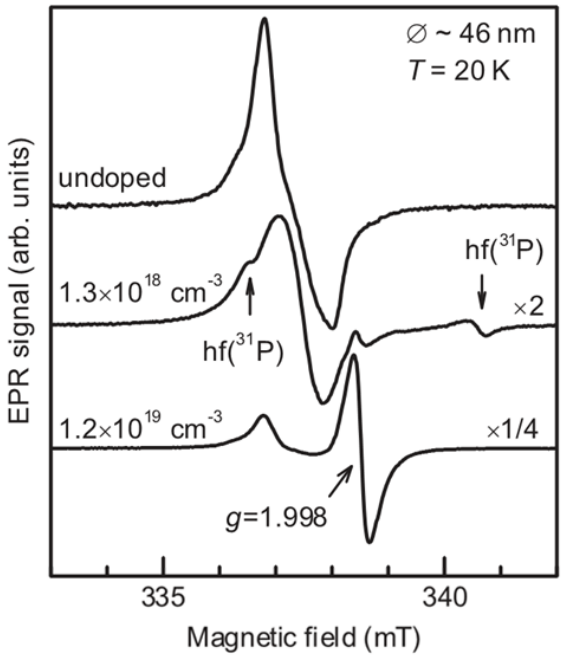

Figure 1.8. EPR spectra of Si NCs with a mean diameter of 42 and 43 nm, and nominal doping concentrations of $[P]_{nom}$ =1.2×10^{19} cm^{-3} and $[P]_{nom}$ = 1.3×10^{18} cm^{-3}, respectively. The spectrum was measured at T=20 K and their intensity was normalized to the sample mass. [26]

The dopants that are electrically activated in Si NCs give rise to extra free carriers which act a critical role in electronic conductivity of the assembly Si NC films. Understanding the doping effect on the electronic transport of Si NC films is fundamental for any future application. A study on the temperature dependence of the dark conductivity for freestanding Si NCs with various P doping concentrations shows that an increase of the P doping concentration results in an increase of the Si NC film dark conductivity and in a decrease of the conductivity temperature dependence. The P donors are found to contribute to dark conductivity of the Si NC films via spin-dependent hopping by performing electrically detected magnetic resonance (EDMR)

measurement.[26]

Although many experimental studies have been carried out towards increasing the conductivity of Si NC films by doping, question still remains if the metal-insulator transition (MIT) occurs in doped Si NC films at some critical concentrations of free carriers. According to the well-known Mott criterion the critical electron concentration (n_M) for the MIT in a bulk semiconductor is related to the Bohr radius as

$$n_M a_B^3 \cong 0.02, \tag{1.1}$$

where $a_B = \varepsilon\hbar^2/m^*e^2$ is the effective Bohr radius (in Gaussian units), ε is the dielectric constant of the semiconductor, m^* is the effective electron mass, $\hbar$ is the Planck constant and e is the electronic charge.

By assuming a dense film of semiconductor NCs that touch each other through small facets of radius without any surface ligands that hinder conduction, Reich et al. derive the MIT criterion for such NC film is

$$n_M \rho^3 \cong 0.3g, \tag{1.2}$$

where ρ is the radius of the touching facets, g is the the number of equivalent minima in the conduction band of the semiconductor. According to this criterion MIT occurs in a Si NC film at a critical electron concentration of 5×10^{20} cm^{-3}.

To test this prediction Chen et al. investigate the electron transport in films of ligand-free P heavily doped Si NCs with a mean size of 7.5 nm.[27] As expected from previous discussions, the ohmic conductance (G) of P-doped Si NC films increases almost monotonically as the nominal doping concentration increases, as shown in Figure 1.9(a). The film conductance over the entire range of doping concentration under investigation is found to follow the Efros-Shklovskii (ES) law as

$$G_f \propto \exp\left[-(T_{ES}/T)^{1/2}\right], \tag{1.3}$$

where

$$T_{ES} = \frac{Ce^2}{\varepsilon_r k_B \xi}, \tag{1.4}$$

ξ is the electron localization length, k_B is the Boltzmann constant and C ≈ 9.6 is a numerical coefficient.

From the slope of linear fits for ln$G$ versus $T^{-1/2}$ the characteristic temperature (T_{ES}) could be readily obtained. The localization length ξ for Si NCs doped with various P concentrations can thus be worked out, as shown in Figure 1.9(b). The localization length increases with increasing doping concentration and exceeds the diameter of a NC at n > 1.9×10^{20} cm^3, which indicates the approach to the MIT in P-doped Si NC films.

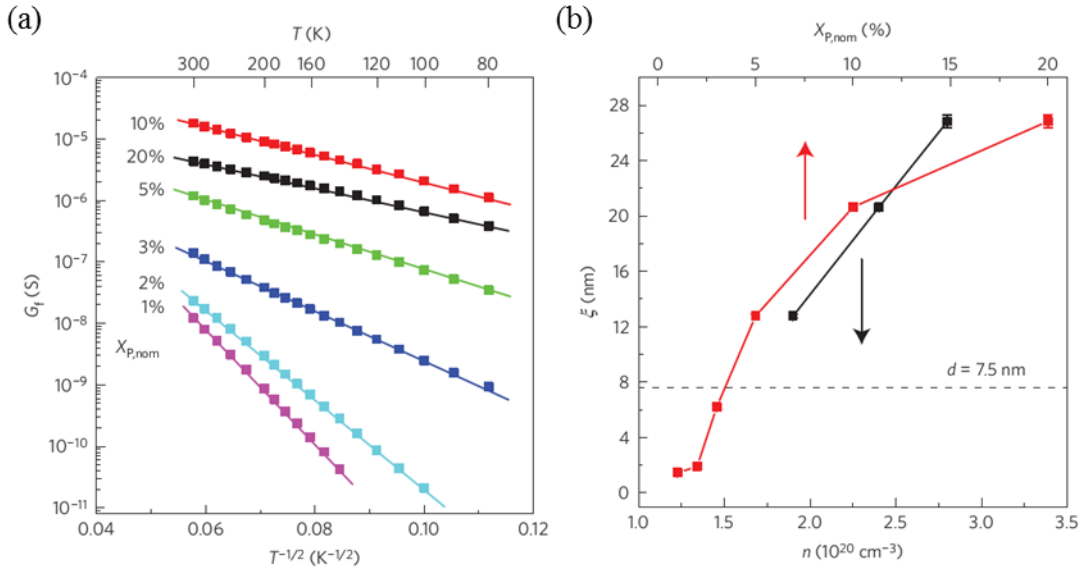

Figure 1.9. Electrical transport in phosphorous-doped Si NC films approaching the metal-to-insulator transition. (a) Temperature dependence of the ohmic conductance for films made from Si NCs at different nominal P doping concentrations. Solid lines are linear fits for each doping concentration. (b) Localization length ξ versus the electron concentration in a NC n and the nominal P doping concentration $X_{P,nom}$. Error bar for each comes from the uncertainty caused by linear fit and is as large as the symbol size. The average

diameter of a NC in films is shown by a horizontal dashed line. [27]

1.5 Scope of this Thesis

This thesis concentrates on freestanding B- and P-doped Si NCs that are synthesized by plasma. For the sake of novel properties enabled by heavy doping, Si NCs doped with very high B and P concentrations will be emphasized. The following chapters will each focus on a different prospect of B- and P-doped Si NCs. Chapters 2-4 are centered on B and P-doped Si NCs that are synthesized from SiH_4 and B_2H_6 or PH_3. Chapter 5 is centered on P-doped Si NCs that are synthesized from $SiCl_4$ and organic dopant precursor (TMP, Trimethyl phosphate).

Chapter 1 provides an introduction to Si NCs as well as the motivation for doping Si NCs with B and P.

Chapter 2 describes the hyperdoping of Si NCs with B and P by a SiH_4-based nonthermal plasma. The dopant concentration, dopant location and doping efficiency have been investigated. The effective doping of B and P is validated by Raman scattering spectroscopy and x-ray photoelectron spectroscopy, respectively. A kinetically-controlled doping model is proposed for the growth of doped Si NCs in plasma, in which collision between Si NCs and B or P atoms and the binding energy of B or P at the NC surface are critical. This chapter is published in Particle and Particle Systems Characterization by S. Zhou, X. D. Pi, Z. Y. Ni, Q. B. Luan, Y. Y. Jiang, C. H. Jin, T. Nozaki and D. Yang. (*Particle and Particle Systems Characterization*, 32, 213-221 (2015))

Chapter 3 discusses the localized surface plasmon resonances (LSPR) arising from free carriers generated by B and P in Si NCs. The LSPR of B-doped Si NCs is demonstrated for the first time and compared with that of P-doped Si NCs by examining the dependence of LSPR

energy on dopant concentration and surrounding medium, and theoretical calculations. Significantly, it has been shown that B-doped Si NCs are better positioned for practical use than P-doped Si NCs for Si-based plasmonics. This chapter is published in ACS Nano by S. Zhou, X. D. Pi, Z. Y. Ni, Y. Ding, Y. Y. Jiang, C. H. Jin, C. Delerue, D. Yang and T. Nozaki. (*ACS Nano, 9, 378-386,* (2015))

Chapter 4 highlights the colloidal stability and interband optical absorption in plasmonic Si NCs heavily-doped with B. Because of the capability of heavily B-doped Si NCs for wet-chemical processing, uniform and dense thin films with plasmonic properties can be inexpensively fabricated by using printing. This is an important progress for employment of plasmonic Si NCs in novel Si-based optoelectronic structures and devices. The shift of the interband optical absorption induced by B heavy doping helps understand the band-structure evolution in B-heavily-doped Si NCs. This chapter is published in ACS Photonics by S. Zhou, Z. Y. Ni, Y. Ding, M. Sugaya, X. D. Pi, and T. Nozaki. (*ACS Photonics,* 3, 415-422, (2016))

Chapter 5 develops a cost-effective gas-phase method to synthesize doped Si NCs by plasma. The precursors employed e.g., $SiCl_4$ and organic phosphate (TMP, Trimethyl phosphate) are both safe and economical compared with conventional precursors such as SiH_4 and PH_3. The main concerns associated with the TMP-enabled-doping of Si NCs have all been addressed. Employments of intrinsic Si NCs and Si NCs doped with P by using TMP in organic/inorganic hybrid solar cells are explored. Portions of this chapter are published in Applied Physics Letters by S. Zhou, Y. Ding, X. D. Pi, and T. Nozaki. (*Applied Physics Letters,* 105, 183110, (2014))

Chapter 6 provides the conclusions of the whole thesis and outlook for future work associated with B- and P-doped Si NCs.

1.6 References

[1] Yu, X.; Chen, J.; Ma, X.; Yang, D. Impurity Engineering of Czochralski Silicon, *Mater. Sci. Eng., R* **2013**, *74*, 1-33.

[2] Soref, R. A. Silicon-Based Optoelectronics, *Proc. IEEE* **1993**, *81*, 1687-1706 (1993).

[3] Green, M. A. Recent Developments in Photovoltaics, *Solar Energy* **2004**, *76*, 3-8.

[4] de Boer, W. D. A. M.; TimmermanD; DohnalovaK; Yassievich, I. N.; ZhangH; Buma, W. J.; GregorkiewiczT. Red Spectral Shift and Enhanced Quantum Efficiency in Phonon-Free Photoluminescence from Silicon Nanocrystals. *Nat. Nanotech.* **2010**, *5*, 878-884.

[5] Cullis, A. G.; Canham, L. T. Visible Light Emission Due to Quantum Size Effects in Highly Porous Crystalline Silicon. *Nature* **1991**, *353*, 335-338.

[6] McVey, B. F. P.; Tilley, R. D. Solution Synthesis, Optical Properties, and Bioimaging Applications of Silicon Nanocrystals. *Acc. Chem. Res.* **2014**, *47*, 3045-3051.

[7] Cheng, K. Y.; Anthony, R.; Kortshagen, U. R.; Holmes, R. J. High-Efficiency Silicon Nanocrystal Light-Emitting Devices. *Nano Lett.* **2011**, *11*, 1952-1956.

[8] Tilley, R. D.; Warner, J. H.; Yamamoto, K.; Matsui, I.; Fujimori, H. Micro-emulsion synthesis of monodisperse surface stabilized silicon nanocrystals. *Chem. Commu.* **2005**, 1833-1835.

[9] Bley, R. A.; Kauzlarich, S. M. A Low-Temperature Solution Phase Route for the Synthesis of Silicon Nanoclusters. *J. Am. Chem. Soc.* **1996**, *118*, 12461-12462.

[10] Holmes, J. D.; Ziegler, K. J.; Doty, R. C.; Pell, L. E.; Johnston, K. P.; Korgel, B. A. Highly Luminescent Silicon Nanocrystals with Discrete Optical Transitions. *J. Am. Chem. Soc.* **2001**, *123*, 3743-3748.

[11] Mangolini, L.; Thimsen, E.; Kortshagen, U. High-Yield Plasma Synthesis of Luminescent Silicon Nanocrystals. *Nano Lett.* **2005**, *5*, 655-659.

[12] Gupta, A.; Swihart, M. T.; Wiggers, H. Luminescent Colloidal Dispersion of Silicon Quantum Dots from Microwave Plasma Synthesis: Exploring the Photoluminescence Behavior Across the Visible Spectrum. *Adv. Fun. Mater.* **2009**, *19*, 696-703.

[13] Li, X. G.; He, Y. Q.; Talukdar, S. S.; Swihart, M. T. Process for Preparing Macroscopic Quantities of Brightly Photoluminescent Silicon Nanoparticles with Emission Spanning the Visible Spectrum. *Langmuir* **2003**, *19*, 8490-8496.

[14] Pi, X. D.; Liptak, R. W.; Nowak, J. D.; Pwells, N.; Carter, C. B.; Campbell, S. A.; Kortshagen, U. Air-Stable Full-Visible-Spectrum Emission From Silicon Nanocrystals Synthesized by an All-Gas-Phase Plasma Approach. *Nanotechnology* **2008**, *19*, 245603.

[15] Jurbergs, D.; Rogojina, E.; Mangolini, L.; Kortshagen, U. Silicon Nanocrystals with Ensemble Quantum Yields Exceeding 60%. *Appl. Phys. Lett.* **2006**, *88*, 233116.

[16] Veinot, J. G. C. Synthesis, Surface Functionalization, and Properties of Freestanding Silicon Nanocrystals. *Chem. Commu.* **2006**, 4160-4168.

[17] Wolf, O.; Dasog, M.; Yang, Z.; Balberg, I.; Veinot, J. G. C.; Millo, O. Doping and Quantum Confinement Effects in Single Si Nanocrystals Observed by Scanning Tunneling Spectroscopy. *Nano Lett.* **2013**, *13*, 2516-2521.

[18] Wheeler, L. M.; Neale, N. R.; Chen, T.; Kortshagen, U. R. Hypervalent Surface Interactions for Colloidal Stability and Doping of Silicon Nanocrystals. *Nat. Commu.* **2013**, *4*, 2197-2206.

[19] Fujii, M.; Yoshida, M.; Kanzawa, Y.; Hayashi, S.; Yamamoto, K. 1.54 μm Photoluminescence of Er^{3+} Doped into SiO_2 Films Containing Si Nanocrystals: Evidence for Energy Transfer from Si Nanocrystals to Er^{3+}. *Appl. Phys. Lett.* **1997**, *71*, 1198-1200.

[20] Zhang, X.; Brynda, M.; Britt, R. D.; Carroll, E. C.; Larsen, D. S.; Louie, A. Y.; Kauzlarich, S. M. Synthesis and Characterization of Manganese-Doped Silicon Nanoparticles: Bifunctional Paramagnetic-Optical Nanomaterial. *J. Am. Chem. Soc.* **2007**, *129*, 10668-10669.

[21] Singh, M. P.; Atkins, T. M.; Muthuswamy, E.; Kamali, S.; Tu, C.; Louie, A. Y.; Kauzlarich, S. M. Development of Iron-Doped Silicon Nanoparticles as Bimodal Imaging Agents. *ACS Nano* **2012**, *6*, 5596-5604.

[22] Stegner, A. R.; Pereira, R. N.; Lechner, R.; Klein, K.; Wiggers, H.; Stutzmann, M.; Brandt, M. S. Doping Efficiency in Freestanding Silicon Nanocrystals from the Gas Phase: Phosphorus Incorporation and Defect-Induced Compensation. *Phys. Rev. B* **2009**, *80*, 165326.

[23] Pi, X. D.; Gresback, R.; Liptak, R. W.; Campbell, S. A.; Kortshagen, U. Doping Efficiency, Dopant Location, and Oxidation of Si Nanocrystals. *Appl. Phys. Lett.* **2008**, *92*, 123102.

[24] Hori, Y.; Kano, S.; Sugimoto, H.; Imakita, K.; Fujii, M. Size-Dependence of Acceptor and Donor Levels of Boron and Phosphorus Codoped Colloidal Silicon Nanocrystals. *Nano Lett.* **2016**, *16*, 2615-2620.

[25] Sato, K.; Fukata, N.; Hirakuri, K. Doping and Characterization of Boron Atoms in Nanocrystalline Silicon Particles. *Appl. Phys. Lett.* **2009**, *94*, 161902.

[26] Stegner, A. R.; Pereira, R. N.; Klein, K.; Lechner, R.; Dietmueller, R.; Brandt, M. S.; Stutzmann, M.; Wiggers, H. Electronic Transport in Phosphorus-Doped Silicon Nanocrystal Networks. *Phys. Rev. Lett.* **2008**, *100*, 026803.

[27] Chen, T.; Reich, K. V.; Kramer, N. J.; Fu, H.; Kortshagen, U. R.; Shklovskii, B. I. Metal-insulator transition in films of doped semiconductor nanocrystals. *Nat. Mater.* **2016**, *15*, 299-303.

Chapter 2: Silicon Nanocrystals Hyperdoped with Boron and Phosphorus*

***** This chapter is adapted from the work published by S. Zhou, X. D. Pi, Z. Y. Ni, Q. B. Luan, Y. Y. Jiang, C. H. Jin, T. Nozaki and D. Yang in Particle and Particle Systems Characterization (*Particle and Particle Systems Characterization*, 32, 213-221 (2015)).

2.1 Abstract

Hyperdoping silicon nanocrysals (Si NCs) to a concentration exceeding the solubility limit of a dopant may enable their novel applications. Here we demonstrate the successful hyperdoping of Si NCs with boron (B) and phosphorus (P), which are the most important dopants for Si. Despite the hyperdoping the diamond structure of Si NCs is hardly modified. There are both electrically active B and P in hyperdoped Si NCs. It is proposed that the hyperdoping is made possible mainly by the kinetics in the nonthermal plasma synthisis of Si NCs. Collision between Si NCs and B or P atoms and the binding energy of B or P at the NC surface are critical to the understanding on the differences in the doping efficiency and dopant distribution between B and P. B-hyperdoping-induced tensile stress needs to be taken into account in the investigation on the doping and oxidation of Si NCs.

2.2 Introduction

As one of the most important semiconductor materials, silicon (Si) needs to be doped for all kinds of technologically important applications whether it is used in its bulk[1-2] or nanometer-sized[3-5] form. The doping of Si is usually carried out under the circumstances of

thermal equilibrium, which makes the concentration of a dopant not to exceed its solubility limit.[6] However, hyperdoping that enables the concentration of a dopant to be larger than its solubility limit has recently emerged as a promising means for designing Si with novel electronic and optical properties. By performing gas immersion laser doping for Si wafers, Bustarret et al.[7] obtained B-hyperdoped Si, which exhibited superconductivity. Se-hyperdoped Si was also prepared by using Si wafers with the assistance of ion implantation and pulsed-laser annealing.[8] The strong sub-bandgap absorption of Se-hyperdoped Si may extend the application of Si to infrared detection and intermediated-band photovoltaics. In the nanometer-sized regime, Al-hyperdoped Si nanowires grown with the vapor-liquid-gas approach have recently been demonstrated, enabling added freedom in the functionalization of Si nanowires.[9] For Si nanocrystals (NCs), it has been realized that localized surface plasmon resonance may occur in P-hyperdoped Si NCs.[10] This should greatly contribute to the development of Si-based plasmonics.[11]

Si NCs are either embedded in a matrix or freestanding. Although hyperdoping may be achieved for Si NCs embedded in a matrix,[12-16] the fact that dopants can be located in both Si NCs and the matrix gives rise to difficulties in the determination of the exact dopant concentration of Si NCs.[17] This disables the further elucidation of the mechanism for the hyperdoping of Si NCs, in contrast to what happened to bulk Si and Si nanowires. Owing to the absence of matrix-induced complication, however, hyperdoped freestanding Si NCs are well positioned for the aforementioned purpose. Up to now, freestanding Si NCs have only been unambiguously hyperdoped with P in nonthermal plasma.[11,18] In this work, we focus on both B- and P-hyperdoped Si NCs produced in nonthermal plasma with an average size (i.e, ~ 14 nm) in the size regime (> 12 nm) that is advantageous for the fabrication of electronic devices.[5] The

differences in the structural and electronic properties between B- and P-hyperdoped Si NCs have been investigated. It is proposed that the hyperdoping of Si NCs with B and P in nonthermal plasma is mainly controlled by kinetics, in which the probability of collision between a Si NC and a B/P atom and the binding energy of Si-B (Si-P) at the NC surface play important roles.

2.3 Experimental Methods

Si NCs were hyperdoped with B and P by introducing B_2H_6 (0.5% in Ar) and PH_3 (0.5% in Ar) into a SiH_4/Ar nonthermal plasma chamber, respectively. The flow rate of B_2H_6 (PH_3) was adjusted in the range from 0.88 (1.77) standard cubic centimeters per minute (sccm) to 15.2 (30.3) sccm, while that of $SiH_4$was maintained at 31.5 sccm. For the synthesis of all the Si NCs the total gas flow rate wasfixed at 3820 sccm, leading to a pressure of ~360 Pa. Plasma was generated with a 13.56 MHz power source and a matching network. The power coupled into the plasma was ~ 200 W.

Si NCs hyperdoped with B (P) initially reacted with KOH in a nickel crucible. The product was transferred to aplastic cup, into which HNO_3 was added to form silicic and boracic (phosphoric) acids. Excessive potassium chloride and potassium fluoride were then added to precipitate potassium fluorosilicate and potassium fluoroborate (fluorophosphate). These precipitates were subsequently hydrolyzed in water, giving rise to the formation of HF. The resulting solution was then treated by a standard NaOH titration method. Phenolphthalein was used to indicate the end of titration. The concentration of Si or B (P) for each sample was finally calculated.

Transmission electron microscopy (TEM) images were taken by FEI Tecnai G2 F20 S-TWIN with an acceleration voltage of 200 kV. High-angle annular dark field (HAADF) scanning TEM and element mapping images were taken by FEI Titan G2 80-200 w/ Chemi STEM with an acceleration voltage of 200 kV. Samples for TEM and HAADF-STEM measuremnets were prepared by drop-coating Si-NC-containing dispersion onto a copper gridcoated with carbon. Each sample was gently heated to evaporate solvent before inserted into the microscope.

X-ray diffraction (XRD) measurements were performed by X'Pert PRO. Si NCs were collected on a glass substrate inside the synthesis system. They were then immediately transferred to an X-ray diffractometer, in which X rays were generated by a Cu Kα source at the voltage of 40 V. A scanning step of 0.016^{o} was used for all the measurements.

Raman spectroscopy measurements were carried out by using Senterra BRUKER. A micro Raman scattering microscope was employed to measure Si NCs immediately after they were synthesized. The excitation was carried out with a 532 or 785 nm laser. The excitation power was 2 mW.

X-ray photoelectron spectroscopy (XPS) measurements were performed by Kratos AXIS Ultra DLD. As-produced Si NCs were first placed on a 5 mm×5 mm carbon-tape-covered aluminum substrate. After ~ 1 hour exposure to air Si NCs were measured by an X-ray Photoelectron Spectrometer. The measurement was performed again after Si NCs were oxidized in air at room temperature for 2 and 11 months.

2.4 Results and Discussion

2.4.1 Dopant Concentration, Dopant Location and Doping Efficiency

The synthesis of Si NCs by means of SiH_4-based nonthermal plasma has been established in the past few years.[19-21] The doping of Si NCs with B (P) may be realized by introducing B_2H_6 (PH_3) into the SiH_4-based nonthermal plasma. In principle, the concentration of B (P) in Si NCs correlates to the ratio of the flow rate (number of moles) of B_2H_6 (PH_3) to that of SiH_4. From the flow rates we can work out the ideal dopant concentration (C_{ideal}) of Si NCs. For the sake of hyperdoping, we have chosen the values of C_{ideal} to be larger than 5%. Chemical titration has been employed to determine the actual dopant concentration (C_{ct}) of Si NCs. Figure 2.1(a) shows the dependence of C_{ct} on C_{ideal}. It is clear that C_{ct} linearly increases with the increase of C_{ideal} for both B and P. The C_{ct} of B (P) is in the range from 6% (1%) to 31% (18%). Since the solubility of B (P) in Si is ~1% (0.3%),[3] the current results demonstrate that Si NCs are indeed hyperdoped with B (P). If we assume that C_{ct}/C_{ideal} is doping efficiency, the doping efficiency of B is significantly larger than that of P (70% vs. 33%). However, previous work on the doping of small (~3 nm) Si NCs shows that the doping efficiency of B is smaller than P. The underlying mechanism will be discussed later.

It is well-known that only dopants residing inside semiconductor NCs may be effective.[22] Therefore, the knowledge on the distribution of B (P) in Si NCs is critical. Figure 2.1(b) shows the comparison for the concentration of B (P) between the chemical titration measurement and XPS measurement (C_{xps}). Since only the surface and near-surface region of a Si NC is examined during the XPS measurement, C_{xps} may approximate to the concentration of B (P) at the NC surface. In contrast, C_{ct} is the average concentration of B (P) without distinguishing the NC surface from the NC core. The fact that C_{xps} is smaller (larger) than C_{ct} for B (P) indicates the

preferential distribution of B (P) in the NC core (at the NC surface). The contrasting preferential distributions of B and P have also been evidenced by the increase (decrease) of the concentration of B (P) after the HF etching of oxide at the NC surface.

To further quantify the preferential distribution of B (P), we have used XPS to measure Si NCs after two months oxidation in air. Within the detection depth of XPS (~ 3 nm)[23] the concentration of B (P) in the surface oxide (C_s) and that in the unoxidized inner part (C_c) can be calculated. We assume that B (P) at the NC surface is all incorporated into the surface oxide after the oxidation of Si NCs. Therefore, C_s/C_c may be used to approximately evaluate the difference in the dopant concentration between the NC surface and the NC core. Figure 2.1(c) shows that the values of C_s/C_c are 1.97, 1.69, 1.28 for Si NCs doped with P at the concentrations of 6%, 10% and 18%, respectively. When Si NCs are doped with B at the concentrations of 13%, 18% and 31%, the values of C_s/C_c are 0.61, 0.44 and 0.35, respectively. It is clear that C_s/C_c decreases with the increase of B (P) concentration. This indicates that larger portion of B (P) atoms enter the NC core as more B (P) atoms are doped. Since B (P) prefers residing in the NC core (surface), the increase of dopant concentration actually makes the distribution of B (P) less (more) uniform.

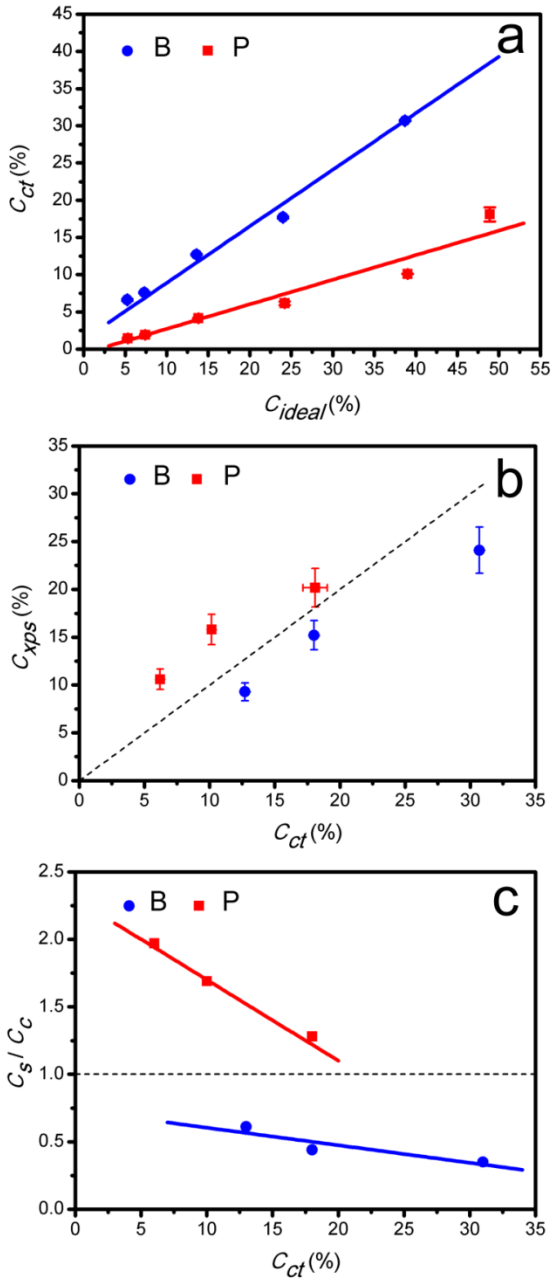

Figure 2.1. (a) Dopant concentration (C_{ct}) measured by chemical titration versus ideal dopant concentration (C_{ideal}) determined by gas flow rates. (b) Dopant concentration (C_{xps}) measured by XPS versus dopant concentration (C_{ct}) measured by chemical titration. The dashed line indicates equivalence between C_{xps} and C_{ct}. (c) Ratio of the concentration (C_s) of dopants in surface oxide to the concentration (C_c) of dopants in the unoxidized inner part within the XPS detection depth for Si NCs that have been oxidized in air for 2 months. The dashed line indicates equivalence between C_s and C_c.

2.4.2 Structure of Hyperdoped Si NCs

Structural characterizations have been carried out to examine if hyperdoping leads to any changes in the crystalline structure of Si NCs. Figure 2.2 shows the typical results of TEM. Low-magnification TEM images (Figure 2.2(a), (d), (g), (j), (m)) demonstrate that sphere-like Si nanoparticles are synthesized whether they are undoped or B/P-hyperdoped. Statistical analyses show that all Si nanoparticles are 12 – 15 nm. The crystallinity of all the Si nanoparticles is evidenced by selective area electron diffraction (SAED) images (Figure 2.2(b), (e), (h), (k), (n)). The lattice fringes of Si NCs can be clearly observed in high-magnification TEM images (Figure 2.2(c), (f), (i), (l), (o)). The lattice spacing *d* of the Si (111) plane can be worked out from both the SAED and high-magnification TEM images. The values of *d* are 0.314, 0.315, 0.314, 0.306 and 0.334 nm for undoped Si NCs and Si NCs doped with 4% P, 18% P, 7% B and 31% B, respectively. It is clear that the hyperdoping of P essentially does not affect the lattice spacing of Si NCs. This should be due to the similarity in the atomic size between P and Si and the substitution of P atoms to Si atoms in P-hyperdoped Si NCs. Given the smaller atomic size of B, the substitution of B atoms to Si atoms may lead to reduction of the lattice spacing. The current reduction of 2.5% for the lattice spacing of the Si (111) plane after Si NCs are doped with 7% B is basically consistent with the Vegard's law. However, when the concentration of B increases to 31%, the lattice spacing of the Si (111) plane is enlarged by 6.4%. We believe that this may result from the formation of interstitial B in the case of enormously hyperdoping Si NCs with B. It is interesting that twining is observed in Si NCs hyperdoped with 31% B and 18% P. Dedicated investigation on the relationship between defects such as twins and hyperdoping for Si NCs should be carried out in the future.

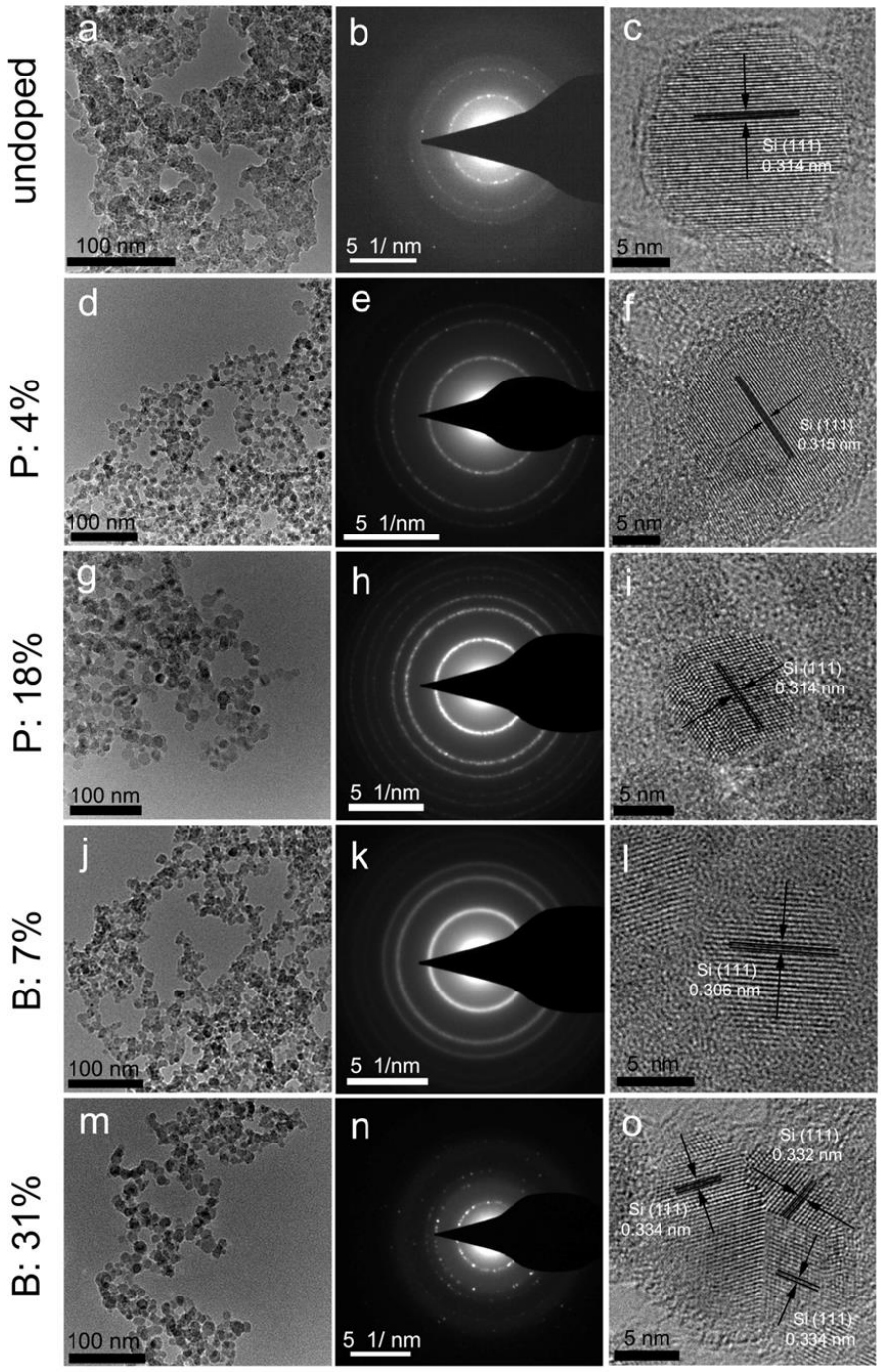

Figure 2.2. Low-magnification TEM images, selective area electron diffraction (SAED) images and high-magnification TEM images of both undoped and hyperdoped Si NCs. (a)-(c) undoped Si NCs; (d)-(f) Si NCs doped with 4% P; (g)-(i) Si NCs doped with 18% P; (j)-(l) Si NCs doped with 7% B and (m)-(o) Si NCs doped with 31% B.

Figure 2.3 shows the high-angle annular dark field (HAADF) scanning TEM images of Si NCs hyperdoped to the highest concentration of B (31%) or P (18%) in the current work. The elements of Si, B and P have been mapped. We see that both B and P elements are associated with the element of Si, indicating that Si NCs have been indeed doped with B or P.

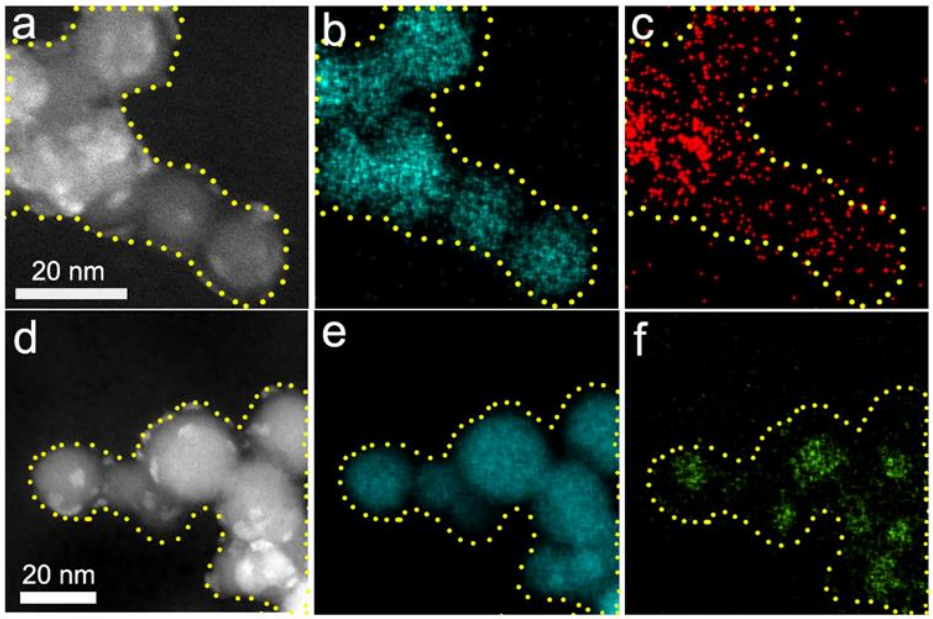

Figure 2.3. (a) HAADF-STEM image of Si NCs hyperdoped with 18% P and corresponding element mapping images of (b) Si and (c) P. (d) HAADF-STEM image of Si NCs hyperdoped with 31% B and corresponding element mapping images of (e) Si and (f) B.

All hyperdoped Si NCs are also measured by using XRD together with undoped ones. It is found that no new phases appear after Si NCs are hyperdoped. This is respresentatively evidenced by the comparison for the XRD patterns between Si NCs hyperdoped to the highest concentration of B (31%) or P (18%) and those undoped, as shown in Figure 2.4(a). All the XRD patterns are characterized by peaks at the 2θ values of 28.4^{o}, 47.3^{o}, 56.1^{o}, 69.1^{o} and 76.4^{o}, which are related to the (111), (220), (311), (400) and (331) diffraction of crystalline Si, respectively.

We conclude that the diamond structure of Si NCs remains after hyperdoping. From the broadening of XRD peaks, we work out that both undoped and hyperdoped Si NCs are ~ 14 nm. This is similar to the results obtained from TEM measurements.

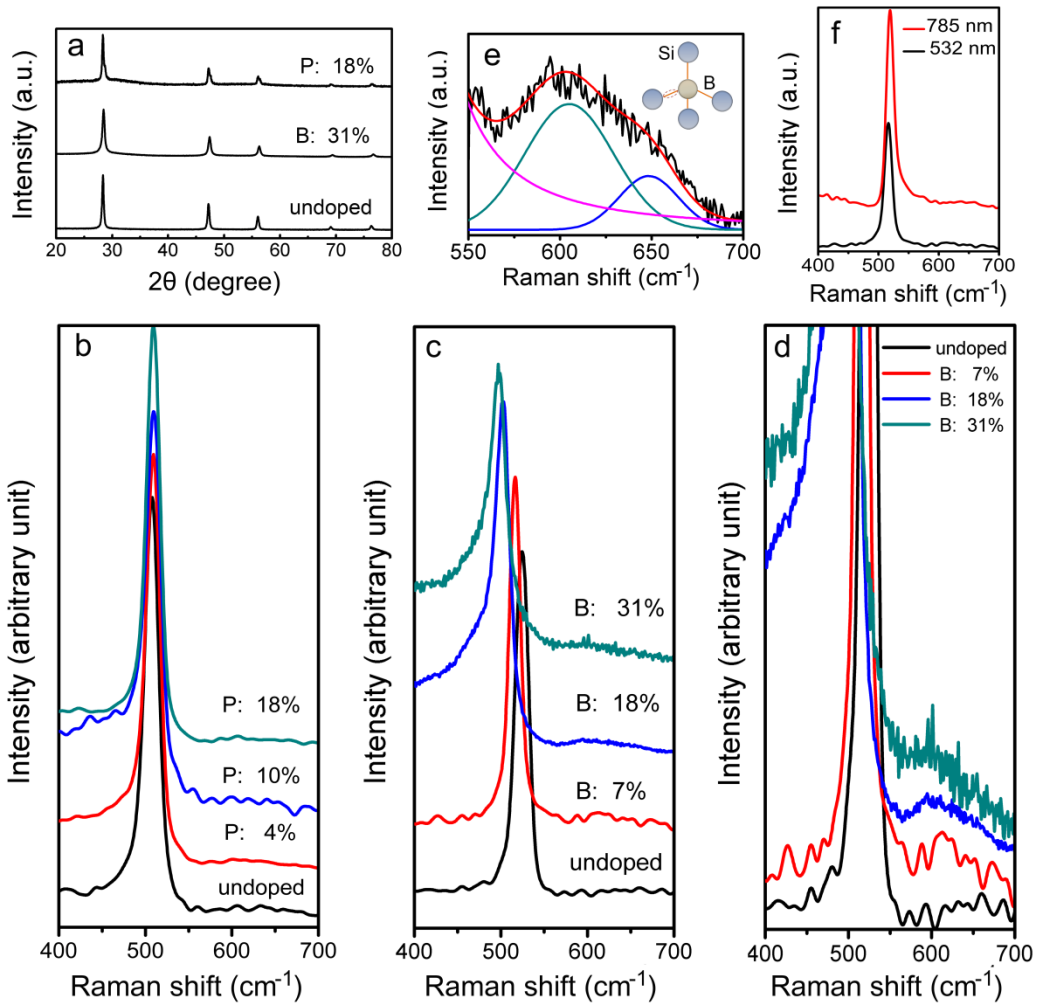

Figure 2.4. (a) XRD spectra of undoped Si NCs,Si NCs hyperdoped with B at the concentration of 31% and Si NCs hyperdoped with P at the concentration of 18%. (b) Raman spectra of undoped Si NCs and Si NCs hyperdoped with P at the concentrations of 4%, 10% and 18%. All the samples are excited by a 532 nm laser. (c) Ramanspectra of undoped Si NCs and Si NCs hyperdoped with B at the concentrations of 7%, 18% and 31%. All the samples are also excited by a 532 nm laser. (d) Results for the normalization of the spectra shown in (c). (e) Decomposition of the Raman signal for Si NCs hyperdoped with B at the concentration of 18%. The

Raman measurement is performed with the excitation of a 532 nm laser.The substitution of B to Si in Si NCs is indicated in the inset. (f) Raman spectra of Si NCs hyperdoped with B at the concentration of 7% obtained with the excitation of 532 and 785 nm lasers.

Figure 2.4(b) shows the Raman spectra of undoped Si NCs and Si NCs hyperdoped with P at the concentrations of 4%, 10% and 18%. It is seen that all these Raman spectra peak at ~520 cm^{-1}, which is the characteristic of the vibration of Si-Si bonds in a Si crystal.[7] The absence of P-hyperdoping-induced changes in the Raman spectroscopy indicates that P hyperdoping leads negligible impact on the structure of Si NCs. Again, this should be due to the similarity of the size of a P atom to that of a Si atom and the excellent substitution of P atoms to Si atoms. In contrast, the Raman peak related to Si-Si bonds redshifts from 520 cm^{-1} to 493 cm^{-1} when Si NCs are hyperdoped with B up to the concentration of 31%. This is shown in Figure 2.4(c). Because of a B atom is significantly smaller than a Si atom, the substitution of a B atom to a Si atom causes neighboring Si-Si bonds to stretch. It is the resulting tensile stress that leads to the redshift of the Raman peak of Si-Si bonds, similar to what Bustarret et al. have observed for B-hyperdoped Si layers.[7] In the meantime, structural distortion induced by tensile stress and aforementioned the formation of interstitial B at a rather high dopant concentration (e. g., ~ 31%) is responsible for the broadening of the Raman peak related to Si-Si bonds toward lower wavenumbers.[7] The tensile stress (ε) of Si–Si bonds can be calculated by using $\varepsilon = \frac{\Delta\omega}{691.2} \times 100\%$, where $\Delta\omega$ is the change of the Raman shift for Si–Si bonds in Si NCs after B doping. We work out that the B-doping-induced tensile stress of Si–Si bonds in Si NCs increases from 0.6% to 3.9% when the B concentration changes from 7% to 31%.

The clear difference between a B atom and a Si atom also enables distinguishable Raman signals of B-Si bonds. By zooming in on the Raman spectra in the range around 600 cm^{-1} for B-hyperdoped Si NCs (Figure 2.4(d), we find Raman signals that may be associated with B-Si bonds. Each of the Raman signals can be decomposed to constituent ones, as representatively shown for the B concentration of 18% in Figure 2.4(e). There are two full constituent peaks at ~ 605 and 648 cm^{-1}. The ratio of the intensity of the 605 cm^{-1} peak to that of the 648 cm^{-1} peak is 3.6, approximately consistent with the natural abundance of ^{11}B and ^{10}B.[24] Therefore, we can state that substitutional B exists in Si NCs, leading to the formation of B-Si bonds (inset of Figure 2.4(e)). It is observed that the Raman peaks related to B-Si bonds redshift when the concentration of B increases from 7% to 31% (Figure 2.4(d)). This is also due to the tensile stress initiated by the large difference in the size between a B atom and a Si atom.

2.4.3 Electrical Activity of Dopants

The electrical activity of substitutional B in Si NCs may be investigated by means of Fano effect,[25] which concerns the coupling between discrete optical phonons and the continuum of interband hole excitation in *p*-type Si. Figure 2.4(f) representatively shows the result for Si NCs hyperdoped with B at the concentration of 7% when the excitation wavelength changes from 532 to 785 nm in the Raman measurement. The Raman peak at 517 cm^{-1} is broadened toward high wavenumbers. An antiresonance dip also appears at the low-wavenumber side of the 517 cm^{-1} peak. They are both characteristic of Fano effect.[24] Similar results have been obtained for other Si NCs hyperdoped with B at the concentrations of 18% and 31%. Therefore, we think that there are B atoms that act as effective acceptors in these Si NCs.

It is well known that hydro-oxygen species play the key role in the oxidation of Si at room temperature. The oxidation of Si follows the Cabrera-Mott mechanism,[26] in which the tunneling of electrons from Si to the surface of oxide is critical. Since the concentration of electrons in Si can be modulated by dopants, dopants may affect the oxidation of Si at room temperature. Therefore, the investigation on the room-temperature oxidation of hyperdoped Si NCs can shed light on the electrical activity of dopants. Figure 2.5 shows the Si 2p XPS results for both undoped and hyperdoped Si NCs after up to 11 months oxidation in air at room temperature. It is found that P significantly enhances the oxidation of Si NCs. Only after 1 hour exposure in air the XPS peak related to the oxidation states of Si emerges for P-hyperdoped Si NCs, in contrast to what happens to undoped Si NCs. With the increase of oxidation time the XPS peak related to Si^0 (99.5 eV) decreases, while the XPS peak related to the oxidation states of Si (100.2 - 104.3 eV) increases. In the meantime the XPS peak related to the oxidation states of Si moves to higher energies. These findings indicate that both undoped and P-hyperdoped Si NCs are progressively oxidized in air. But the XPS peaks related to the oxidation states of Si are clearly much more pronounced with larger energies for P-hyperdoped Si NCs. Therefore, we conclude that P hyperdoping leads to faster oxidation and oxides with more highest oxidation state of Si (Si^{4+}).

The P-hyperdoping-induced significant enhancement of the oxidation of Si NCs implies that P atoms may be effective donors. The concentration of electrons in P-hyperdoped Si NCs is larger than that of undoped Si NCs. A larger concentration of electrons means that more electrons may tunnel through the oxide to reach the surface, ionizing more O atoms. The electric field across the oxide is also stronger, leading to the faster transport of O ions toward the NC core. With the increase of P concentration, the concentration of electrons increases, leading to more significant oxidation. This is evidenced by the increase of the intensity of the peak related

to the oxidation states of Si and the shift of this peak toward higher binding energies (Figure 2.5).

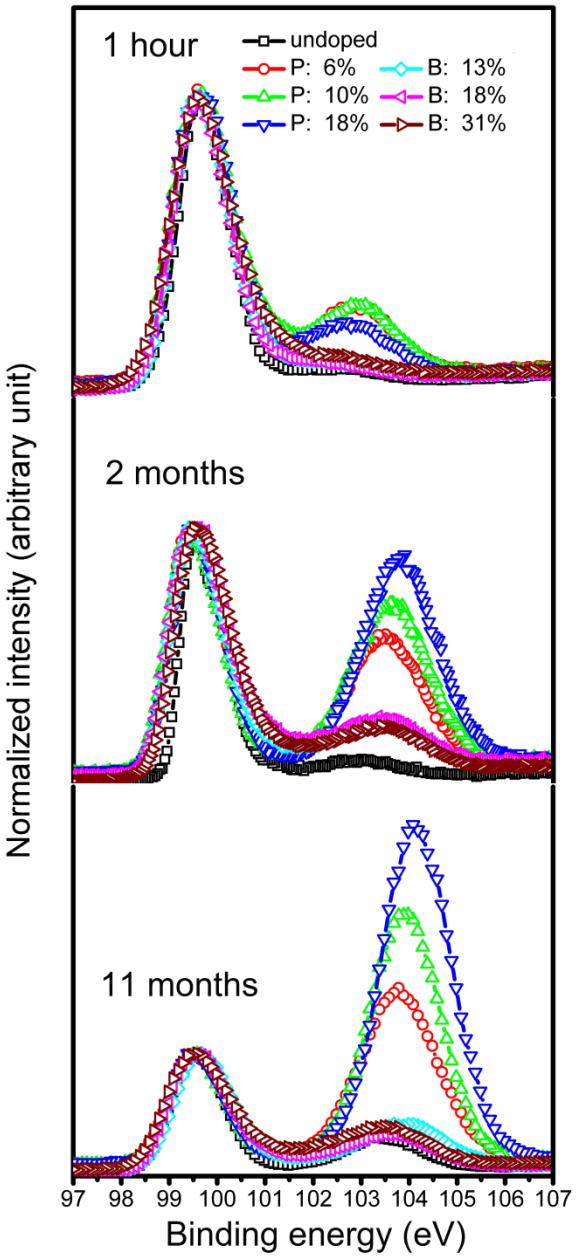

Figure 2.5. XPS spectra of undoped and hyperdoped Si NCs. XPS measurements are carried out after Si NCs are stored in air for 1 h, 2 months and 11 months.The concentrations of P are 6%, 10% and 18%, while those of B are 13%, 18% and 31%.

2.4.4 Oxidation of Hyperdoped Si NCs

For Si NCs that have been exposed in air for 11 months we can work out the quantity of Si in each charge state within the detection depth of XPS by analyzing their XPS spectra. We would like to mention that the influences of fluctuation of the temperature and humidity on each sample are the same because all the samples are stored in the same place and measured at the same time. The results are shown in Table 2.1.

Table 2.1. Atomic fraction of various charge states of Si obtained by analyzing the XPS data for Si NCs that have been oxidized in air for 11 months.

Dopant concentration	N_{Si}^{0}	N_{Si}^{1+}	N_{Si}^{2+}	N_{Si}^{3+}	N_{Si}^{4+}
undoped	0.62	0.14	0	0	0.25
P: 4%	0.46	0.06	0	0.04	0.45
P: 6%	0.25	0.11	0	0	0.64
P: 10%	0.2	0.04	0.02	0	0.73
P: 18%	0.12	0.06	0	0.02	0.8
B: 13%	0.59	0.11	0	0	0.3
B: 18%	0.51	0.19	0	0.1	0.2
B: 31%	0.52	0.16	0	0.11	0.21

The ratio of O to Si in the oxide (x) and the ratio of O to Si within the XPS detection depth (y) can be expressed as

$$x = \frac{\sum_{i=1}^{4} i* \mathrm{N}_{\mathrm{Si}^{i+}}}{2*\sum_{i=1}^{4} \mathrm{N}_{\mathrm{Si}^{i+}}} \tag{2.1}$$

$$\text{and} \qquad y = \frac{\sum_{i=0}^{4} i * \mathrm{N}_{\mathrm{Si}^{i+}}}{2 * \sum_{i=0}^{4} \mathrm{N}_{\mathrm{Si}^{i+}}}, \tag{2.2}$$

where $\mathrm{N}_{\mathrm{Si}^{i+}}$ is the atomic fraction of Si^{i+}.

An oxidized Si NC is schematically shown in Figure 2.6. We can obtain the following equation

$$y = \frac{\frac{\frac{4}{3}\pi\left[\left(\frac{D}{2}\right)^3 - \left(\frac{D}{2}-d\right)^3\right]\cdot\rho_{SiO_x}}{28+16x}}{\frac{\frac{4}{3}\pi\left[\left(\frac{D}{2}-d\right)^3 - \left(\frac{D}{2}-L\right)^3\right]\cdot\rho_{Si}}{28} + \frac{\frac{4}{3}\pi\left[\left(\frac{D}{2}\right)^3 - \left(\frac{D}{2}-d\right)^3\right]\cdot\rho_{SiO_x}}{28+16x}}, \tag{2.3}$$

where D is the diameter of the Si NC, L is the detection depth of XPS, d is the thickness of oxide (SiO_x), ρ_{SiOx} is the density of SiO_x, ρ_{Si} is the density of a Si crystal.

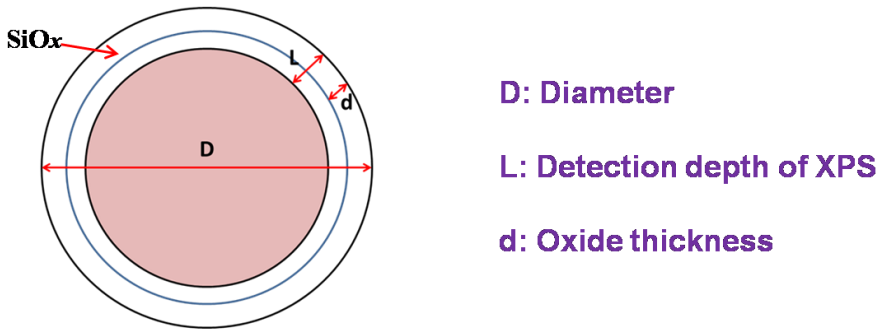

Figure 2.6. Schematic of an oxidized Si NC examined by XPS.

Finally, the oxide thickness can be calculated by using

$$d = \frac{1}{2}\left[D - \sqrt[3]{\frac{28\cdot\rho_{SiO_x}\cdot(x-y)\cdot D^3+(28+16x)\cdot\rho_{Si}\cdot y\cdot(D-2L)^3}{28\cdot\rho_{SiO_x}\cdot(x-y)+(28+16x)\cdot\rho_{Si}\cdot y}}\right]. \quad (2.4)$$

The densities of Si and SiO_2 are 2.33 and 2.20 g/cm^3, respectively. By means of interpolation we obtain that the density of SiO_x is $(2.33-0.06x)$ g/cm^3. In addition, we know that $L \approx 3$ nm[3] and $D \approx 14$ nm. Therefore, the values of d can be readily calculated. The results are shown in Figure 2.7.

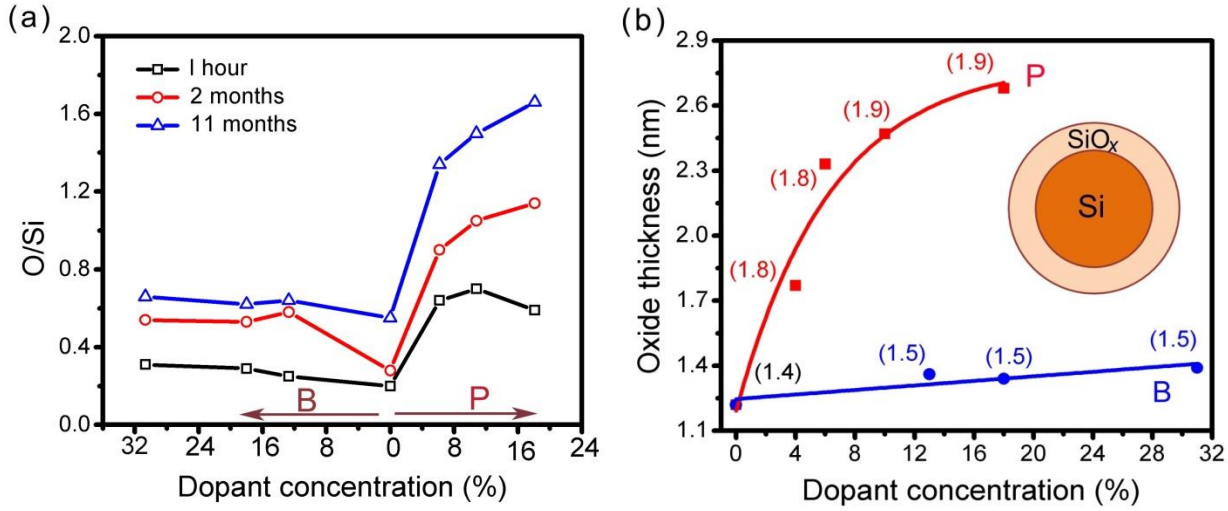

Figure 2.7. (a) Ratio of the number of O atoms to that of Si atoms calculated by using the XPS data shown in a). (b) Thickness of silicon oxide (SiO_x) at the surface of Si NCs that have been oxidized in air for 11 months. The values of x in SiO_x are indicated in the brackets.

As mentioned before, B atoms that act as effective acceptors exist in B-hyperdoped Si NCs. This leads to the fact that electrons are minority carriers in B-hyperdoped Si NCs. The concentration of electrons in B-hyperdoped Si NCs is smaller than that in undoped SiNCs. Therefore, we should expect that the oxidation of B-hyperdoped Si NCs is less significant than that of undoped Si NCs in the framework of the Cambrera-Mott mechanism. However, it is seen that B hyperdoping slightly enhances the oxidation of Si NCs, as evidenced by the more pronounced peak related to the oxidation state of Si in Figure 2.5 and the larger O/Si in Figure 2.7(a) in the comparison with undoping. With the increase of oxidation time or B concentration O/Si increases, although it does not increase as significantly as that for P-hyperdoped Si NCs. The actual slight enhancement of oxidation induced by B hyperdoping should be associated with the tensile stress in B-hyperdoped Si NCs. It is known that the poly-siloxane has usually a helical steric structure, which results in relatively porous and elastic properties. This may induce a void in the NCs and leads to compressive stress at the interface between Si and silicon oxide.[27] The compressive stress that develops during oxidation suppresses the oxidation.[28] Since B-hyperdoping-induced tensile stress is opposite to the oxidation-induced compressive stress,[29] the suppression of the oxidation by compressive stress is mitigated in B-hyperdoped Si NCs. It is clear that this effect prevails over the B-hyperdoping-induced weakening of oxidation in the Cambrera-Mott mechanism. Thus, we have observed the slightly enhanced oxidation for B-hyperdoped Si NCs.

Figure 2.7(b) shows the calculated thickness of silicon oxide (SiO_x), which is formed after 11 months oxidation in air at the surface of undoped and hyperdoped Si NCs. The values of x in the formula of SiO_x are also indicated in the brackets. The process for obtaining these results by use of XPS data is detailed in the Supporting Information. We see that after long-time oxidation

1.2 nm thick $SiO_{1.4}$ is formed at the surface of undoped Si NCs. This thickness is similar to those previously obtained by Li et al.[30] and Stegneret et al.[5] The understoichiometry of surface oxide is characteristic of silicon oxide formed at room temperature.[31,32] P hyperdoping causes both x and the thickness of SiO_x to significantly increase. It appears that P hyperdoping leads to a SiO_x thickness up to 2 times larger than that of undoped Si NCs and the maximum x is 1.9. In contrast, B hyperdoping only gives rise to a rather small increase in the SiO_x thickness. For instance, when Si NCs are hyperdoped with B at the concentration of 31%, the final SiO_x thickness is 1.4 nm, which is only 0.2 nm larger than that for undoped Si NCs. In addition, B hyperdoping just causes x to increase from 1.4 to 1.5. All the above analysis further demonstrates that in the case of hyperdoping B and P vastly differently affect the oxidation of Si NCs.

2.4.5 Doping Mechanism

We now move to discuss the mechanism for the hyperdoping of Si NCs with B and P. The first intriguing question is why Si NCs can be hyperdoped with B or P to concentrations beyond the solubility limit. In this work Si NCs are synthesized in nonthermal plasma, in which the thermal equilibrium between Si NCs and background gas is absent.[33] This may indicates that the doping of Si NCs in nonthermal plasma is mainly controlled by kinetics. Here we assume a simplified kinetic model which is schematically shown in Figure 2.8(a). In this model B or P atoms collide with Si NCs (①) in terms of first-order approximation. The collision may lead to the adsorption of B or P atoms at the surface of Si NCs (②). The adsorbed B or P atoms are then trapped during the subsequent growth of Si NCs (③). Hence, the resulting dopant concentration is basically determined by the frequency of the collision between impurities and Si NCs.

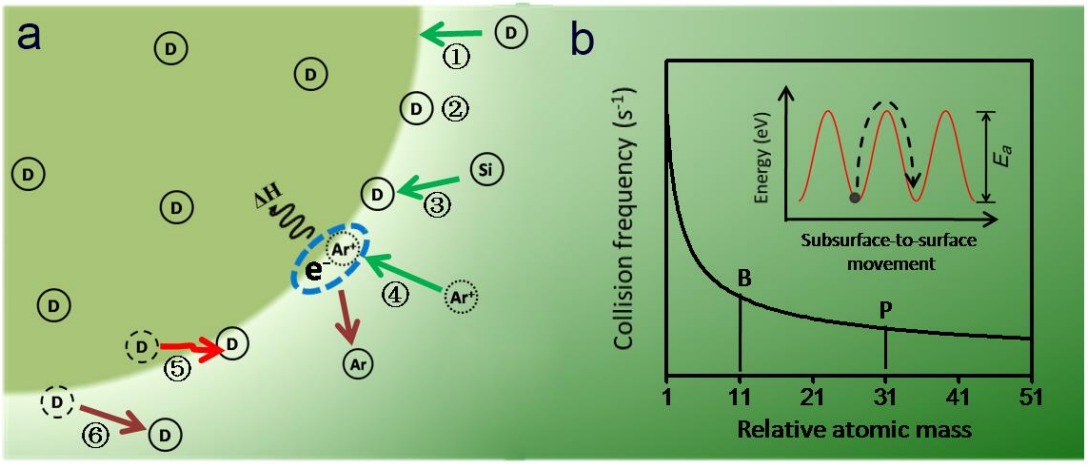

Figure 2.8. (a) Model for the doping of a Si NC in nonthermal plasma. In this model a dopant atom collides with the Si NC (①). The collision may lead to the adsorption of the dopant atom at the surface of the Si NC (②). The adsorbed dopant atom is then trapped during the subsequent growth of the Si NC (③). In nonthermal plasma energy (ΔH) is released when argon ions recombine with electrons at the NC surface (④). It is possible that ajust trapped dopant atom moves to the new NC surface (⑤), which may be called subsurface-to-surface movement. At the NC surface a dopant atom may be dissociated (⑥) because of the bombardment of electrons and ions. (b) Dependence of the frequency of the collision between a Si NC and a dopant atom on the relative atomic mass of the dopant atom. Energy barrier (E_a) for the movement of a dopant atom from subsurface to surface is indicated in the inset.

According to the orbital-motion-limited (OML) theory[34], the frequency of the collision between NCs and charged species is

$$\nu_{e,i} = \begin{cases} n_{e,i} S \sqrt{\frac{k_B T_{e,i}}{2\pi m_{e,i}}} exp(-\frac{q_{e,i}\varphi}{k_B T_{e,i}}), & q_{e,i}\,\varphi \geq 0 \quad (2.5a) \\ n_{e,i} S \sqrt{\frac{k_B T_{e,i}}{2\pi m_{e,i}}} (1 - \frac{q_{e,i}\varphi}{k_B T_{e,i}}), & q_{e,i}\,\varphi < 0 \quad (2.5b) \end{cases}$$

where $v_{e,i}$ is the frequency of the collison between a NC and an electron or ion, $n_{e,i}$ is the electron (ion) density, S is the NC surface area, k_B is Boltzmann constant, $T_{e,i}$ is the electron (ion) temperature, $m_{e,i}$ is the mass of electron (ion), $q_{e,i}$ is the electron (ion) charge, and φ is the NC potential, which is given by

$$\varphi = \frac{eZ}{4\pi\varepsilon_0 r_p}, \tag{2.6}$$

where Z is the number of elementary charge on the NC, e is the elementary charge, ε_0 is the vacuum dielectric constant, and r_p is the NC radius.

By using OML theory, Mangolini et al.[33] modeled the collision of atomic hydrogen with Si NCs and illustrated the energy transfer mechanism in the collision. The collision of NCs with atomic B and P may be modeled in the same way. By assuming that B and P are free of charge we obtain

$$\nu_D = n_D S \sqrt{\frac{k_B T_D}{2\pi m_D}}, \tag{2.7}$$

where n_D is the atomic density of dopant (B or P) in the gas, m_D is the atomic mass of dopant, T_D is the temperature of dopant.

Here we assume that the effective collision efficiency is 100%. Then the number of dopants (N_D) can be calculated by using

$$N_D = \int_0^{t_0} \nu_D \, dt. \tag{2.8}$$

It is well-known that the size of a Si NC strongly depends on the residence time of the Si NC in the synthesis plasma. Figure 2.9 shows the fitting for the dependence of NC size on residence

time by using experimental data collected from the synthesis of Si NCs in SiH_4-based nonthermal plasma.

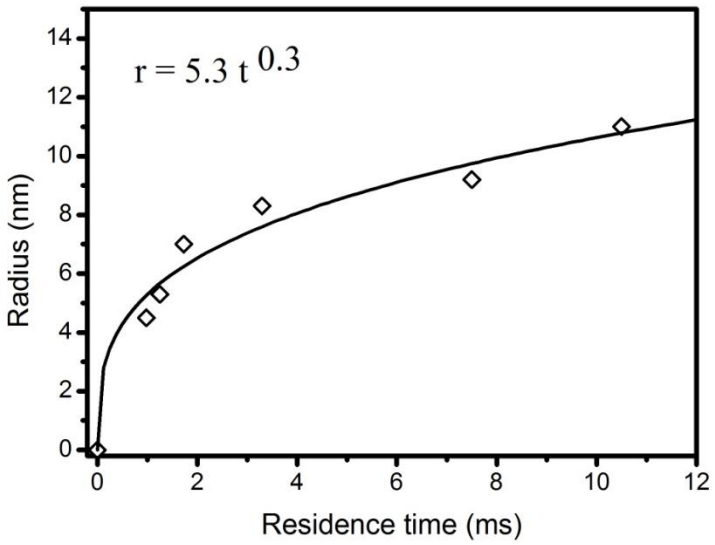

Figure 2.9. Fitting result for the dependence of NC size on residence time.

We obtain

$$r = 5.3t^{0.3}, \tag{2.9}$$

where *t* is the residence time. Thus,

$$dt = 0.014r^{2.3}dr. \tag{2.10}$$

Equation 2.8 can then be rewritten as

$$N_D = \int_0^{r_0} 0.014\, \nu_D r^{2.3}\, dr \tag{2.11}$$

The number (*N*) of atoms in a Si NC is given by

$$N = \frac{4}{3}\pi r^3 \rho_{atom}, \tag{2.12}$$

where ρ_{atom} is the atomic density of Si (5×10^{22} cm^{-3}). Therefore, the dopant concentration (C) can be calculated as

$$C = \frac{\int_0^{r_0} 0.014 \nu_{B,P} r^{2.3} dr}{\frac{4}{3}\pi r^3 \rho_{atom}} = \frac{0.018}{\rho_{atom}} n_D \sqrt{\frac{k_B T_D}{2\pi\, m_D}}\, r^{2.3}. \tag{2.13}$$

Figure 2.8(b) shows the dependence of the collision frequency on the impurity mass in the framework of orbital-motion-limited (OML) theory.[34] It is clear that the collision frequency for B is larger than that for P. For the same size of Si NCs and the same dopant concentration in the gas, the concentration (doping efficiency) of B is calculated to be 1.7 times larger than that of P. Such a result is slightly smaller than that (2.1) obtained from Figure 2.1(a). Since our experiment shows that P atoms prefer the NC surface to the NC core, the trapping of adsorbed P atoms by the subsequent NC growth may be not very efficient. With the assistance of the energy released by ion recombination at the NC surface[20] (④ in Figure 2.8(a), part of just trapped P atoms move to the new NC surface (subsurface-to-surface movement, ⑤ in Figure 2.8(a), where the loss of P atoms to the gas may occur (⑥ in Figure 2.8(a) because of the bombardment of electrons and ions. However, the energy barrier (E_a) for the similar subsurface-to-surface movement (inset of Figure 2.8(b)) of B atoms is larger (3.1 for B vs. 2.7 eV for P).[35] Hence, the trapping of adsorbed dopant atoms by the subsequent NC growth for B-doped Si NCs is more efficient than that for P-doped Si NCs. If this difference is considered, we can then understand the underestimation of the ratio of the B doping efficiency to the P doping efficiency by use of Equation 2.13.

It was previously shown that B doping efficiency was smaller than P doping efficiency for ~ 3 nm Si NCs,[36] in contrast to the current finding for ~14 nm Si NCs. In nonthermal plasma only

very small Si NCs (< 3 nm) undergoes pulsed heating.[33, 37] Since the binding energy of B at the NC surface (i.e, bond strength of Si-B, 2.85 eV) is smaller than that of P at the NC surface (i.e, bond strength of Si-P, 3.64 eV),[38] B atoms are more likely dissociated from the NC surface by the pulsed heating. This may explain why the B doping efficiency is smaller than the P doping efficiency for very small Si NCs. The pulsed-heating-induced B dissociation from the surface of very small Si NCs also accounts for their lower B doping efficiency, when compared with large Si NCs (e.g, current ~ 14 nm Si NCs). We should point out that the P doping efficiency of ~ 14 nm Si NC is smaller than that of ~ 3 nm Si NCs. This may be due to the fact that P atoms preferentially reside at the NC surface. The surface-to-volume ratio of ~ 14 nm Si NCs is smaller than that of ~ 3 nm Si NCs. Therefore, the capacity of accommodating P atoms is weakened when the NC size changes from ~ 3 to 14 nm.

From Equation 2.13 we know that $dC/dr > 0$, indicating that the dopant concentration increases from the NC center to the NC surface. This is not in contradiction to what has been observed for P-hyperdoped Si NCs. However, it does not agree with the fact that the concentration of B in the NC core is higher than that at the NC surface. By means of simulation[39] we find that the average bond length of Si-Si bonds at the NC surface decreases with the increase of the NC size (Figure 2.10), consistent with the change of the surface curvature with the NC size. Because of the shift of the electron cloud of the Si atom shared by the Si-Si bond and Si-B (Si-P) bond toward the Si-Si bond, a shorter Si-Si bond enables a weaker neighboring Si-B (Si-P) bond. This effect may be not serious for a Si-P bond owing to its relatively large bond strength. But a weaker Si-B bond can be affected to be vulnerable enough for the dissociation of B at the NC surface. Therefore, the concentration of B decreases as a NC grows. This leads to the observation of the preferential doping in the NC core for B.

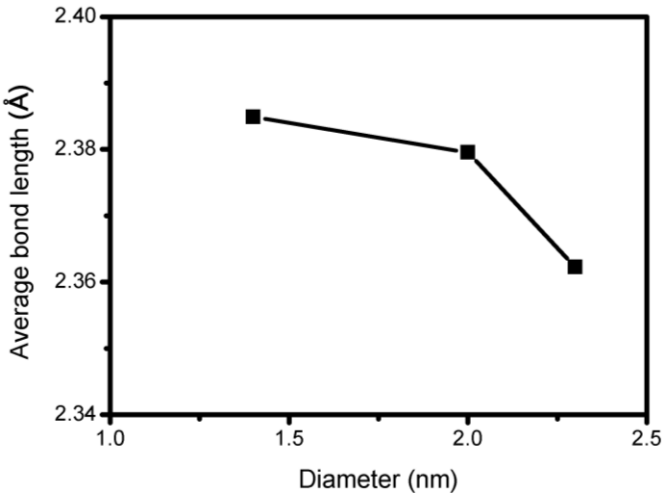

Figure 2.10. Average length of Si-Si bonds at the NC surface for a 1.4, 2.0 or 2.3 nm Si NC.

2.5 Conclusions

In summary, both B- and P-hyperdoped ~14 nm Si NCs have been produced in nonthermal plasma. Despite the hyperdoping the diamond structure of Si NCs remains without the introduction of new phases. The differences in the doping efficiency and dopant distribution between B and P can be understood by assuming that the doping of Si NCs is mainly controlled by kinetics, in which the collision between Si NCs and B or P atoms and the binding energy of B or P at the NC surface are critical. Both B and P may be effective dopants in Si NCs. P-induced electrons enhance the oxidation of Si NCs, leading to thicker and more stoichiometric silicon oxide at the NC surface. B induced holes may weaken the oxidation of Si NCs. However, B-hyperdoping-induced tensile stress helps to relax the oxidation induced compressive stress. This effect is strong enough to actually slightly enhance the oxidation of Si NCs. We hope that the current understanding on the synthesis and properties of hyperdoped Si NCs will help the development of novel devices based on hyperdoped Si NCs.

2.6 References

[1] Yu, X.; Chen, J.; Ma, X.; Yang, D. Impurity Engineering of Czochralski Silicon. *Mater. Sci. Eng. R* **2013**, *74*, 1-33.

[2] Koenraad, P. M.; Flatte, M. E. Single Dopants in Semiconductors. *Nat. Mater.***2011**, *10*, 91-100.

[3] Cui, Y.; Lieber, C. M. Functional Nanoscale Electronic Devices Assembled Using Silicon Nanowire Building Blocks, *Science* **2001**, *291*, 851-853.

[4] Imakita, K.; Ito, M.; Naruiwa, R.; Fujii, M.; Hayashi, S. Ultrafast Third Order Nonlinear Optical Response of Donor and Acceptor Codoped and Compensated Silicon Quantum Dots, *Appl. Phys. Lett.* **2012**, *101*, 041112.

[5] Stegner, A. R.; Pereira, R. N.; Lechner, R.; Klein, K.; Wiggers, H.; Stutzmann, M.; Brandt, M. S. Doping Efficiency in Freestanding Silicon Nanocrystals from the Gas Phase: Phosphorus Incorporation and Defect-Induced Compensation, *Phys. Rev. B* **2009**, *80*, 165326.

[6] Kodera, H. Constitutional Supercooling during the Crystal Growth of Germanium and Silicon. *J. J. Appl. Phy.* **1963**, *2*, 527.

[7] Bustarret, E.; Marcenat, C.; Achatz, P.; Kacmarcik, J.; Levy, F.; Huxley, A.; Ortega, L.; Bourgeois, E.; Blase, X.; Debarre, D.; Boulmer, J. Superconductivity in Doped Cubic Silicon. *Nature* **2006**, *444*, 465-468.

[8] Ertekin, E.; Winkler, M. T.; Recht, D.; Said, A. J.; Aziz, M. J.; Buonassisi, T.; Grossman, J. C. Insulator-to-Metal Transition in Selenium-Hyperdoped Silicon: Observation and Origin. *Phys. Rev. Lett.* **2012**, *108*, 026401.

[9] Moutanabbir, O.; Isheim, D.; Blumtritt, H.; Senz, S.; Pippel, E.; Seidman, D. N. Colossal Injection of Catalyst Atoms into Silicon Nanowires. *Nature* **2013**, *496*, 78-82.

[10] Pi, X. D.; Delerue, C. Tight-Binding Calculations of the Optical Response of Optimally P-Doped Si Nanocrystals: A Model for Localized Surface Plasmon Resonance. *Phys. Rev. Lett.* **2013**, *111*, 177402.

[11] Rowe, D. J.; Jeong, J. S.; Mkhoyan, K. A.; Kortshagen, U. R. Phosphorus-Doped Silicon Nanocrystals Exhibiting Mid-Infrared Localized Surface Plasmon Resonance. *Nano Lett.* **2013**, *13*, 1317-1322.

[12] Fujii, M.; Toshikiyo, K.; Takase, Y.; Yamaguchi, Y.; Hayashi, S. Below Bulk-Band-Gap Photoluminescence at Room Temperature from Heavily P- and B-Doped Si Nanocrystals. *J. Appl. Phys.* **2003**, *94*, 1990-1995;

[13] Fujii, M.; Mimura, A.; Hayashi, S.; Yamamoto, Y.; Murakami, K. Hyperfine Structure of the Electron Spin Resonance of Phosphorus-Doped Si Nanocrystals. *Phys. Rev. Lett.* **2002**, *89*, 206805.

[14] Xie, M. Li, D.; Chen, L.; Wang, F.; Zhu, X.; Yang, D. The Location And Doping Effect of Boron in Si Nanocrystals Embedded Silicon Oxide Film. *Appl. Phys. Lett.* **2013**, *102*, 123108.

[15] Perego, M.; Bonafos, C. Fanciulli, M. Phosphorus Doping of Ultra-Small Silicon Nanocrystals. *Nanotechnology* **2010**, *21*, 025602.

[16] Sato, K.; Fukata, N.; Hirakuri, K. Doping and Characterization of Boron Atoms in Nanocrystalline Silicon Particles. *Appl. Phys. Lett.* **2009**, *94*, 161902.

[17] Khelifi, R.; Mathiot, D.; Gupta, R.; Muller, D.; Roussel, M.; Duguay, S. Efficient N-Type Doping of Si Nanocrystals Embedded in SiO_2 by Ion Beam Synthesis. *Appl. Phys. Lett.* **2013**, *102*, 013116.

[18] Pereira, R. N.; Almeida, A. J.; Stegner, A. R.; Brandt, M. S.; Wiggers, H. Exchange-Coupled Donor Dimers in Nanocrystal Quantum Dots. *Phys. Rev. Lett.* **2012**, *108*, 126806.

[19] Knipping, J.; Wiggers, H.; Rellinghaus, B.; Roth, P.; Konjhodzic, D.; Meier, C. Synthesis of High Purity Silicon Nanoparticles in a Low Pressure Microwave Reactor. *J. Nanosci. Nanotech.* **2004**, *4*, 1039-1044.

[20] Mangolini, L.; Thimsen, E.; Kortshagen, U. High-Yield Plasma Synthesis of Luminescent Silicon Nanocrystals. *Nano Lett.* **2005**, *5*, 655-659.

[21] Pi, X. D.; Liptak, R. W.; Nowak, J. D.; Wells, N. P.; Carter, C. B.; Campbell, S. A.; Kortshagen, U. Air-Stable Full-Visible-Spectrum Emission from Silicon Nanocrystals Synthesized by an All-Gas-Phase Plasma Approach. *Nanotechnology* **2008**, *19*, 245603.

[22] Norris, D. J. Doped Nanocrystals. *Science* **2008**, *319*, 1776-1779.

[23] Seah, M. P.; Dench, W. A. Quantitative Electron Spectroscopy of Surfaces: A Standard Data Base for Electron Inelastic Mean Free Paths in Solids. *Surf. Interface Anal.* **1979**, *1*, 2-11.

[24] Fukata, N. Impurity Doping in Silicon Nanowires. *Adv. Mater.* **2009**, *21*, 2829-2832.

[25] Fano, U. Effects of Configuration Interaction on Intensities and Phase Shifts. *Phys. Rev.* **1961**, *124*, 1866-1878.

[26] Cabrera, N.; Mott, N. F. Theory of the Oxidation of Metals. *Rep. Prog. Phys.* **1949**, *12*, 163.

[27] Jacobs, E. P.; Dorda, G. Mechanical Stress at the (111) Si Surface Covered by SiO_2 and Al/SiO_2 layers. *Surf. Sci.* **1978**, *73*, 357-364.

[28] Cui, H.; Wang, C. X.; Yang, G. W. Origin of Self-Limiting Oxidation of Si Nanowires. *Nano Lett.* **2008**, *8*, 2731-2737.

[29] Yen, J.-Y.; Hwu, J.-G. Enhancement of Silicon Oxidation Rate Due to Tensile Mechanical Stress. *Appl. Phys. Lett.* **2000**, *76*, 1834-1835.

[30] Li, X. G.; He, Y. Q.; Talukdar, S. S.; Swihart, M. T. Process for Preparing Macroscopic Quantities of Brightly Photoluminescent Silicon Nanoparticles with Emission Spanning the Visible Spectrum. *Langmuir* **2003**, *19*, 8490-8496.

[31] Himpsel, F. J.; McFeely, F. R.; Taleb-Ibrahimi, A.; Yarmoff, J. A.; Hollinger, G. Microscopic Structure of the SiO_2/Si Interface. *Phys. Rev. B* **1988**, *38*, 6084-6096.

[32] Pi, X. D.; Mangolini, L.; Campbell, S. A.; Kortshagen, U. Room-Temperature Atmospheric Oxidation of Si Nanocrystals after HF Etching. *Phys. Rev. B* **2007**, *75*, 085423.

[33] Mangolini, L.; Kortshagen, U. Selective Nanoparticle Heating: Another Form of Nonequilibrium in Dusty Plasmas. *Phys. Rev. E* **2009**, *79*, 026405.

[34] Allen, J. E. Probe Theory - the Orbital Motion Approach. *Physica Scripta* **1992**, *45*, 497.

[35] Christensen, J. S.; Radamson, H. H.; Kuznetsov, A. Y.; Svensson, B. G. Phosphorus and Boron Diffusion in Silicon Under Equilibrium Conditions. *Appl. Phys. Lett.* **2003**, *82*, 2254-2256.

[36] Pi, X. D.; Gresback, R.; Liptak, R. W.; Campbell, S. A.; Kortshagen, U. Doping Efficiency, Dopant Location, and Oxidation of Si Nanocrystals. *Appl. Phys. Lett.* **2008**, *92*, 123102.

[37] Kramer, N. J.; Anthony, R. J.; Mamunuru, M.; Aydil, E. S.; Kortshagen. U. Plasma-Induced Crystallization of Silicon Nanoparticles. *J. Phys. D, Appl. Phys.* **2014**, *47*, 075202.

[38] Luo, Y. R. *Comprehensive Handbook of Chemical Bond Energies*, CRC Press, **2007**.

[39] Ni, Z.; Pi, X. D.; Yang, D. Density Functional Theory Study on a 1.4 nm Silicon Nanocrystal Coated with Carbon. *RSC Adv.* **2012**, *2*, 11227-11230.

Chapter 3: Localized Surface Plasmon Resonance of Boron- and Phosphorous-Doped Silicon Nanocrystals*

***** This chapter is adapted from the publication authored by Shu Zhou, Xiaodong Pi, Zhenyi Ni, Yi Ding, Yingying Jiang, Chuanhong Jin, Christophe Delerue, Deren Yang and Tomohiro Nozaki in ACS Nano. (*ACS Nano, 9, 378-386,* (2015))

3.1 Abstract

Localized surface plasmon resonance (LSPR) of doped Si nanocrystals (NCs) is critical to the development of Si-based plasmonics. We now experimentally show that LSPR can be obtained from both B- and P-doped Si NCs in the mid-infrared region. Both experiments and calculations demonstrate that the Drude model can be used to describe the LSPR of Si NCs if the dielectric screening and carrier effective mass of Si NCs are considered. When the doping levels of B and P are similar, the LSPR energy of B-doped Si NCs is higher than that of P-doped Si NCs because B is more efficiently activated to produce free carriers than P in Si NCs. We find that the plasmonic coupling between Si NCs is effectively blocked by oxide at the NC surface. The LSPR quality factors of B- and P-doped Si NCs approach those of traditional noble metal NCs. We demonstrate that LSPR is an effective means to gain physical insights on the electronic properties of doped Si NCs. The current work on the model semiconductor NCs, i. e., Si NCs has important implication for the physical understanding and practical use of semiconductor NC plasmonics.

3.2 Introduction

Impressive progress on the development of localized surface plasmon resonance (LSPR) has recently been made by using semiconductor nanocrystals (NCs).[1-7] In contrast to conventional noble metal NCs, semiconductor NCs greatly facililate the integration of plasmonics with electronics.[8,9] Given the dominant role of silicon (Si) in electronics, the LSPR of Si NCs is highly desired for the plasmonics-electronics integration.[10,11] Rowe et al.[12] have recently demonstrated the LSPR of phosphorous (P)-doped Si NCs, leading to an intriguing question whether LSPR also occurs to boron (B)-doped Si NCs. It is well known that B and P introduce free holes and electrons in Si materials, respectively. Since holes can behave differently from electrons, one may expect differences in the LSPR between B- and P-doped Si NCs if the LSPR of B-doped Si NCs also indeed exists. In addition, it has been shown that B prefers entering the core of a Si NC, while P prefers residing at the surface of a Si NC.[13-17] This leads to an important question whether the preferential doping impacts the LSPR of doped Si NCs. Therefore, a comparative study between B- and P-doped Si NCs in the context of LSPR is currently imperative.

In this chapter, we focus on Si NCs that are doped with B and P at high concentrations. LSPR in the energy regions of 0.26-0.40 eV and 0.09-0.13 eV have been found in B- and P-doped Si NCs, respectively. We clearly show that the LSPR energy increases with the increase of the dopant concentration, highlighting the remarkable doping-enabled tunability of LSPR for semiconductor NCs. The optical absorption of B- and P-doped Si NCs can be well simulated by using the Drude model.[18] We find that the plasmonic coupling between Si NCs is negligible because of oxide at the NC surface. We point out that the differences in LSPR between B- and P-doped Si NCs are basically related to the dopant distribution and free carrier behavior.

3.3 Experimental Methods

Both undoped and doped Si NCs are synthesized by means of nonthermal plasma.[19,20] B and P-doped Si NCs were synthesized by introducing B_2H_6 (0.5% in Ar) and PH_3 (0.5% in Ar) into a SiH_4/Ar nonthermal plasma chamber, respectively. The flow rate of B_2H_6 (PH_3) was changed from 0.88 (1.77) standard cubic centimeters per minute (sccm) to 15.2 (30.3) sccm, while the flow rate of SiH_4 was kept at 31.5 sccm. The total gas flow rate was fixed at ~ 3820 sccm and the pressure was maintained at ~ 360 Pa for synthesizing all the Si NCs. A 13.56 MHz power source and a matching network were used to generate the plasma. The power for synthesizing all the Si NCs was ~ 200 W.

The concentration of B or P in an ensemble of Si NCs is obtained by using chemical titration. Si NCs doped with B (P) were initially reacted with KOH in a nickel crucible. The product was then transferred to a plastic cup. HNO_3 was added into the plastic cup to form silicic and boracic (phosphoric) acids. Excessive potassium chloride and potassium fluoride were added to precipitate potassium fluorosilicate and potassium fluoroborate (fluorophosphate). These precipitates were then hydrolyzed in water, leading to the formation of HF. The resulting solution was treated by a standard NaOH titration method. Phenolphthalein was used to indicate the end of titration.

Transmission electron microscopy (TEM) measurements were performed by FEI Tecnai G2 F20 S-TWIN with an acceleration voltage of 200 kV. High-angle annular dark field (HAADF) scanning TEM and element mapping measurements were performed by FEI Titan G2 80-200 w/Chemi STEM with an acceleration voltage of 200 kV. Si NCs were dispersed in ethanol by ultrasonication after they were synthesized. Samples for both TEM and HAADF-STEM measurements were prepared by drop-casting the Si-NC-containing dispersion onto a

carbon-coated copper grid. The copper grids were inserted to the microscope after ethanol totally evaporated.

X-ray diffraction (XRD) measurements were performed by X'Pert PRO. Si-NC powders were collected on a glass substrate inside the plasma synthesis system. X rays generated by a Cu Kα source at the voltage of 40 V were employed. A scanning step of 0.016° was used for measuring all the Si-NC powder samples.

X-ray photoelectron spectroscopy (XPS) measurements were performed by Kratos AXIS Ultra DLD. The samples for XPS were prepared by placing as-synthesized Si NCs on a 5 mm ×5 mm carbon-tape-covered aluminum substrate. They were measured within ~ 1 hour exposure to air. The measurements were carried out again after Si NCs were exposed to air at room temperature for 2 and 11 months.

For a Fourier transform infrared (FTIR) spectroscopy measurement a Si-NC dispersion was prepared by the addition of ~ 10 mg Si NCs into a 2 ml solvent (benzonitrile, 1,2 dichlorobenzene or chlorobenzene) and subsequent ultrasonication for 3 minutes with a tip-ultrasonicator (Sonic & Materials, Inc-VCX130PB) at ~ 2 W. The Si-NC dispersion was then drop-casted onto a thallium bromoiodide substrate for the FTIR measurement in the transmission mode. A FTIR spectrum was collected either after the solvent totally evaporated or during the course of the evaporation of the solvent. Nitrogen might be used to enable an inert atmosphere for a sample during the FTIR measurement. All the FTIR measurements were performed by using JASCO FT/IR-6100 with a resolution of 4 cm^{-1}.

3.4 Results and Discussion

3.4.1 Structure Characterization

Figure 3.1 shows the TEM results for both undoped and doped Si NCs. Sphere-like undoped Si NCs are clearly seen in the low-resolution TEM image (Figure 3.1(a)). Selected-area electron diffraction (SAED) demonstrates the excellent crystallinity of undoped Si NCs (inset of Figure 3.1(a)). Figure 3.1(b) representatively shows the lattice fringes of an undoped Si NC. It is found that a log-normal curve may be used to fit the size distribution of undoped Si NCs, the mean size of which is ~ 13 nm (Figure 3.1(c)). We do not see significant changes in the NC size when Si NCs are doped with B and P (Figure 3.1(f), (i)). Doped Si NCs remain crystalline (Figure 3.1(e), (h)). This mean NC size is similar to that obtained by XRD analysis.

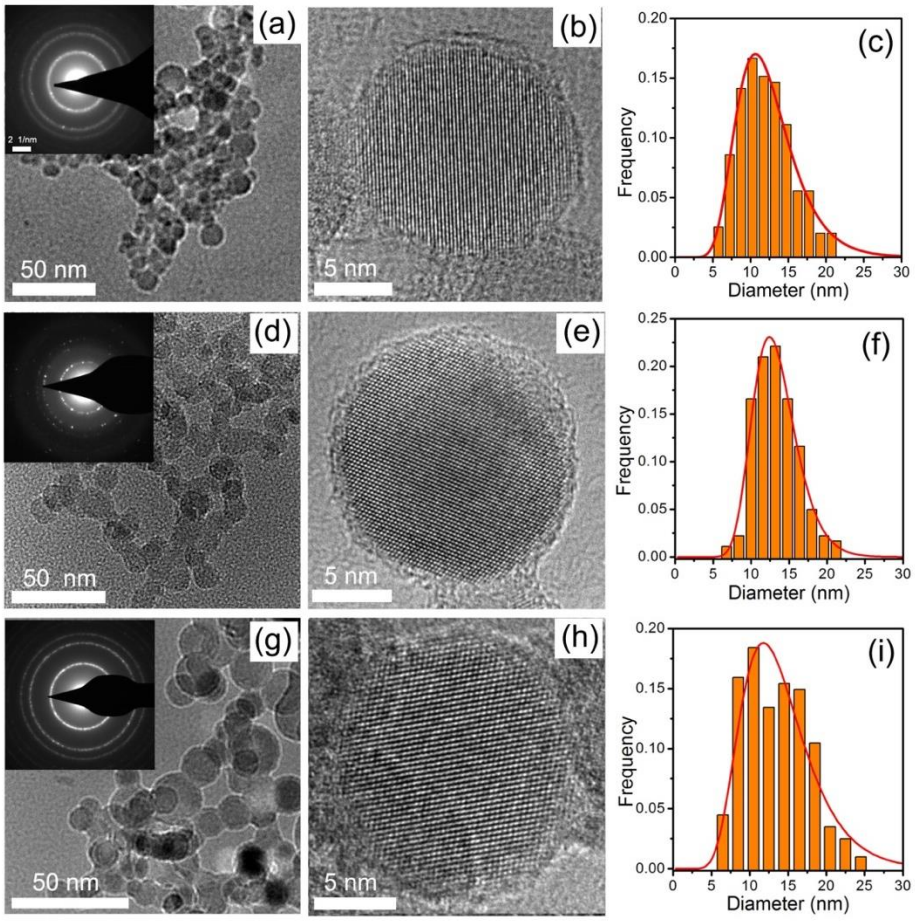

Figure 3.1. TEM images for undoped and doped Si NCs. (a) Low-resolution TEM image for undoped Si NCs. Inset of (a) shows the selected area electron diffraction (SAED) image. (b) Typical high-resolution TEM image for undoped Si NCs. (c) Size distribution for undoped Si NCs with a log-normal fit. The mean size is ~ 13 nm. (d) Low-resolution TEM image for Si NCs doped with 31% B. Inset of (d) shows the selected area electron diffraction (SAED) image. (e) Typical high-resolution TEM image of Si NCs doped with 31% B. (f) Size distribution for Si NCs doped with 31% B with a log-normal fit. The mean NC size is ~ 13 nm. (g) Low-resolution TEM image for Si NCs doped with 18% P. Inset of (g) shows the selected area electron diffraction (SAED) image. (h) Typical high-resolution TEM image of Si NCs doped with 18% P. (i) Size distribution for Si NCs doped with 18% P with a log-normal fit. The mean NC size is ~ 14 nm.

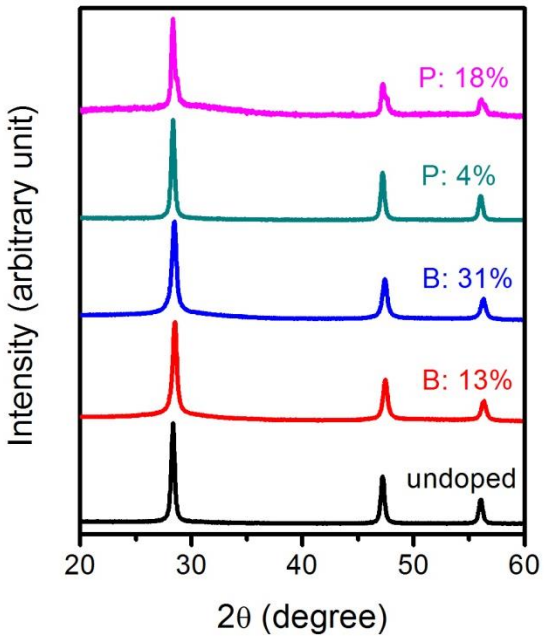

Figure 3.2. XRD spectra of undoped Si NCs, Si NCs doped with B at the concentrations of 13% and 31%, and Si NCs doped with P at the concentrations of 4% and 18%. The crystallinity of all the Si NCs is evidenced by the (111), (220) and (311) diffraction peaks, which are located at ~ 28.6 °, 47.3 °, 56.1 °, respectively. From the broadening of XRD peaks we work out that the sizes of all the Si NCs are ~ 13-14 nm.

Chemical titration measurements show that in the current work Si NCs are doped with B and P in the concentration ranges of 7%-31% and 4%-18%, respectively. Such high concentrations of B/P may actually mean that Si-B/P alloys are produced. However, we just stick to the traditional term of doping for convenience. Figure 3.3(a) and (b) representatively shows the HAADF-STEM images of Si NCs doped with B at the concentration of 31% and those doped with P at the concentration of 18%, respectively. Both of them indicate that the elements of B and P are associated with the element of Si. Si NCs are indeed doped with B and P. The successful doping for Si NCs has also been recently imaged by means of laser-assisted atom probe tomography.[21] It is seen that the the distribution of B in Si NCs is not uniform compared with that of P. The relatively long-time irradiation of high energy electrons (200 keV with a probe current of 70 pA for typically 200 seconds) may contribute to the displacement (and the associated diffusion) of boron atoms via the so-called knock-on mechanism, especially given the rather small mass of a B atom.

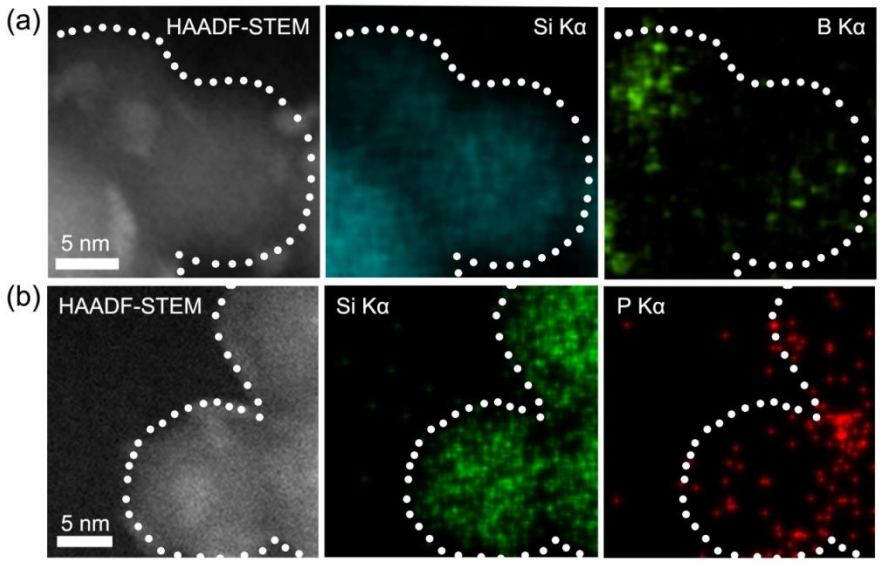

Figure 3.3. (a) HAADF-STEM image and corresponding Si and B mapping images for Si NCs doped with B at the concentration of 31%. (b) HAADF-STEM image and corresponding Si and P mapping images for Si NCs doped with 18% P. Areas where Si NCs are located are approximately marked to guide the eye in (a) and (b).

3.4.2 Localized Surface Plasmon Resonance

For all the as-synthesized Si NCs, we do not observe clear absorption peaks related to LSPR. This may be due to the fact that all the as-synthesized Si NCs are shortly exposed to air when FTIR spectroscopy measurements are carried out. The initial oxidation of Si NCs in air introduces a high density defects such as dangling bonds at the Si/oxide interface.[22,23] These interface defects may trap dopant-induced free carriers,[16,24,25] and hence void the LSPR. Figure 3.4 shows the ratio (R) of the number of Si atoms in intermediate oxidation states to that of Si atoms in the neutral state and all oxidation states. It is seen R decreases with the increase of oxidation time in air. It is known that a smaller value of R means a less defective Si/oxide interface.[26] Therefore, we believe that the density of defects at the Si/oxide interface is significantly reduced after Si NCs are oxidized in air for a long time. We would like to point out that the current improvement of the Si/oxide interface by means of long-time oxidation in air may be not efficient enough for practical use. More efficient oxidation methods such as ultraviolet (UV)-light enhanced oxidation or ozone-enabled chemical oxidation need to be investigated in the future.[27]

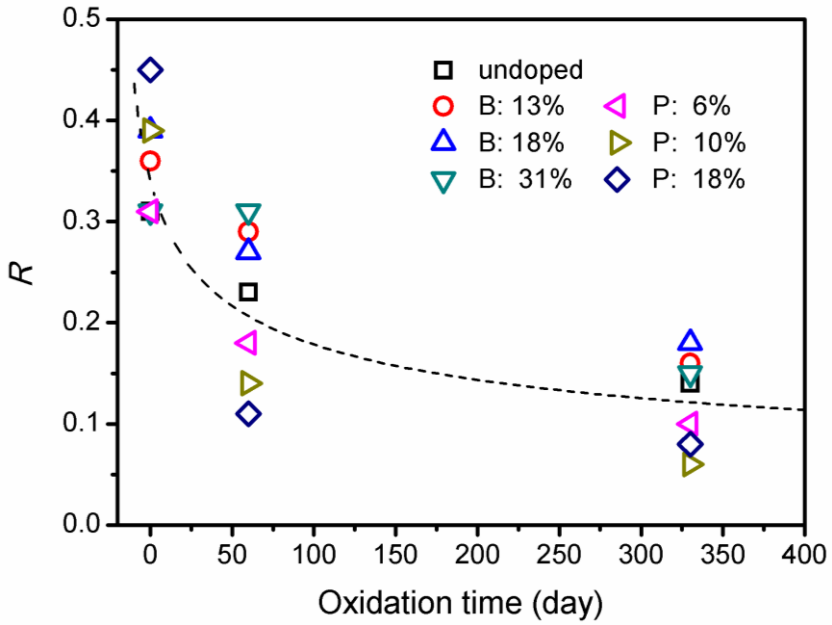

Figure 3.4. Ratio (R) of the number of Si atoms in intermediated oxidation states (Si^{+1}, Si^{+2} and Si^{+3}) to that of Si atoms in the neutral state and all oxidation states (Si^{+1}, Si^{+2}, Si^{+3} and Si^{+4}) obtained from XPS spectra of undoped and doped Si NCs. All the Si NCs are first measured shortly after exposure to air. They are then measured after ~ 60 and 330 days storage in air. The concentrations of P are 6%, 10% and 18%, while those of B are 13%, 18% and 31%. The dashed line is drawn to guide the eye.

FTIR spectroscopy measurements are carried out again for both undoped and doped Si NCs when they are oxidized in air for a long time (~ 330 days). Assignments of the vibration modes in FTIR are shown in Table 3.1.

Table 3.1. Assignments of vibration modes in FTIR characterization. ν: stretching; δ: bending; TO: transverse-optic; LO: longitudinal-optic.

Wavenumber (cm^{-1})	Mode
637	δ Si-Si-H_x

850	δ H-Si-O_2
880	δ H-Si-O_3
890	δ Si-Si-H_x
1100	ν Si-O-Si (TO)
1200	ν Si-O-Si (LO)
1100	ν Si-O-P
1354	ν B-O
2096	ν Si-Si-H_x
2370	ν O=C=O
2896, 2985	ν C-H_x

Figure 3.5 shows the obtained FTIR spectra for both undoped and doped Si NCs. The oxidation of all the Si NCs is evidenced by the absorption peaks at ~ 1100 and 1200 cm^{-1}, which are associated with the vibration of Si-O-Si bonds.[28] It is clear that a broad absorption peak emerges as Si NCs are doped with B (Figure 3.5(a)). The broad absorption peak moves from ~ 2090 to 3244 cm^{-1} when the B concentration increases from 7% to 31%. The dependence of the absorption energy on the doping level of B and the absence of the absorption for undoped Si NCs strongly suggest that B-doping induced free holes lead to LSPR in Si NCs.

For P-doped Si NCs, the absorption related to Si-O-Si bonds and Si-O-P bonds (these two types of bonds are similar because of the similarity of P atoms to Si atoms) dominates all the FTIR spectra in Figure 3.5(b). However, we do observe a broad shoulder at the low-wavenumber side of the Si-O-Si/Si-O-P related absorption in the FTIR spectrum of each P-doped Si-NC sample. It is found that the FTIR spectrum of undoped Si NCs in the range below 1500 cm^{-1} can be fitted with four peaks, which are located at ~ 850, 880, 1100 and 1200 cm^{-1}. Among these four peaks, the peaks at ~ 850 and 880 cm^{-1} are associated with the vibration of H-Si-O_2 and H-Si-O_3 bonds,[29] respectively. Since the oxidation of Si NCs is enhanced by P doping,[13,14] H-Si-O_2 bonds hardly exist in oxidized P-doped Si NCs. But H-Si-O_3 bonds remain in oxidized P-doped Si NCs. Therefore, three peaks located at 880, 1100 and 1200 cm^{-1} are employed to fit the FTIR spectrum of each P-doped Si-NC sample in the range below 1500 cm^{-1} together with a fourth peak, which corresponds to the above-mentioned broad shoulder. It is interesting that the position of thefourth peak (broad shoulder) changes from ~ 804 to 977 cm^{-1} as the concentration of P increases from 4% to 18%. This indicates that P-doping induced free electrons also give rise to LSPR in Si NCs.

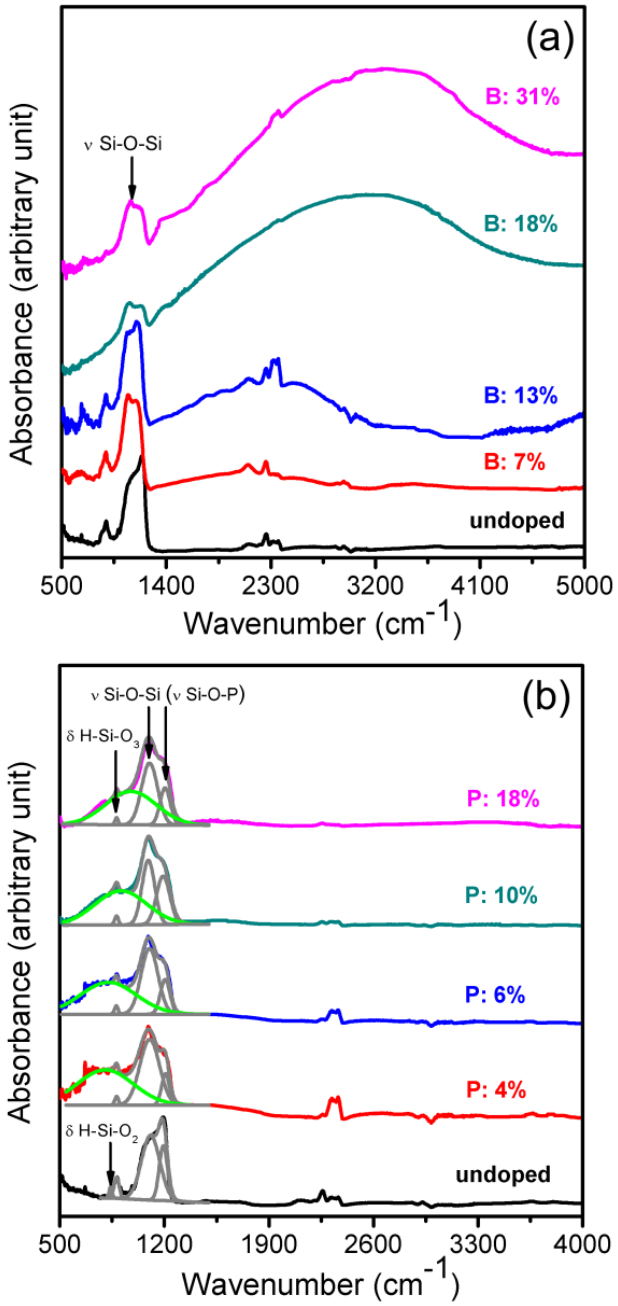

Figure 3.5. (a) FTIR spectra for undoped and B-doped Si NCs. (b) FTIR spectra for undoped and P-doped Si NCs. The FTIR spectrum for undoped Si NCs is fitted by four peaks located at ~ 850, 880, 1100 and 1200 cm^{-1}. While the FTIR spectrum of each P-doped Si-NC sample is fitted by three peaks at ~ 880, 1100 and 1200 cm^{-1} together with a fourth peak (green line). All the spectra are obtained after Si NCs are stored in air for ~ 330 days.

Please note that we have also obtained the FTIR spectra of P-doped Si NCs in the atmosphere of nitrogen after oxide at the NC surface is removed by HF vapor etching. As shown in Figure 3.6, the LSPR absorption has been clearly seen in these FTIR spectra without the interference of absorption induced by the vibration of O-related bonds.

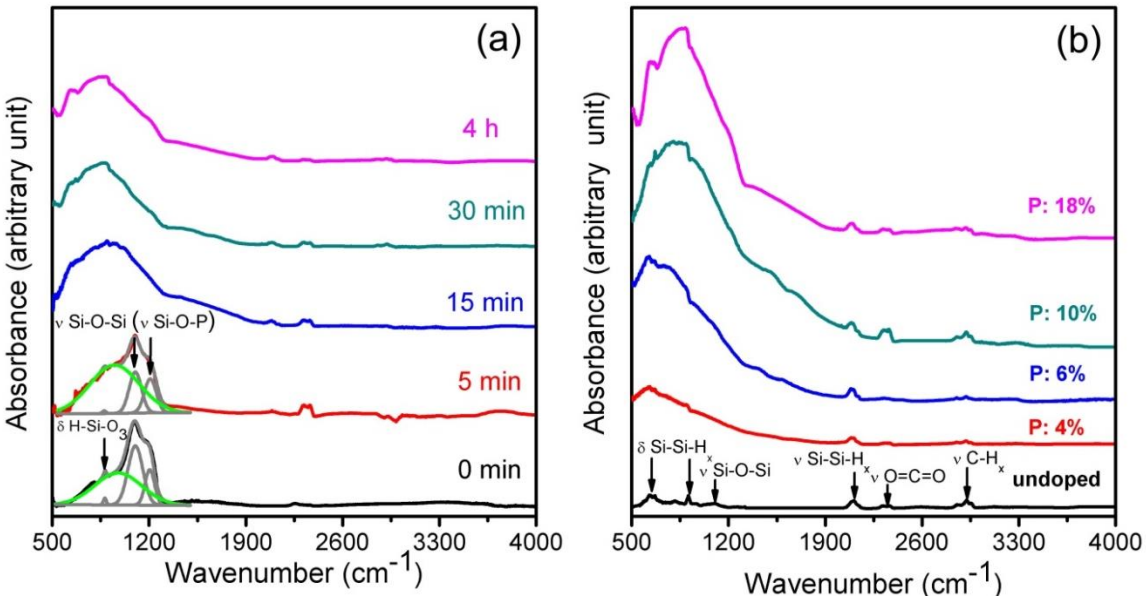

Figure 3.6. (a) FTIR spectra for P-doped Si NCs collected in the atmosphere of nitrogen after HF vapor etching up to 4 h. Si NCs are originally doped with P at the concentrations of 18%. (b) FTIR spectra for undoped and P-doped Si NCs collected in the atomosphere of nitrogen after 4 h HF vapor etching. The original P concentrations in P-doped Si NCs are 4%, 6%, 10% and 18%, respectively. Now the absorption induced by the vibration of O-related bonds is too small to interfere with the LSPR absorption, which blueshifts with the increase of the concentration of P.

Equation 3.1 was theoretically validated for P-doped Si NCs in our previous work[31]. In the current work we have further found that Equation 3.1 is also applicable to B-doped Si NCs by

means of tight-binding calculation. We have carried out tight-binding calculation with the random-phase approximation for 4 nm Si NCs that are doped with B at the concentrations of 5.0%, 9.9% and 19.9%. For the calculation details, please refer to reference [31]. Figure 3.7 shows the optical absorption of these B-doped Si NCs. The absorption peaks are due to the collective excitation of B-induced holes in Si NCs. We have plotted the obtained LSPR energy against the concentration of B, as shown in Figure 3.8. It is found that the data points may be nicely fitted by using

$$\hbar\omega_{sp} \approx \hbar\sqrt{\frac{ne^2}{\varepsilon_0 m^*(\varepsilon_\infty+2\varepsilon_m)}}, \tag{3.1}$$

where n is the free carrier concentration, e is the electronic charge, ε_0 is the free space permittivity, m^* is the effective mass of a free carrier, ε_∞ is the high-frequency dielectric constant of a Si NC. ε_m is the dielectric constant of the surrounding medium of the NC. Therefore, we conclude that Equation 3.1 is also valid for B-doped Si NCs. Please note that the NC size does not affect the applicability of Equation 3.1 because size-dependent screening has already been taken into account in this equation.[31]

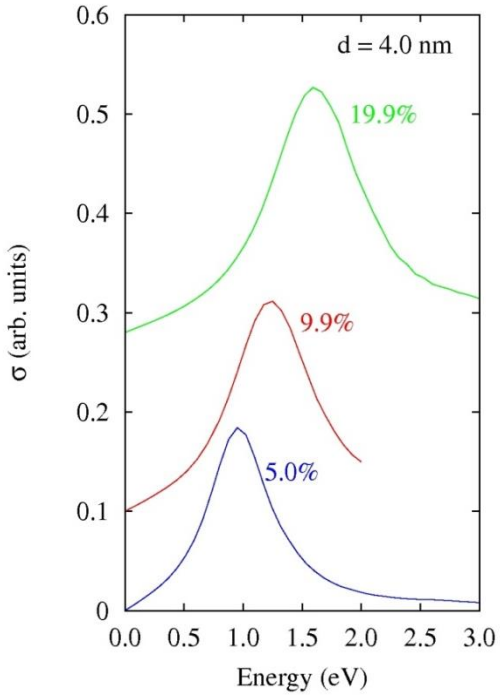

Figure 3.7. Optical absorption spectra of 4 nm Si NCs doped with B at the concentrations of 5.0%, 9.9% and 19.9%.

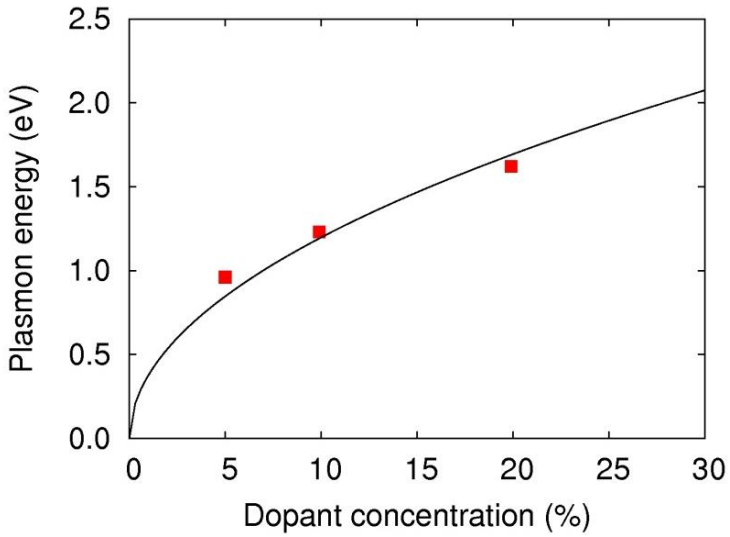

Figure 3.8. LSPR energy versus dopant concentration for 4 nm B-doped Si NCs. The solid line represents the LSPR energy predicted by using Equation 3.1.

To further prove that LSPR occurs to both B- and P-doped Si NCs, we have examined the dependence of the LSPR energy on the surrounding medium. Si NCs doped with B at the concentration of 31% and those doped with P at the concentration of 18% are initially dispersed in benzonitrile, 1,2 dichlorobenzen and chlorobenzen with the same concentration. Each of these dispersions is then drop-cast onto a thallium bromoiodide (KRS-5) substrate for a FTIR measurement, which is carried out immediately after the drop casting. This means that the surrounding media of Si NCs are the solvents during the FTIR measurements. The dielectric constants of benzonitrile, 1,2 dichlorobenzene and chlorobenzene are 25, 9.9 and 5.6, respectively.[30] When the solvents totally evaporate, the surrounding media of Si NCs are changed to be nitrogen, which has a dielectric constant of 1. Hence, we should expect changes in LSPR energy according to Equation 3.1. Please note that the carrier damping constant (Γ) is not incorporated in the Drude theory based Equation 3.1 because it is usually small enough not to seriously affect ω_{sp}.

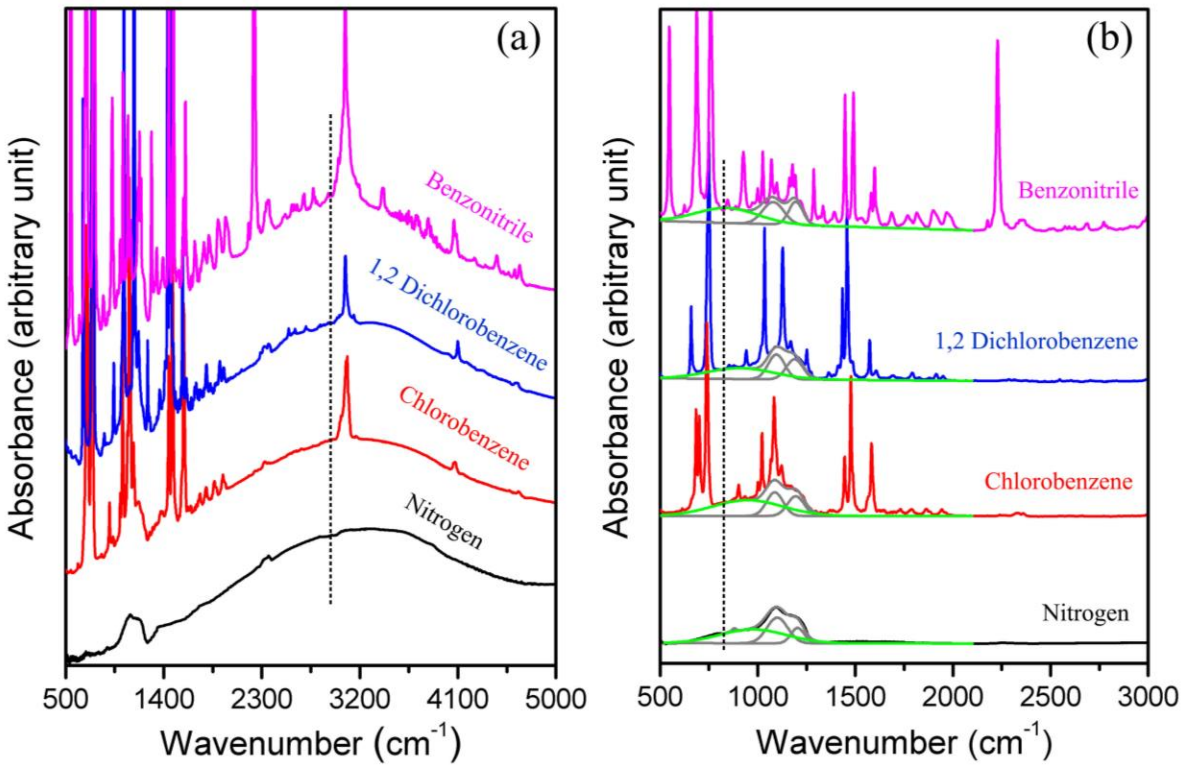

Figure 3.9. FTIR spectra for (a) B- and (b) P-doped Si NCs in different surrounding media, which are benzonitrile, 1,2 dichlorobenzene, chlorobenzene and nitrogen with the dielectric constants of 25, 9.9, 5.6 and 1, respectively. The dopant concentrations of B and P are 31% and 18%, respectively. Each spectrum for P-doped Si NCs is fitted by two peaks located at ~ 1100 and 1200 cm-1 together with a third peak (green line), which corresponds to the LSPR-induced absorption. The dashed lines are used to facilitate the observation on the shifts of the LSPR-induced absorption.

Figure 3.9 shows the FTIR spectra for (a) B- and (b) P-doped Si NCs with the varying surrounding medium. The solvents around Si NCs are manifested by the intense sharp absorption peaks in the FTIR spectra. As the dielectric constant of the surrounding medium decreases from 25 to 1, we see that the LSPR-induced absorption of B- and P-doped Si NCs blueshifts from ~ 2940 cm^{-1} to 3145 cm^{-1}, 3200 cm^{-1} and 3244 cm^{-1} and from ~ 830 cm^{-1} to 910 cm^{-1}, 949 cm^{-1} and 977 cm^{-1}, respectively. These changes in the LSPR energy are consistent with those predicted by

using Equation 3.1, in which an effective dielectric constant (ε_{eff}) is adopted to substitute ε_∞ for the sake of taking into account the screening effect of oxide at the NC surface (Section 3.4.5).[32] We would like to point out that the ignorance of the oxide at the NC surface causes the values of the LSPR energy predicted by Equation 3.1 to be smaller than those measured. This indicates that the dielectric screening of the oxide at the NC surface does exist. But it is clear that the oxide at the NC surface does not render complete dielectric screening. The LSPR of our doped Si NCs with oxide at the NC surface is reasonably sensitive to their environments.

All the samples for FTIR measurements are prepared by drop casting in the current work. After solvent evaporation Si NCs aggregate. According to previous work on noble metal NCs,[5,33] we may expect that the aggregation of Si NCs likely leads to plasmonic coupling between Si NCs. Figure 3.10 shows the FTIR spectra for Si NCs doped with 31% B and 18% P collected during the course of the evaporation of benzonitrile. When benzonitrile nearly completely evaporates after 80 min, the LSPR-induced absorption blueshifts from ~ 2940 cm^{-1} to 3240 cm^{-1} and from ~ 830 cm^{-1} to 940 cm^{-1} for B- and P-doped Si NCs, respectively. This means that plasmonic coupling between Si NCs is negligible despite the solvent-evaporation-induced aggregation of Si NCs, since plasmonic coupling usually gives rise to the redshift of LSPR-induced absorption.[34-36] Clearly, the observed blueshift of the LSPR-induced absorption is largely due to the change of the surrounding medium from benzonitrile to nitrogen.

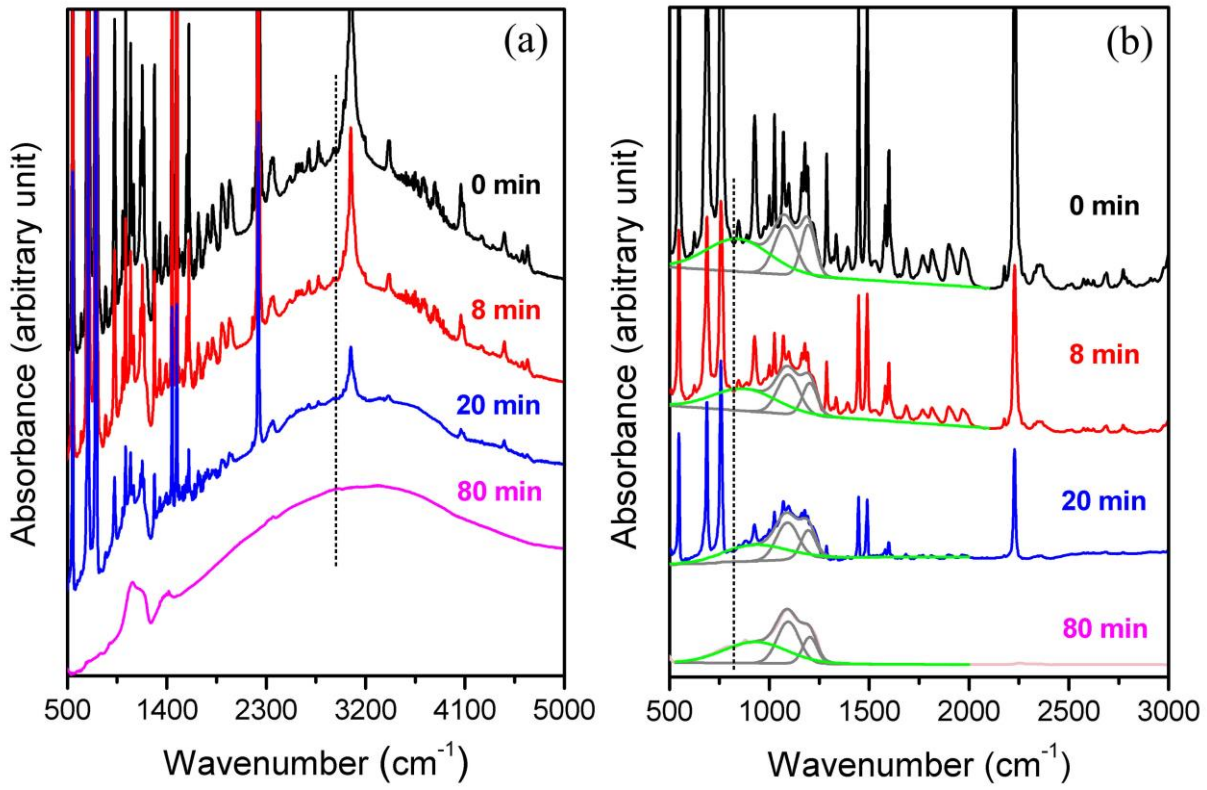

Figure 3.10. FTIR spectra for (a) B- and (b) P-doped Si NCs exhibiting shifts upon the solvent (benzonitrile) evaporates with different time. The dopant concentration is 31% for B and 18% for P, respectively. The absorption arising from P-doped Si NCs in (b) is fitted by two peaks located at ~ 1100 and 1200 cm^{-1} together with a third peak (green line) corresponding to the LSPR-induced absorption. The dashed lines are used to facilitate the observation on the shifts of the LSPR-induced absorption.

We have previously shown that after long-time room-temperature oxidation the thicknesses of surface oxide are ~ 1.4 and 2.7 nm for Si NCs doped with 31% B and 18% P, respectively.[14] Hence, we can work out that the shortest distances between Si NCs are ~ 2.8 and 5.4 nm for Si NCs doped with 31% B and 18% P, respectively. These shortest NC-NC distances are larger than 20% of the diameter of Si NCs (~ 2.6 nm). Because near-field plasmonic coupling significantly

decays as the NC-NC distance is larger than 20% of the NC size,[34-36] we can readily understand the negligible plasmonic coupling indicated by Figure 3.10.

We would like to mention that we have also collected FTIR spectra for HF-vapor-etched Si NCs that are doped with 31% B and 18% P during the course of the evaporation of benzonitrile. Figure 3.11 shows FTIR spectra for Si NCs doped with 31% B and those doped with 18% P after HF vapor etching. The successful removal of oxide at the NC surface is evidenced by the absence of the Si-O-Si absorption peak in all the FTIR spectra. As the solvent of benzonitrile totally evaporates, the LSPR-induced absorption of B- and P-doped Si NCs redshifts from ~ 3057 cm^{-1} to 2810 cm^{-1} and from ~ 1020 cm^{-1} to 840 cm^{-1} , respectively. This indicates that the plasmonic coupling between Si NCs becomes stronger as the distances between Si NCs decrease with the evaporation of benzonitrile. Clearly, the distances between Si NCs can be small enough to enable the plasmonic coupling when there is no oxide at the NC surface. The redshifts of the LSPR energy are up to 8% and 18% for B- and P-doped Si NCs, respectively. The stronger plasmonic coupling between P-doped Si NCs may be due to the higher carrier mobility of free electrons[8] and the preferential incorporation of P in the near-surface region. It is apparent that the lack of oxide at the NC surface causes the distances between Si NCs to be small enough to enable strong plasmonic coupling when Si NCs aggregate.

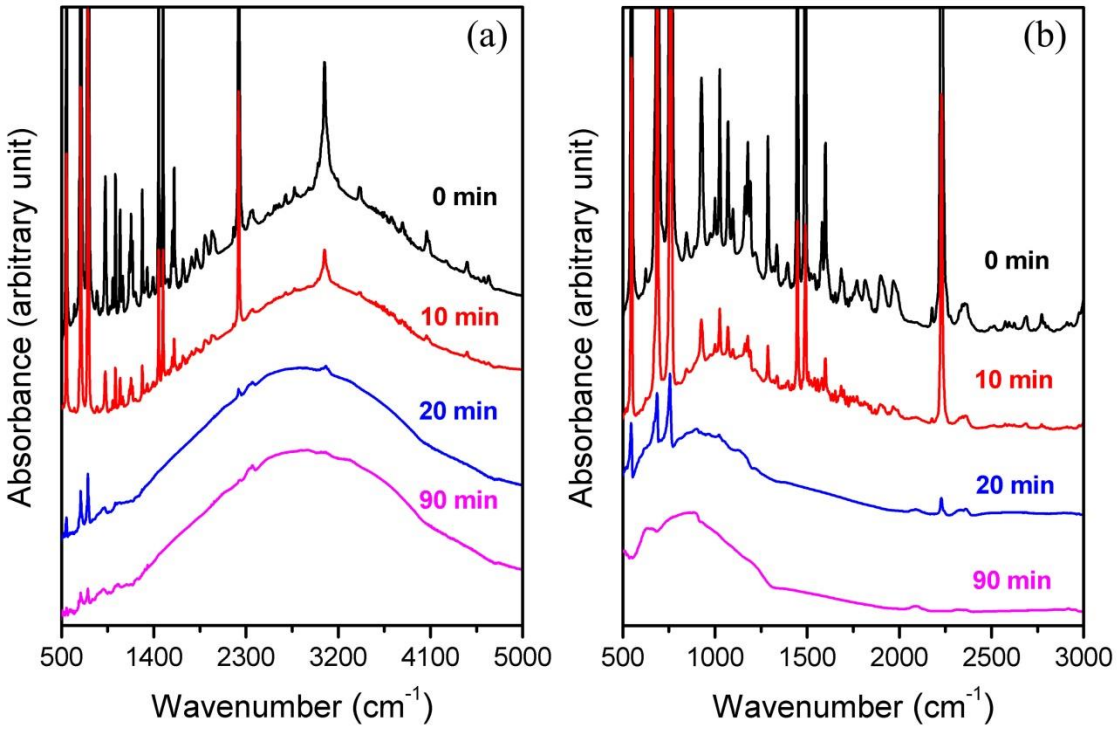

Figure 3.11. FTIR spectra for (a) B- and (b) P-doped Si NCs collected during the evaporation of benzonitrile for up to 90 min. Both B- and P- doped Si NCs are etched by HF vapor for 4 h before the FTIR measurements. The dopant concentrations are 31% and 18% for B and P, respectively.

3.4.3 Drude Fitting and Simulation

The Mie absorption cross section $\sigma_A(\omega)$ of a Si NC is calculated by considering the Drude contribution [37] via

$$\sigma_A(\omega) = \frac{8\pi^2\sqrt{\varepsilon_m}r^3\omega}{c}\,\mathrm{Im}\left\{\frac{\varepsilon(\omega)-\varepsilon_m}{\varepsilon(\omega)+2\varepsilon_m}\right\}, \tag{3.2}$$

where $\varepsilon(\omega) = \varepsilon_\infty - \frac{{\omega_p}^2}{\omega^2+i\omega\Gamma}$. ω is the frequency. c is the speed of light. r is the NC radius. ε_m is the dielectric constant of the surrounding medium of the NC. $\varepsilon(\omega)$ is the frequency-dependent dielectric constant of the NC. Γ is the carrier damping constant. ω_p is the bulk plasma frequency.

ε_∞ is the high frequency dielectric constant of the NC. In the current study a Si NC is covered by an oxide shell, as schematically shown in Figure 3.12. Therefore, an effective dielectric constant (ε_{eff}) is adopted to substitute ε_∞ for the Si NC to take into account the effect of the oxide shell. According to Neeves A. E et al's work,[38] we obtain ε_{eff} by using

$$\varepsilon_{eff} = \varepsilon_2(\varepsilon_1(3 - 2\mathrm{P}) + 2\varepsilon_2\mathrm{P})/(\varepsilon_1\mathrm{P} + \varepsilon_2(3 - \mathrm{P})), \tag{3.3}$$

where ε_1 is the high frequency dielectric constant of the NC core. ε_2 is the high frequency dielectric constant of the oxide shell. P is given by

$$\mathrm{P} = 1 - R^3/r^3, \tag{3.4}$$

where R is the radii of the NC core. The values of R and r are obtained from our previous work[14]. ε_1 is calculated by using $\varepsilon_1 = 1 + 10.7/[1+(0.92/R_1)^{1.18}]$, which was previously demonstrated by Lannoo et al..[39] ε_2 is assumed to be 3.9.[40]

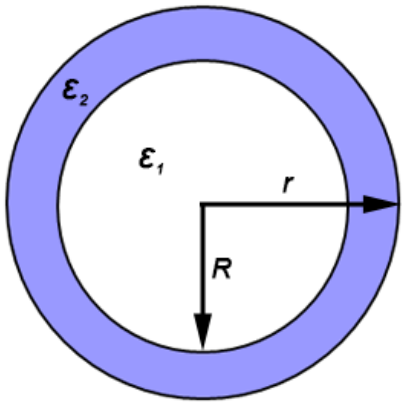

Figure 3.12. Schematic of the core-shell structure of an oxidized Si NC for calculating the effective dielectric constant of the NC.

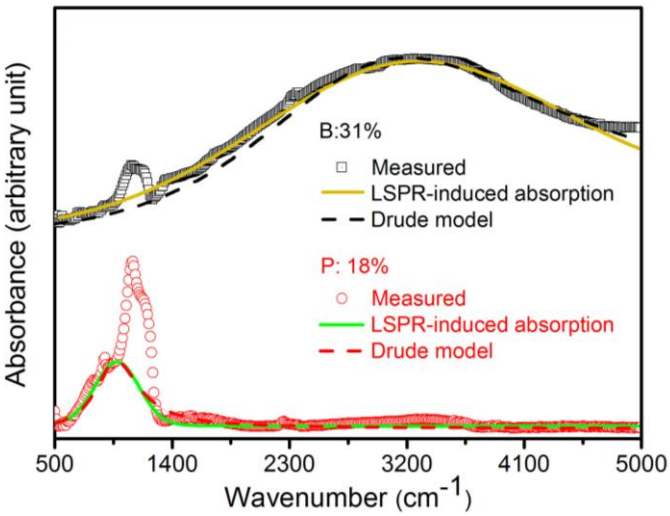

Figure 3.13. Fitting of the LSPR-induced absorption for Si NCs doped with 31% B and that for Si NCs doped with 18% P by using the Drude model.

We find that all the LSPR-induced absorption peaks can be well fitted by using Equation 3. 2. Please note that the validity of Equation 3.2 is justified by the surface-oxide-induced negligible plasmonic coupling between Si NCs. Figure 3.13 representatively shows the good fitting for Si NCs doped with 31% B and 18% P. Please note that Γ and ω_p are readily obtained from the fitting. We find that Γ increases from ~ 1000 to 3000 cm^{-1} as the concentration of B increases from 7% to 31%. But Γ slightly decreases from ~ 540 to 460 cm^{-1} when the concentration of P increases from 4% to 18%.

Table 3.2 summarizes the calculated values of ε_{eff} and those of ω_p and Γ obtained by fitting the LSPR-induced absorption of B- and P-doped Si NCs in the framework of Mie absorption, which takes the Drude contribution into account. The values of carrier mobility (μ) obtained from Γ are also shown in Table 3.2.

Table 3.2 The calculated values of the effective dielectric constant (ε_{eff}) for a Si NC with oxide at the NC surface. The values of the bulk plasma frequency (ω_p) and carrier damping constant (Γ) obtained by fitting the LSPR-induced absorption of B- and P-doped Si NCs. The values of carrier mobility (μ) are calculated by using $\mu = he/(m^*\Gamma)$, where h is the Plank constant and e is the electron charge.

Dopant concentration	ε_{eff}	ω_p (cm^{-1})	Γ (cm^{-1})	μ ($cm^2V^{-1}s^{-1}$)
B: 7%	7.0	6100	1000	147
B: 13%	7.0	6800	1400	105
B: 18%	7.1	9400	2900	51
B:31%	7.0	9600	3000	49
P: 4%	6.0	2240	540	362
P: 6%	5.4	2250	510	383
P: 10%	5.2	2450	480	407
P: 18%	5.0	2570	460	425

It is known that $\mu = he/(m^*\Gamma)$, where μ and h are the carrier mobility and Planck constant (Γ is deemed as energy), respectively.[41] Therefore, we can then work out the carrier mobility of each doped Si-NC sample. Figure 3.14 shows the carrier mobility of each doped Si-NC sample obtained by fitting the LSPR-induced absorption peak. We see that the hole mobility decreases

from ~ 150 to 50 $cm^2V^{-1}s^{-1}$ as the concentration of B increases from 7% to 31%. Such an inversely proportional dependence of the hole mobility on the concentration of B indicates that holes are predominantly scattered by ionized B atoms in Si NCs, similar to what occurs in bulk Si.[42] In contrast, the electron mobility for P-doped Si NCs increases from ~ 360 to 425 $cm^2V^{-1}s^{-1}$ with the increase of the concentration of P from 4% to 18%. By using

$$L = h\sqrt{3KT/m^*}/\Gamma, \tag{3.5}$$

where L, K and T are the mean free path of carriers, Boltzmann constant and temperature (300 K), respectively, we estimate that the mean free paths of holes in B-doped Si NCs and electrons in P-doped Si NCs are 2-7 and 12-15 nm, respectively. Since the mean free paths of electrons basically approximate to the NC size, the surface scattering of electrons in P-doped Si NCs should be more significant than that of holes in B-doped Si NCs. When P atoms are at the NC surface, they may be not ionized. In addition, P atoms are more electronegative than Si atoms. Hence, unionized P atoms at the NC surface can retard the movement of electrons toward the NC surface, reducing the surface scattering of electrons. The increase of the concentration of P may mainly lead to more P atoms at the NC surface, making the surface scattering of electrons less effective. Therefore, it turns out that the mobility of electrons in P-doped Si NCs can increase when the concentration of P increases.

We would like to point out that the values of the carrier mobility derived from the current optical measurements are comparable with those of doped bulk Si obtained by Hall measurements,[43] but several orders of magnitude higher than those of B- and P-doped Si-NC films in field-effect transistors.[44] This implies that carrier transport in a Si-NC film is mainly limited by the tunneling between neighboring Si NCs.

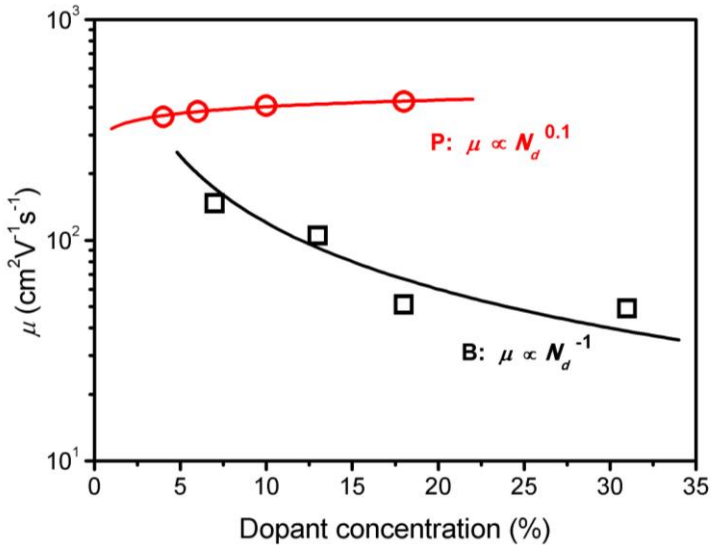

Figure 3.14. Carrier mobility (μ) of each doped Si-NC sample obtained by fitting the LSPR-induced absorption peak. The black line gives $\mu \propto N_d^{-1}$, while the red line gives $\mu \propto N_d^{0.1}$, where N_d is the dopant concentration.

The bulk plasma frequency (ω_p) derived from the fitting of LSPR-induced absorption is related to the free carrier concentration (n) via $\omega_p^2 = ne^2/(m^*\varepsilon_0)$. Therefore, we can work out the free carrier concentration from the fitting-obtained bulk plasma frequency. In addition, we may calculate the free carrier concentration by using Equation 3.1, in which $\hbar\omega_{sp}$ corresponds to the energy of the measured LSPR-induced absorption peak.

Table 3.3 Free carrier concentration (n) obtained from Equation 3.1 and bulk plasma frequency (ω_p) generated by the Drude fitting.

Dopant	n (cm^{-3})	n (cm^{-3})

concentration	(from Eq. 3.1)	(from the Drude fitting)
B: 7%	1.710^{20}	1.8×10^{20}
B: 13%	1.9×10^{20}	2.1×10^{20}
B: 18%	3.6×10^{20}	4.1×10^{20}
B:31%	4.0×10^{20}	4.3×10^{20}
P: 4%	1.4×10^{19}	1.8×10^{19}
P: 6%	1.7×10^{19}	1.8×10^{19}
P: 10%	2.0×10^{19}	2.0×10^{19}
P: 18%	2.4×10^{19}	2.7×10^{19}

The bulk plasma frequency (ω_p) derived from the fitting of LSPR-induced absorption is related to the free carrier concentration (n) via $\omega_p^2 = ne^2/(m^*\varepsilon_0)$. The free carrier concentration obtained with this expression is quite comparable with that obtained by using Equation 3.1 (Table 3.3). This further experimentally validates Equation 3.1 for Si NCs. Since n depends on the activation efficiency (η) of B or P in Si NCs with a concentration of N_d ($n = N_d\eta$), we can obtain the value of η by fitting the ω_p-N_d data according to

$$\omega_p = \sqrt{\frac{N_d \eta e^2}{m^* \varepsilon_0}}. \tag{3.6}$$

The results are shown in Figure 3.15. It is seen that the values of the activation efficiency of B and P are 2.8%-5.2% and 0.3%-0.9%, respectively. Clearly, B much more efficiently produces free carriers than P in Si NCs. We should mention that in the current study Si NCs are heavily doped in terms of free carrier concentrations (up to 4×10^{20} cm^{-3} and 3×10^{19} cm^{-3} for B- and P-doped Si NCs, respectively), although B and P have been hyperdoped to concentrations exceeding their solubility in Si.[45] It looks that the distribution of dopants in Si NCs is not the only factor that determines the activation of dopants. Although B prefers residing in the NC core, significant portion of B atoms remain electrically inactive. The trend of the decrease of the activation efficiency with the increase of the dopant concentration for both B and P indicates that the clustering of B and P may become serious as their concentrations increase.[46-48] Future work is needed to minimize the deactivation of B and P in Si NCs, moving the LSPR of Si NCs towards the visible region.

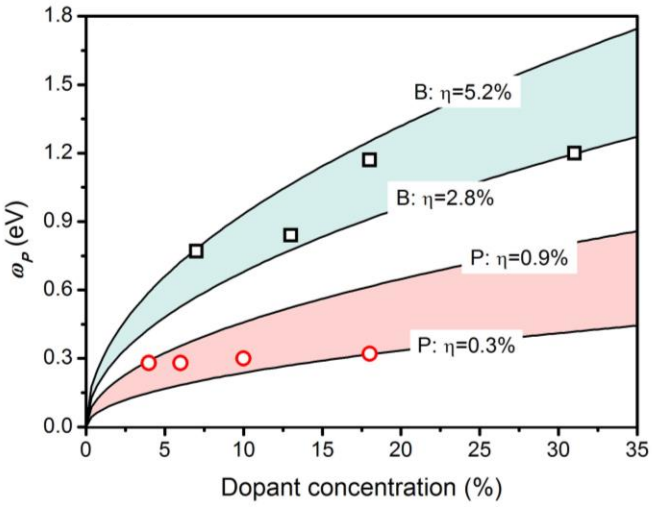

Figure 3.15. Bulk plasma frequency (ω_p) versus dopant concentration (N_d). The solid lines represent the fitting by using $\omega_p = \sqrt{N_d \eta e^2/(m^* \varepsilon_0)}$. The values of dopant activation efficiency (η) obtained from the fitting are indicated.

Finally, we calculate the quality factor (Q) of the LSPR of doped Si NCs by using

$$Q = \omega_{sp}/\gamma, \tag{3.7}$$

where γ is the linewidth (half width at the half maximum) of a LSPR-induced absorption peak. We notice that the values of γ for B-doped Si NCs are larger than those for P-doped Si NCs in the current work. The value of γ usually increases with the increase of the scattering of carriers.[2,49] As mentioned before, B atoms are more efficiently activated (ionized) to produce free carriers than P atoms. This means that the scattering of carriers by ionized impurities may be more significant in B-doped Si NCs than that in P-doped Si NCs. Therefore, it is reasonable that the values of γ for B-doped Si NCs are larger than those for P-doped Si NCs. Moreover, it is known that the scattering of carriers by twin boundaries may also contribute to the broadening of a LSPR-induced absorption peak.[12] We have previously demonstrated that twin defects may occur to both B- and P-doped Si NCs with high doping levels.[14] The number of twin boundaries in a B-doped Si NC is often larger than that in a P-doped Si NC, probably due to the larger difference in the atom size between a B atom and a Si atom. The larger numbers of twin boundaries should also contribute to the broader LSPR-induced absorption peaks for B-doped Si NCs.

Despite the larger values of γ for B-doped Si NCs the values of Q for B-doped Si NCs are actually not significantly smaller than those for P-doped Si NCs because the values of ω_{sp} for B-doped Si NCs are also larger. The values of Q for B-doped Si NCs are about 3-4, while those for P-doped Si NCs are about 4-5. Therefore, we may state that the values of Q for our doped Si NCs may be higher than those for other semiconductor NCs such as copper chalcogenide NCs,[50]

tungsten oxide NCs[6] and indium tin oxide NCs,[51] approaching those for traditional noble metal NCs.[52] This brings great promise for the use of doped Si NCs in a variety of demanding plasmonic applications such as highly sensitive chemical sensing.[53] We have complied the values of γ for current B- and P-doped Si NCs and those reported by Rowe et al. for P-doped Si NCs (Figure 3.16). It is found that the value of γ for B-doped Si NCs is smaller than that for P-doped Si NCs when their LSPR energies are similar. This implies that the value of Q for B-doped Si may be larger than that for P-doped Si NCs in the same LSPR energy region.

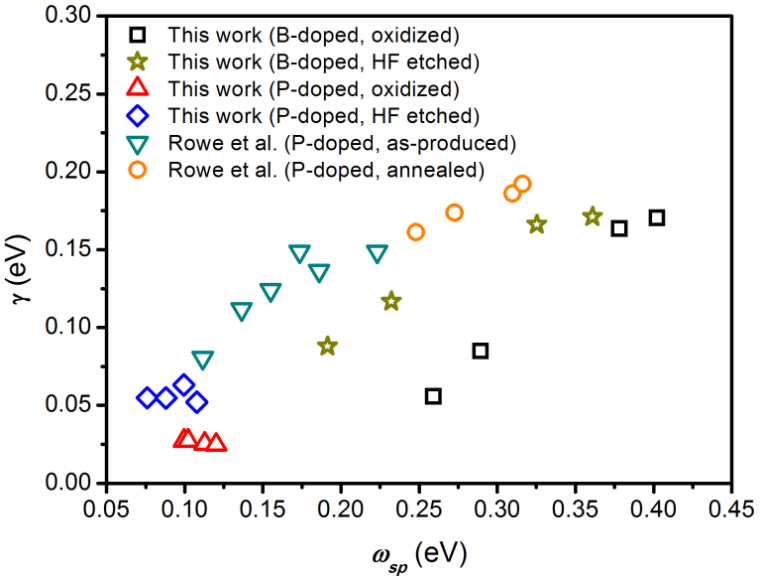

Figure 3.16. Dependence of the linewidth (γ) on the LSPR energy (ω_{sp}) for B and P-doped Si NCs. Previous results on P-doped Si NCs are obtained from Rowe et al.'s paper [1]. (black square: oxidized B-doped Si NCs in this work; dark yellow star: B-doped Si NCs after HF etching in this work; red triangle: oxidized P-doped Si NCs in this work; blue diamond: P-doped Si NCs after HF etching in this work; cyan inverted triangle: as-produced P-doped Si NCs by Rowe et al.; orange circle: P-doped Si NCs after annealing by Rowe et al.).

3.5 Conclusions

In summary, we have demonstrated the LSPR of B-doped Si NCs for the first time. The LSPR of B-doped Si NCs has been systematically compared with that of P-doped Si NCs. It is found that the LSPR energies for B- and P-doped Si NCs are now all located at mid-infrared region. But the LSPR energy of B-doped Si NCs is larger than that of P doped Si NCs when the doping levels of B and P are similar. This is because B is much more efficiently activated than P in Si NCs. By fitting the LSPR-induced absorption of both B- and P-doped Si NCs with the Drude model, the values of the hole/electron mobility for Si NCs have been obtained. It is seen that the hole mobility decreases with the increase of the B concentration of Si NCs. However, the electron mobility slightly increases with the increase of the P concentration of Si NCs. All the differences between B- and P-doped Si NCs may be related to dopant distribution, which impacts the dopant activation and carrier scattering. The LSPR quality factors of B and P doped Si NCs are approaching those of traditional noble metal NCs, signifying the great potential of doped Si NCs in plasmonic applications. Oxide at the NC surface is found to effectively block the plasmonic coupling between Si NCs. It looks that B-doped Si NCs are better positioned for practical use than P-doped Si NCs. On one hand, B atoms can be more efficiently activated than P atoms, enabling greater tunability of LSPR for B-doped Si NCs than P-doped Si NCs. On another hand, the LSPR of B-doped Si NCs may be not as seriously screened by the vibration of O-related bonds as that of P-doped Si NCs. We hope that the current experimental progress on the LSPR of doped Si NCs should encourage the development of novel Si-based plasmonic devices.[11,53]

3.6 References

[1] Liu, X.; Swihart, M. T. Heavily-Doped Colloidal Semiconductor and Metal Oxide Nanocrystals: An Emerging New Class of Plasmonic Nanomaterials. *Chem. Soc. Rev.* **2014**, *43*, 3908-3920.

[2] Luther, J. M.; Jain, P. K.; Ewers, T.; Alivisatos, A. P. Localized Surface Plasmon Resonances Arising from Free Carriers in Doped Quantum Dots. *Nat. Mater.* **2011**, *10*, 361-366.

[3] Polking, M. J.; Jain, P. K.; Bekenstein, Y.; Banin, U.; Millo, O.; Ramesh, R.; Alivisatos, A. P. Controlling Localized Surface Plasmon Resonances in GeTeNanoparticles Using an Amorphous-to-Crystalline Phase Transition. *Phys. Rev. Lett.* **2013**, *111*, 037401.

[4] Garcia, G.; Buonsanti, R.; Runnerstrom, E. L.; Mendelsberg, R. J.; Llordes, A.; Anders, A.; Richardson, T. J.; Milliron, D. J. Dynamically Modulating the Surface Plasmon Resonance of Doped Semiconductor Nanocrystals. *Nano Lett.* **2011**, *11*, 4415-4420.

[5] Naik, G. V.; Shalaev, V. M.; Boltasseva, A. Alternative Plasmonic Materials: Beyond Gold and Silver. *Adv. Mater.* **2013**, *25*, 3264-3294.

[6] Manthiram, K.; Alivisatos, A. P. Tunable Localized Surface Plasmon Resonances in Tungsten Oxide Nanocrystals. *J. Am. Chem. Soc.* **2012**, *134*, 3995-3998.

[7] Buonsanti, R.; Llordes, A.; Aloni, S.; Helms, B. A.; Milliron, D. J. Tunable Infrared Absorption and Visible Transparency of Colloidal Aluminum-Doped Zinc Oxide Nanocrystals. *Nano Lett.* **2011**, 11, 4706-4710.

[8] Ozbay, E. Plasmonics: Merging Photonics and Electronics at Nanoscale Dimensions. *Science* **2006**, *311*, 189-193.

[9] Faucheaux, J. A.; Stanton, A. L. D.; Jain, P. K. Plasmon Resonances of Semiconductor Nanocrystals: Physical Principles and New Opportunities. *J. Phys. Chem. Lett.* **2014**, *5*, 976-985.

[10] Soref, R. Mid-infrared Photonics in Silicon and Germanium. *Nat. Photon.* **2010**, *4*, 495-497.

[11] Walters, R. J.; Loon, R. V. A. van; Brunets, I.; Schmitz, J.; Polman, A. A Silicon-Based Electrical Source of Surface Plasmon Polaritons. *Nat. Mater.* **2010**, *9*, 21-25.

[12] Rowe, D. J.; Jeong, J. S.; Mkhoyan, K. A.; Kortshagen, U. R. Phosphorus-Doped Silicon Nanocrystals Exhibiting Mid-Infrared Localized Surface Plasmon Resonance. *Nano Lett.* **2013**, *13*, 1317-1322.

[13] Pi, X. D.; Gresback, R.; Liptak, R. W.; Campbell, S. A.; Kortshagen, U. Doping Efficiency, Dopant location, and Oxidation of Si Nanocrystals. *Appl. Phys. Lett.* **2008**, *92*, 123102.

[14] Zhou, S.; Pi, X. D.; Ni, Z. Y.; Luan, Q. B.; Jiang, Y. Y.; Jin, C. H.; Nozaki, T.; Yang, D. Boron- and Phosphorus-Hyperdoped Silicon Nanocrystals. Part. Part. Syst. Charact. **2014**, *32*, 213–221.

[15]Chan, T. L.; Tiago, M. L.; Kaxiras, E.; Chelikowsky, J. R. Size Limits on Doping Phosphorus into Silicon Nanocrystals. *Nano Lett.* **2008,** *8*, 596-600.

[16] Stegner, A. R.; Pereira, R. N.; Lechner, R.; Klein, K.; Wiggers, H.; Stutzmann, M.; Brandt, M. S. Doping Efficiency in Freestanding Silicon Nanocrystals from the Gas Phase: Phosphorus Incorporation and Defect-Induced Compensation. *Phys. Rev. B* **2009**, *80*, 165326.

[17] Chen, X. B.; Pi, X. D.; Yang, D. R. Critical Role of Dopant Location for P-Doped Si Nanocrystals. *J. Phys. Chem. C* **2011**, *115*, 661-666.

[18] Mendelsberg, R. J.; Garcia, G.; Li, H. B.; Manna, L.; Milliron, D. J. Understanding the Plasmon Resonance in Ensembles of Degenerately Doped Semiconductor Nanocrystals. *J. Phys. Chem. C* **2012**, *116*, 12226-12231.

[19] Mangolini, L.; Thimsen, E.; Kortshagen, U. High-Yield Plasma Synthesis of Luminescent Silicon Nanocrystals. *Nano Lett.* **2005**, *5*, 655-659.

[20] Pi, X. D.; Yu, T.; Yang, D. Water-Dispersible Silicon-Quantum-Dot-Containing Micelles Self-Assembled from an Amphiphilic Polymer. *Part. Part. Syst. Charact.* **2014**, *32*, 751-756.

[21] Khelifi, R.; Mathiot, D.; Gupta, R.; Muller, D.; Roussel, M.; Duguay, S. Efficient N-Type Doping of Si Nanocrystals Embedded in SiO_2 by Ion Beam Synthesis. *Appl. Phys. Lett.* **2013**, *102*, 013116.

[22] Gupta, A.; Schulz, C.; Wiggers, H. Influence of Etching and Surface Functionalization on the Optical Property of Luminescing Phosphorus Doped Silicon Nanoparticles. *J. Optoelectron. Adv. Mater.* **2010**, *12*, 518-522.

[23] Pi, X. D.; Liptak, R. W.; Campbell, S. A.; Kortshagen, U. In-Flight Dry Etching of Plasma-Synthesized Silicon Nanocrystals. *Appl. Phys. Lett.* **2007**, *91*, 083112.

[24] Stirling, A.; Pasquarello, A.; Charlier, J. C.; Car, R. Dangling Bond Defects at Si-SiO2 Interfaces: Atomic Structure of the P(b1) Center. *Phys. Rev. Lett.* **2000**, *85*, 2773-2776.

[25] Delerue, C.; Allan, G.; Lannoo, M. Theoretical Aspects of the Luminescence of Porous Silicon. *Phys. Rev. B* **1993**, *48*, 11024-11036.

[26] Himpsel, F. J.; McFeely, F. R.; Talebibrahimi, A.; Yarmoff, J. A.; Hollinger, G. Microscopic Structure of the SiO_2/Si Interface. *Phys. Rev. B* **1988**, *38*, 6084-6096.

[27] Zhang J.; Zou H. J.; Qing Q.; Yang Y. L.; Li Q. W.; Liu Z. F.; Guo X. Y.; Du Z. L. Effect of Chemical Oxidation on the Structure of Single-Walled Carbon Nanotubes. *J. Phys. Chem. B* **2003,** *107,* 3712-3718.

[28] Pi, X. D.; Mangolini, L.; Campbell, S. A.; Kortshagen, U. Room-Temperature Atmospheric Oxidation of Si Nanocrystals after HF Etching. *Phys. Rev. B* **2007**, *75*, 085423.

[29] Yeh, J. L.; Lee, S. C. Structural and Optical Properties of Amorphous Silicon Oxynitride. *J.*

Appl. Phys. **1996**, *79*, 656-663.

[30] Wheeler, L. M.; Neale, N. R.; Chen, T.; Kortshagen, U. R. Hypervalent Surface Interactions for Colloidal Stability and Doping of Silicon Nanocrystals. *Nat. Commun.* **2013**, *4*, 2197-2206.

[31] Pi, X. D.; Delerue, C. Tight-Binding Calculations of the Optical Response of Optimally P Doped Si Nanocrystals: A Model for Localized Surface Plasmon Resonance. *Phys. Rev. Lett.* **2013**, *111*, 177402.

[32] Neeves A. E.; Birnboim M. H. Composite Structures for the Enhancement of Nonlinear-Optical Susceptibility. *J. Opt. Soc. Am. B* **1989**, *6*, 787-796.

[33] Prashant K. J.; Mostafa A. E. Plasmonic Coupling in Noble Metal Nanostructures. *Chem. Phys. Lett.* **2010**, *487*, 153-164.

[34] Prashant K. J.; Huang W. Y.; Mostafa A. E. On the Universal Scaling Behavior of the Distance Decay of Plasmon Coupling in Metal Nanoparticle Pairs: A Plasmon Ruler Equation. *Nano Lett.* **2007**, *7*, 2080-2088.

[35] Su K. H.; Wei Q. H.; Zhang X.; Mock J. K.; Smith D. R.; Schultz S. Interparticle Coupling Effects on Plasmon Resonances of Nanogold Particles. *Nano Lett.* **2003**, *3*, 1087-1090.

[36] P Su W. H.; Charles N.; Andrea R. T. Tunable and Directional Plasmonic Coupling within Semiconductor Nanodisk Assemblies. *Nano Lett.* **2014**, *14*, 2372-2380.

[37] Mendelsberg, R. J.; Garcia, G.; Li, H. B.; Manna, L.; Milliron, D. J. Understanding the Plasmon Resonance in Ensembles of Degenerately Doped Semiconductor Nanocrystals. *J. Phys. Chem. C* **2012**, *116*, 12226-12231.

[38] Boyd, R. W.; Gehr, R. J.; Fischer, G. L.; Sipe, J. E. Nonlinear optical properties of nanocomposite materials. *Pure Appl. Opt.* **1996**, *5*, 505–512.

[39] Lannoo, M.; Delerue, C.; Allan, G.; Screening in Semiconductor Nanocrystallites and Its Consequences for Porous Silicon. *Phys. Rev. Lett.* **1995**, *74*, 3415-3418.

[40] Robertson, J. High Dielectric Constant Gate Oxides for Metal Oxide Si Transistors. *Rep. Prog. Phys.* **2006**, *69*, 327-396.

[41] Grant, J.; Shi, X.; Alton, J.; Cumming, D. R. S. Terahertz Localized Surface Plasmon Resonance of Periodic Silicon Microring Arrays. *J. Appl. Phys.* **2011**, *109*, 054903.

[42] Sze, S. M. *Physics of Semiconductor Devices*; John Wiley & Sons, New York, **1969**.

[43] Masetti, G.; Severi, M.; Solmi, S. Modeling of Carrier Mobility against Carrier Concentration in Arsenic-Doped, Phosphorus-Doped, and Boron-Doped Silicon. *IEEE Trans. Electron Devices* **1983**, *30*, 764-769.

[44] Gresback, R.; Kramer, N. J.; Ding, Y.; Chen, T.; Kortshagen, U. R.; Nozaki, T. Controlled Doping of Silicon Nanocrystals Investigated by Solution-Processed Field Effect Transistors. *ACS Nano* **2014**, *8*, 5650-5656.

[45] Kodera, H. Constitutional Supercooling during the Crystal Growth of Germanium and Silicon. *Jpn. J. Appl. Phys.* **1963**, *2*, 527-534.

[46] Sugimoto, H.; Fujii, M.; Imakita, K.; Hayashi, S.; Akamatsu, K. Phosphorus and Boron Codoped Colloidal Silicon Nanocrystals with Inorganic Atomic Ligands. *J. Phys. Chem. C* **2013**, *117*, 6807-6813.

[47] Y. H. Zeng, X. Y. Ma, D. X. Tian, W. Y. Wang, L. F. Gong, D. R. Yang, D. L. Que, Oxygen Precipitation Heterogeneously Nucleating on Silicon Phosphide Precipitates in Heavily Phosphorus-Doped Czochralski Silicon. *J. Appl. Phys.* **2009**, *105*, 093503.

[48] Landi, E.; Guimaraes, S.; Solmi, S. Influence of Nucleation on the Kinetics of Boron Precipitation in Silicon. *Appl. Phys. A* **1987**, *44*, 135-141.

[49] Alberto C.; Liberato M. New Materials for Tunable Plasmonic Colloidal Nanocrystals. *Chem. Soc. Rev.* **2014**, *43*, 3957-3975.

[50] Kriegel, I.; Jiang, C. Y.; Fernandez, J. R.; Schaller, R. D.; Talapin, D. V.; Como, E. D.; Feldmann, J. Tuning the Excitonic and Plasmonic Properties of Copper Chalcogenide Nanocrystals. *J. Am. Chem. Soc.* **2012**, *134*, 1583-1590.

[51] Kanehara, M.; Koike, H.; Yoshinaga, T.; Teranishi, T. Indium Tin Oxide Nanoparticles with Compositionally Tunable Surface Plasmon Resonance Frequencies in the Near-IR Region. *J. Am. Chem. Soc.* **2009**, *131*, 17736-17737.

[52] Rycenga, M.; Cobley, C. M.; Zeng, J.; Li, W. Y.; Moran, C. H.; Zhang, Q.; Qin, D.; Xia, Y. N. Controlling the Synthesis and Assembly of Silver Nanostructures for Plasmonic Applications, *Chem. Rev.* **2011**, *111*, 3669-3712.

[53] Law, S.; Podolskiy, V.; Wasserman, D. Towards Nano-scale Photonics with Micro-scale Photons: the Opportunities and Challenges of Mid-infrared Plasmonics, *Nanophotonics* **2013**, *2*, 103-130.

Chapter 4: Ligand-Free, Colloidal and Plasmonic Silicon Nanocrystals Heavily Doped with Boron*

* This chapter is adapted from the publication authored by Shu Zhou, Zhenyi Ni, Yi Ding, Michihiro Sugaya, Xiaodong Pi, and Tomohiro Nozaki in ACS Photonics. (*ACS Photonics*, 3, 415-422, (2016))

4.1 Abstract

Colloidal heavily-doped silicon nanocrystals (Si NCs) exhibiting tunable localized surface plasmon resonance (LSPR) are of great interest in cost-effective, solution-processed optoelectronic devices given the abundance and nontoxicity of Si. In this work we show that tunable plasmonic properties and colloidal stability without the use of ligands can be simultaneously obtained for Si NCs heavily doped with boron (B). The heavily B-doped Si NC colloids are found to be stable in air for months, opening up the possibility of device processing in ambient atmosphere. The optical absorption of heavily B-doped Si NCs reveals that the heavy B doping not only changes the concentration of free carriers that are confined in Si NCs, but also modifies the band structure of Si NCs. After heavy B doping both indirect and direct electronic transition energies remarkably decrease in Si NCs because the heavy B doping induced move of the conduction band toward the bandgap could be more significant than that of the Fermi level into the valence band. The LSPR of heavily B-doped Si NCs originates from free holes above the Fermi level, which are largely from the B-induced impurity band.

4.2 Introduction

As an emerging new class of plasmonic nanomaterials, heavily-doped semiconductor nanocrystals (NCs) with localized surface plasmon resonance (LSPR) have received great attention in the past few years because of their potential applications in novel optoelectronic devices.[1-3] In contrast to conventional metal NCs, the plasmonic properties of heavily-doped semiconductor NCs are largely dependent on the tunable concentration of free carriers that are confined in semiconductor NCs. The tunability of the free carrier concentration of semiconductor NCs may be realized either by intrinsically introducing defects or extrinsically doping impurities.[4-11] Despite recent impressive progress made on the heavy-doping-enabled LSPR of semiconductor NCs, the applications of plasmonic semiconductor NCs in optoelectronic devices remain challenging. Creating stable heavily-doped semiconductor-NC colloids is particularly demanded for the integration of the doping-enabled plasmonic properties with high-performance low-cost optoelectronic devices, given the fact that uniform and dense thin films may be inexpensively fabricated by using printing.[12-15] A common method to obtain stable semiconductor-NC colloids is the functionalization of the surface of semiconductor NCs by using organic ligands which effectively suppress the van der Waals force induced agglomeration of semiconductor NCs.[16-21] However, it becomes exceedingly difficult to functionalize the surface of heavily-doped semiconductor NCs because part of doped impurities inevitably reside at the NC surface,[22-24] leading to the significant change of the surface chemistry of semiconductor NCs. Moreover, it should be noted that organic ligands at the NC surface may seriously hinder the transport of carriers in semiconductor-NC films,[25-28] even if the surface of heavily-doped semiconductor NCs are successfully functionalized with organic ligands.

As one of the most important semiconductor NCs, silicon (Si) NCs may be heavily-doped to exhibit mid-infrared LSPR.[8,9,11,29] In contrast, the LSPR of other NCs are routinely limited in the visible and near-infrared regions.[2-5,7] It is additionally known that Si is abundant and nontoxic. Therefore, heavily-doped Si NCs hold considerable promise for plasmonics. Wheeler et al.[30] have recently indicated that the colloidal stability of plasmonic Si NCs can be confronted by functionalizing the NC surface with highly electronegative chlorine (Cl). The large bond polarization induced by Cl raises hypervalent interaction between the NC surface and hard donor molecules, providing the heavy doping and colloidal stability of Si NCs. But the plasmonic properties of Si NCs are unlikely to be widely tuned by the hypervalent interaction. In addition, Si-Cl bonds are not stable in air,[31-34] limiting the processing of Si NCs inside of inert atmosphere.

In this chapter, we demonstrate that tunable infrared LSPR and colloidal stability can be realized in the same time for heavily boron (B)-doped Si NCs without the use of ligands. The effect of heavy B doping on the band structure of Si NCs has been explored by optical absorption measurements. It is found that the heavy B doping leads to the decrease of the energy for both the indirect and direct electronic transitions in Si NCs because the heavy B doping induced move of the conduction band toward the bandgap could be more significant than that of the Fermi level into the valence band. The knowledge on the band structure of heavily B-doped Si NCs helps understand the origin of LSPR in heavily-doped semiconductor NCs.

4.3 Experimental Methods

Undoped Si NCs were synthesized by introducing SiH_4 (10% in Ar) and Ar into a nonthermal plasma chamber. The synthesis of B-doped Si NCs was realized by including B_2H_6

(0.5% in Ar) into the SiH_4/Ar nonthermal plasma. The flow rate of B_2H_6 was changed from 0.88 standard cubic centimeters per minute (sccm) to 15.2 sccm, while the flow rate of SiH_4 was kept at 31.5 sccm. The total gas flow rate was fixed at 3820 sccm and the pressure was maintained at 360 Pa. For synthesizing Cl-passivated Si NCs, $SiCl_4$ was employed as the silicon precursor. The flow rate of $SiCl_4$, H_2 and Ar introduced into the plasma chamber was 7, 140 and 560 sccm, respectively, leading to a pressure of 400 Pa. The power for synthesizing all Si NCs was ~ 200 W.

HF vapor etching of oxidized Si NCs were performed in a teflon container at room temperature for 4 hours. The etched NCs were placed in vacuum for 2 h to remove the excess HF for further analysis. Undoped Si NC colloid was prepared by adding the etched undoped Si NCs into benzonitrile followed by ultrasonication for 3 minutes with a tip-ultrasonicator (Sonic & Materials, Inc-VCX130PB) at ~ 2 W. Heavily B-doped Si NC colloids were prepared by adding the etched heavily B-doped Si NCs into benzonitrile without ultrasonication.

The concentrations of B for heavily doped Si NCs were determined by standard chemical titration measurements. Heavily B-doped Si NCs were reacted with solid KOH in a nickel crucible. The product was then transferred to a plastic cup containing HNO_3 to form silicic and boracic (phosphoric) acids. Excessive potassium chloride and potassium fluoride were added to the plastic cup to fully precipitate potassium fluorosilicate and potassium fluoroborate (fluorophosphate). These precipitates were then hydrolyzed in water, resulting in the formation of HF. The resulting solution was finally treated by a standard NaOH titration method, in which phenolphthalein was employed as an indicator for the end of titration. For TEM measurements, Samples were prepared by drop-casting the Si NC colloid onto a copper grid coated with carbon film. Each sample was gently heated to evaporate solvent before inserted into the microscope.

TEM measurements were performed by FE-TEM 2010F with an acceleration voltage of 200 kV. Zeta potential measurements were carried out on the NC colloids by using Zetasizer Nano-ZS (Malvern Instrument). Photoelectron spectroscopy measurements were performed by using Kratos AXIS Ultra DLD. XPS measurements were carried out with a monochromatic Al-Kα x-ray source. Samples for XPS were prepared by placing HF-etched Si NCs on carbon-tape-covered aluminum substrates. UPS measurements were carried out with a 21.2 eV He-Ia source and a −9.8 eV bias. Samples for UPS were prepared by placing the HF etched Si NCs on ITO-coated glass substrates.

Si NC films were fabricated in air by drop-casting the Si NC colloids onto Si substrate. A small funnel was placed over a film to slow the evaporation. Scanning electron microscopy (SEM) images were obtained by using a Hitachi S4000 field emission microscope at an acceleration voltage of 25 kV. Atomic force microscopy (AFM) images were obtained by using Shimadzu SPM-9600.

A UV-VIS spectrometer (Shimadzu UV-2000) was used to measure the optical absorption of Si NCs. Samples for UV-VIS were diluted NC colloids contained in quartz cuvettes with a path length of 10 mm. All the measurements were carried out at a resolution of 4 nm. Samples for FTIR measurements were prepared by drop-casting Si NC colloids on a thallium bromoiodide (KRS-5) substrate. Si NCs were self-assembled into films after solvent evaporation. A FTIR spectrometer (JASCO FT/IR-6100) operated in the transmission mode with a resolution of 4 cm^{-1} was used to measure all the samples.

4.4 Results and Discussion

Both undoped and heavily B-doped Si NCs have been synthesized by using a SiH_4-based nonthermal plasma.[23,35-37] After storage in air for 15 months both undoped and heavily B-doped Si NCs are treated with hydrofluoric acid (HF) to render much less-defective NC surface.[38] The resulting hydrogen (H)-passivated NCs are characterized by using transmission electron microscopy (TEM). Figure 4.1 representatively shows the TEM results for undoped Si NCs and Si NCs doped with B at the concentrations of ~ 7% and 31%. The low-resolution TEM image (Figure 4.1(a), (d) and (g)) and high-resolution TEM image (Figure 4.1(b), (e) and (h)) clearly show sphere-like Si NCs. In addition to lattice fringes, twining is also observed in the high-resolution TEM images of Si NCs doped with B (Figure 4.1(e) and (h)), characteristic of the heavy B doping of Si NCs.[9] By analyzing the size distributions in Figure 4.1(c), (f) and (i), the average sizes for undoped Si NCs, Si NCs doped with 7% B and Si NCs doped with 31% B are calculated to be ~ 7.5, 7.8, and 7.5 nm, respectively. The results indicates the heavy B doping hardly changes the size and crystallinity of Si NCs. TEM results for Cl-passivated Si NCs that are synthesized by a $SiCl_4$-based nonthermal plasma are also included in Figure 4.1 (j), (k), (l). The average size of Cl-passivated Si NCs is 7.5 nm, similar to that of B-doped Si NCs.

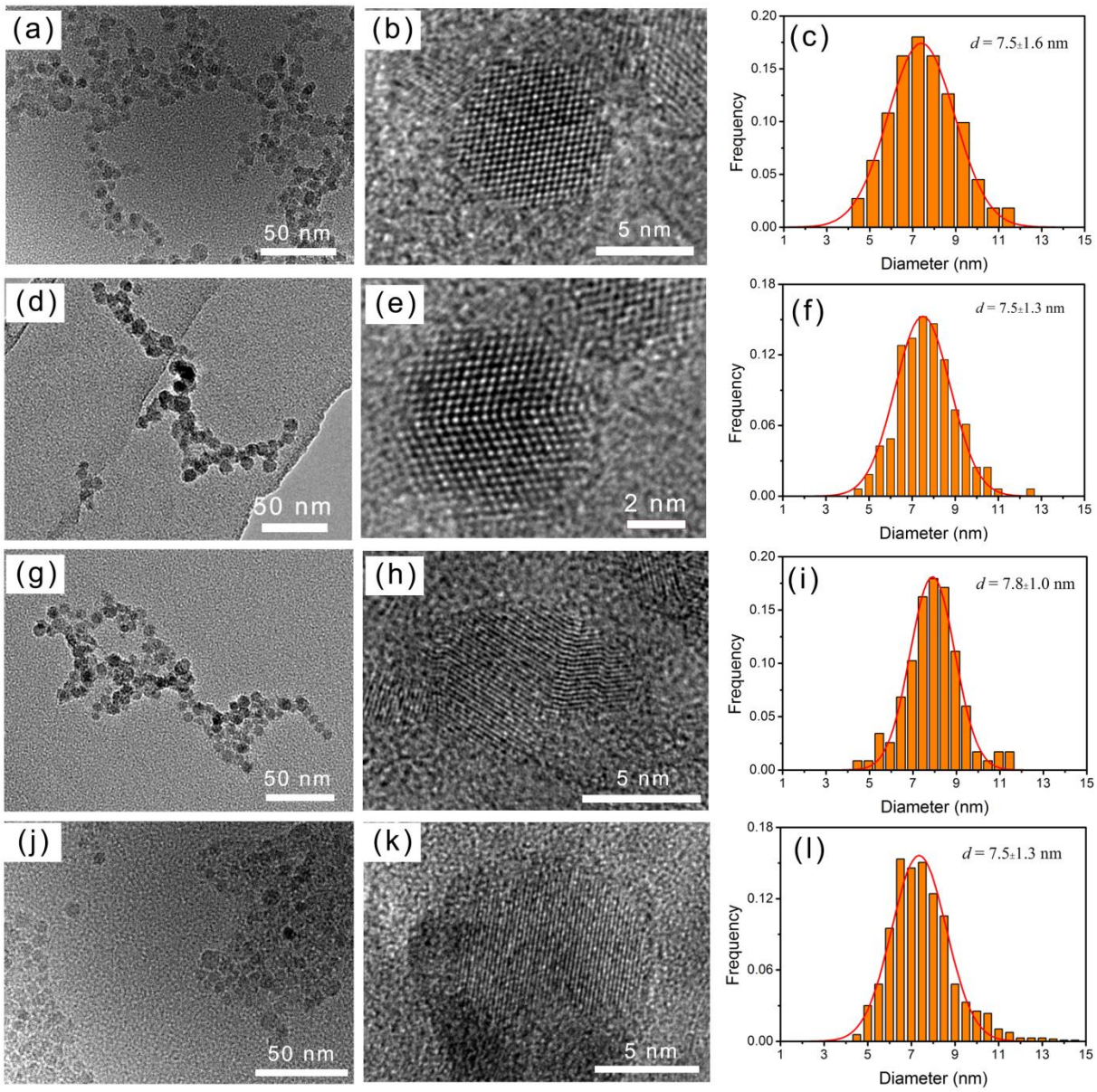

Figure 4.1. TEM images for undoped, heavily B-doped and Cl-passivated Si NCs. (a) Low-resolution TEM image, (b) high-resolution TEM image and (c) size distribution of Si NCs heavily doped with B at the concentration of ~ 7%. (d) Low-resolution TEM image for undoped Si NCs. (e) Typical high-resolution TEM image for undoped Si NCs. (f) Size distribution for undoped Si NCs. The mean NC size is 7.5 nm. (g) Low-resolution TEM image for Si NCs doped with 31% B. (h) Typical high-resolution TEM image for Si NCs doped with 31% B. (i) Size distribution for Si NCs doped with 31% B. The mean NC size is 7.8 nm. (j) Low-resolution TEM image for Cl-passivated Si NCs. (k) Typical high-resolution TEM image for Cl-passivated Si NCs. (l) Size distribution for Cl-passivated Si NCs. The mean NC size is 7.5 nm.

4.4.1 Colloidal Stability

It is well-known that undoped Si NCs are not soluble in most nonpolar solvents.[39] The choice of appropriate polar solvents such as benzonitrile may enable dilute solutions of undoped Si NCs after sonification,[40] but undoped Si NCs agglomerate shortly. Figure 4.2 shows the resulting cloudy dispersion of undoped Si NCs (the left image). In contrast to undoped Si NCs, heavily B-doped Si NCs may be readily dispersed in benzonitrile, leading to an optically transparent colloid (Figure 4.2, the middle image). This indicates that the agglomeration of Si NCs in benzonitrile is essentially suppressed by heavy B doping. The dispersibility of heavily B-doped Si NCs in benzonitrile is basically as good as that of Cl-passivated undoped Si NCs (Figure 4.3, the right image).

Figure 4.2. Photographs of undoped Si NCs (left), heavily B-doped Si NCs (middle) and Cl-passivated Si NCs (right) in benzonitrile. The concentrations for all Si NCs in benzonitrile are 0.04 mg/ml. The concentration of B for heavily doped Si NCs is ~ 7%.

Figure 4.3(a) shows the UV-VIS absorption spectra of the benzonitrile solutions of undoped, heavily B-doped and Cl-passivated Si NCs. Due to the agglomeration-induced light scattering, undoped Si NCs exhibit apparent optical absorption when the wavelength is > ~ 600 nm. However, the optical absorbance of heavily B-doped Si NCs and Cl-passivated Si NCs are almost zero in the long-wavelength region because their light scattering is negligible. Further evidence can be obtained from the derivation of the absorption spectrum, as shown in Figure 4.3(b). A rather broad peak in the derivative spectrum occurs to undoped Si NCs because of the significant scattering induced by agglomeration.

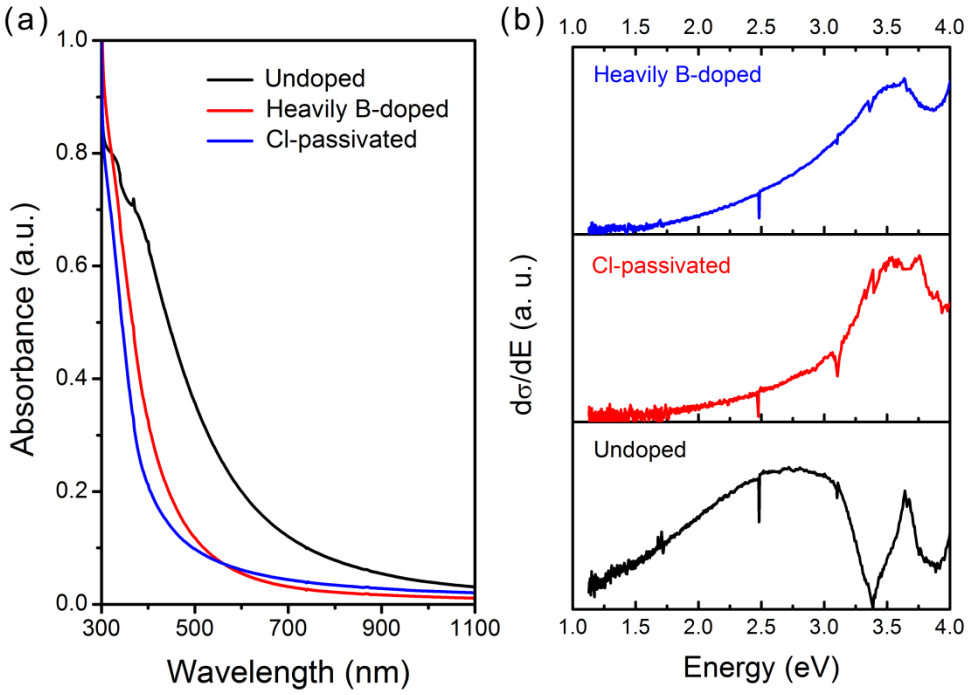

Figure 4.3. (a) UV-VIS absorption spectra of undoped Si NCs, heavily B-doped Si NCs and Cl-passivated Si NCs in benzonitrile. (b) Derivative absorption spectra of undoped Si NCs, Cl-passivated Si NCs and Si NCs doped with ~ 7% B in benzonitrile.

The stability of heavily B-doped Si NCs in benzonitrile has been studied by recording the optical absorption of the colloids during the course of storage in air. The results are shown in Figure 4.4. It can be seen that there is almost no change in the absorption spectra as storage time in air increases up to 4 months. Therefore, we claim that heavily B-doped Si NCs are readily well-dispersed and highly-stable in benzonitrile. We would like to point out that the Cl-passivated Si NCs strongly agglomerate and precipitate in benzonitrile after they are stored in air for a few days because of the instability of Si-Cl bonds at the NC surface.[31-34] The colloidal stability in air provided by heavy B doping in air opens up the possibility of the processing of devices that are based on Si NC films in ambient atmosphere.

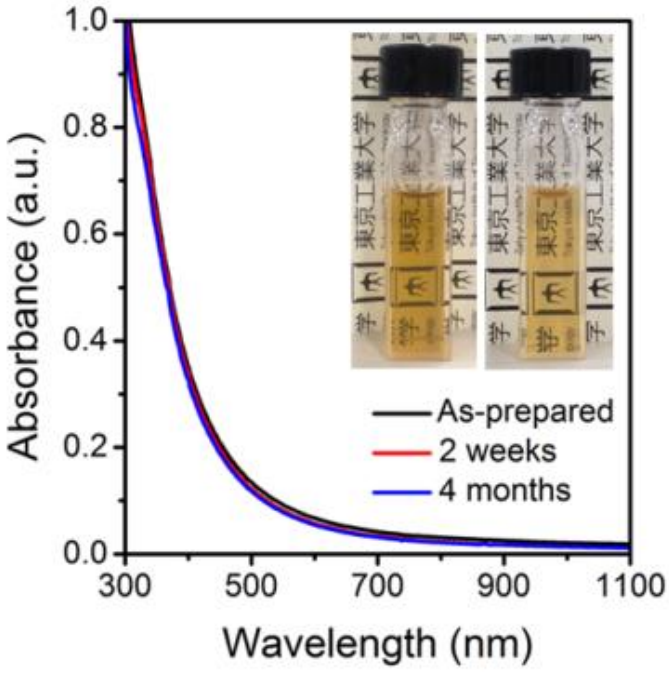

Figure 4.4. UV-VIS absorption spectra for heavily B-doped Si NCs in benzonitrile after they are stored in air for 0 day, 2 weeks and 4 months, respectively. The inset shows the photograph of as-prepared heavily B-doped Si NC colloid and that of the same colloid after 4 months storage in air.

Figure 4.5 shows the scanning electronic microscopy (SEM) image of a continuous and dense film obtained by drop-casting a 5 mg/ml benzonitrile solution of Si NCs heavily doped with B at the concentration of ~ 7% onto a Si substrate in air. The film is rather smooth with an average roughness of 15 nm, which is measured with atomic force microscopy (AFM) (inset of Figure 4.5). It is the excellent dispersion of heavily B-doped Si NCs in benzonitrile that enables the continuity and smoothness of the Si NC film.

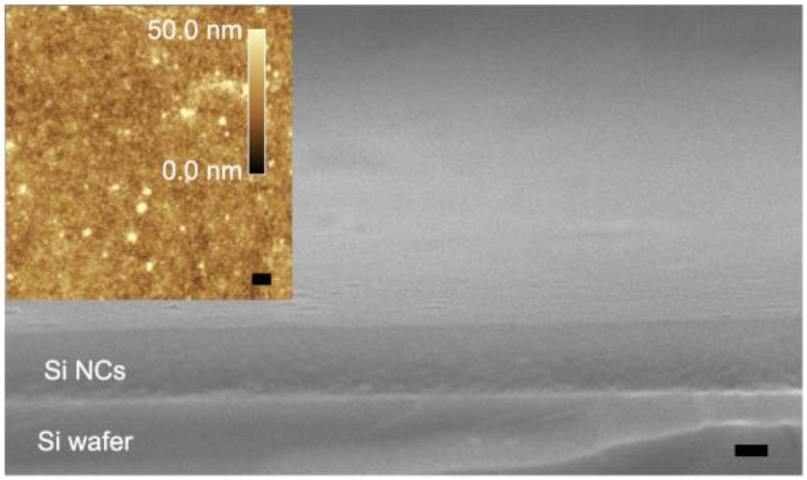

Figure 4.5. Scanning electron microscopy (SEM) and atomic force microscopy (AFM) (inset) show that a continuous, dense and smooth film is obtained by drop-casting heavily B-doped Si NC colloid on a Si substrate. Scale bar, 2 μm.

The colloidal stability of Si NCs in benzonitrile is largely dependent on their surface chemistry.[39,40] We have used Fourier transform infrared (FTIR) spectroscopy to characterize the Si NC films casted from the colloids of undoped and heavily B-doped Si NCs. Figure 4.6 shows the obtained FTIR results for both undoped and heavily B-doped Si NCs. For undoped Si NCs, the most prominent peaks at ~ 640, 890 and 2100 cm^{-1} are basically related to the vibration of

Si-H bonds.[41] Small peaks at ~ 810 and 1100 cm^{-1} associated with the Si-O stretching mode[41] can also be observed in the spectrum, indicating a little O exists at the NC surface. These peaks are all present in the FTIR spectrum of heavily B-doped Si NCs. No vibration modes related to B-H bonds are found in the FTIR spectrum, indicating that H prefers bonding with a Si atom over a B atom at the NC surface.

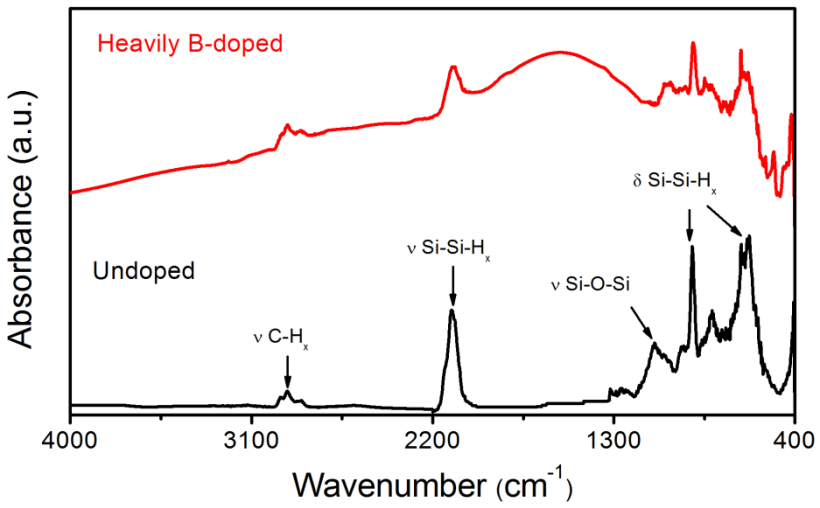

Figure 4.6. FTIR spectra of undoped and heavily B-doped Si NCs. The concentration of B is ~ 7%.

The existence of B at the surface of heavily B-doped Si NCs is evaluated by using X-ray photoelectron spectroscopy (XPS), as shown in Figure 4.7. The B 1s spectrum indicates that there are B atoms at the surface or subsurface of Si NCs. In the B 1s spectrum, the peak at 188.3 eV is related to B atoms that are bonded with four Si atoms (B(IV)-Si),[42] while the peak at 184.8 eV means a B atom is linked with three Si atoms (B(III)-Si).[43] The small peaks at 191.2 and 193.0 eV are associated with oxidized B,[43] indicating very little O at the NC surface. Since H cannot give rise to enough steric force to enable stable dispersion of Si NCs, B at the surface or subsurface of Si NCs should be responsible for the stable heavily B-doped Si NC colloids.

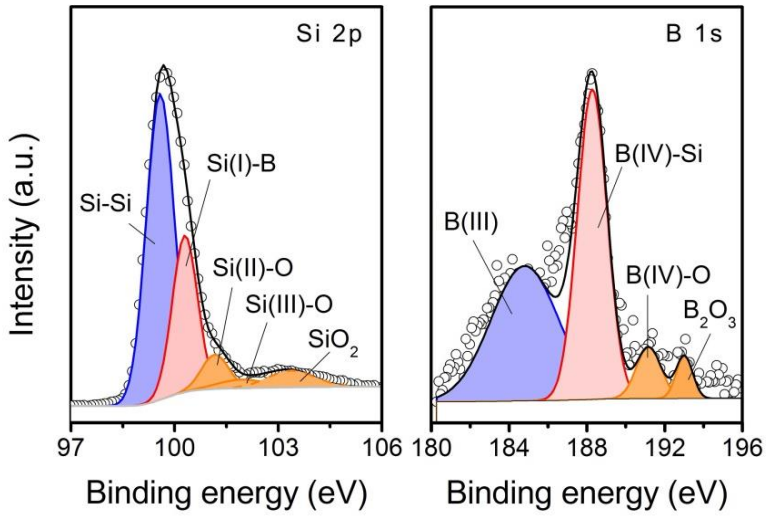

Figure 4.7. X-ray photoelectron spectra of heavily B-doped Si NCs.. The Si 2p spectrum of heavily B-doped Si NCs can be decomposed into five constituent peaks at 99.5, 100.2, 101.1, 101.9 and 103.3 eV. The neutral state peak at 99.5 eV (blue) is related to the Si-Si bond, while the other four high valent state peaks (Si(I), Si(II), Si(III) and Si(IV)) (orange) are due to the Si atoms bonded with B and oxygen (O). In the B 1s spectrum the peaks at 184.8 (blue) and 188.3 eV (red) originate from the B atoms bonded to three Si atoms (B(III)-Si) and B atoms bonded to four Si atoms (B(IV)-Si), respectively. The two higher energy peaks at 191.2 and 193.0 eV (orange) are due to B atoms bonded with O. The concentration of B for heavily doped Si NCs is ~ 7%.

It has been previously shown that in B and phosphorous (P) codoped Si NCs a negative potential occurs at the NC surface because of ionized B atoms at the surface side and ionized P atoms at the core side.[44] We believe that ionized B atoms at the surface/subsurface of heavily B-doped Si NCs produce a negative potential that is strong enough to effectively retard the agglomeration of heavily B-doped Si NCs in the current work. Indeed we have measured a zeta potential of -26 mV for the heavily B-doped Si NCs in benzonitrile, approaching ± 30 mV which is usually considered to be sufficient for long-term stability. It appears that a thin oxide

layer at the surface of heavily B-doped Si NCs cannot seriously screen the B-induced negative potential at the NC surface. This explains the excellent colloidal stability of heavily B-doped Si NCs during long-time storage in air.

4.4.2 Direct and Indirect Electronic Transitions

The excellent dispersion of heavily B-doped Si NCs in benzonitrile facilitates the study on the electronic transitions of heavily B-doped Si NCs by using optical absorption measurements. Figure 4.8(a) shows the optical absorption spectra of heavily B-doped Si NCs in benzonitrile. The optical absorption spectrum of Cl-passivated Si NCs in benzonitrile is also included for comparison. As an indirect bandgap semiconductor, bulk Si is characteristic of an indirect $\Gamma-X$ transition (T_0) and a direct $\Gamma-\Gamma$ transition (T_1) (inset of Figure 4.8(a)). As expected from the Mie theory,[45,46] a shoulder associated with the T_1 transition can be identified in each spectrum in Figure 4.8(a). However, we do not observe a clear sign for the T_0 transition from the spectra, largely due to the weak band-edge absorption of Si.[47] The energy of the T_1 transition (E_1) can be determined by examining the derivation of an absorption spectrum, as demonstrated in Figure 4.8(b). Specifically, Cl-passivated Si NCs show the T_1 transition at 3.58 eV, similar to that obtained by Gresback et al..[45] As the B concentration increases from ~ 7% to 31%, the T_1 transition monotonically red-shifts from 3.55 to 3.06 eV.

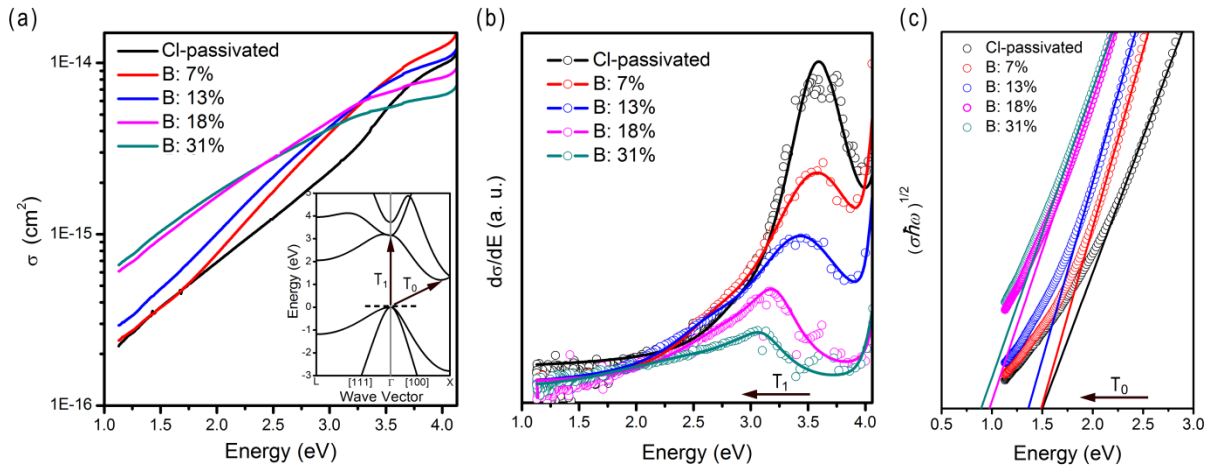

Figure 4.8. (a) Per-NC absorption spectra of Cl-passivated Si NCs and heavily B-doped Si NCs in benzonitrile. The inset shows the band structure of bulk Si in which the indirect phonon-assisted Γ—X transition (T_0) and direct Γ—Γ (T_1) transition are indicated. (b) Derivative absorption spectra of Cl-passivated Si NCs and heavily B-doped Si NCs in benzonitrile. (c) Absorption data for Cl-passivated Si NCs and heavily B-doped Si NCs in benzonitrile plotted as $(\sigma\hbar\omega)^{1/2}$. The concentration of B are ~ 7%, 13%, 18% and 31%.

To investigate whether heavy B doping also leads to the change of the T_0 transition, we employ the Tauc law to analysis the optical absorption spectra.[48] For an indirect semiconductor, the relationship between absorption cross section (σ) and the energy of the T_0 transition (E_0) is given by[49]

$$\sigma\hbar\omega \propto \omega^{-1}(\hbar\omega - E_0)^2, \tag{4.1}$$

where $\hbar\omega$ is the photon energy. According to Eq. (4.1), each optical absorption spectrum in Figure 4.8(a) is replotted, leading to the results shown in Figure 4.8(c). We see that there is a soft onset, followed by an almost linear increase in each spectrum. E_0 can be extracted by fitting the linear increase of each curve in Figure 4.8(c). For Cl-passivated Si NCs, we obtain that E_0 is 1.5 eV, consistent with the quantum confinement effect.[50] After Si NCs are heavily doped with B E_0

red-shifts. When the concentration of B reaches ~ 31%, E_0 decreases to be 0.9 eV. The apparent red-shift of the absorption onset (i.e., T_0) is actually consistent with the change of Si NC color from dark yellow to black as the doping level of B increases, as shown in Figure 4.9.

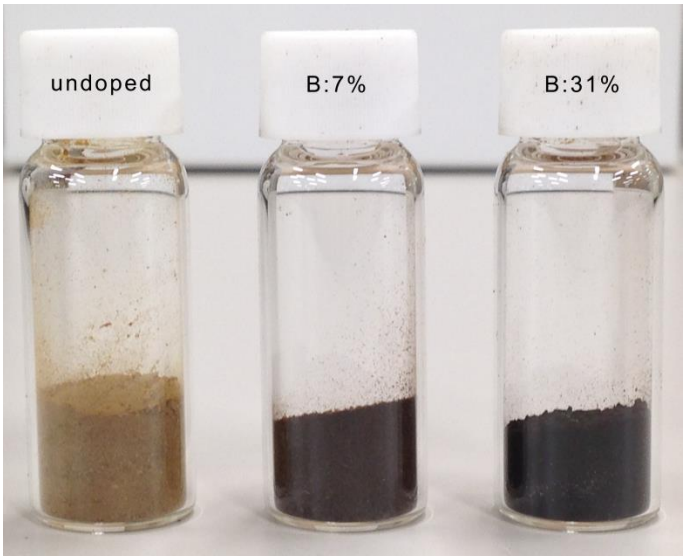

Figure 4.9. Photograph of undoped and heavily B-doped SiNC powders. With the increase of B doping level, the color of Si NCs changes from dark yellow to black, indicating the red-shift of the optical absorption onset.

4.4.3 Bandgap Narrowing

Figure 4.10 shows the FTIR spectra of undoped and heavily B-doped Si NCs. Heavy B doping leads to a broad absorption peak which blue-shifts from ~ 1528 to 3020 cm^{-1} with the increase of B doping level. This is characteristic of the heavy-doping-induced LSPR of Si NCs.[8,9,11,29] After analyzing the LSPR-induced absorption peak of heavily B-doped Si NCs by using the Mie absorption theory with the Drude contribution,[9] we obtain that free carrier (hole) concentrations of Si NCs doped with ~ 7%, 13%, 18% and 31% B are ~ 1.4×10^{20}, 2.0×10^{20}, 4.1×10^{20} and 4.9×10^{20} cm^{-3}, respectively. Clearly, there is a great deal of unionized B atoms in Si NCs despite the current rather high free carrier concentrations. In the meantime, we should

note that the high free carrier concentrations in heavily B-doped Si NCs are consistent with the aforementioned red-shifts of T_0 and T_1 (i.e., bandgap narrowing) if we assume the similarity of Si NCs to bulk Si.[51-53]

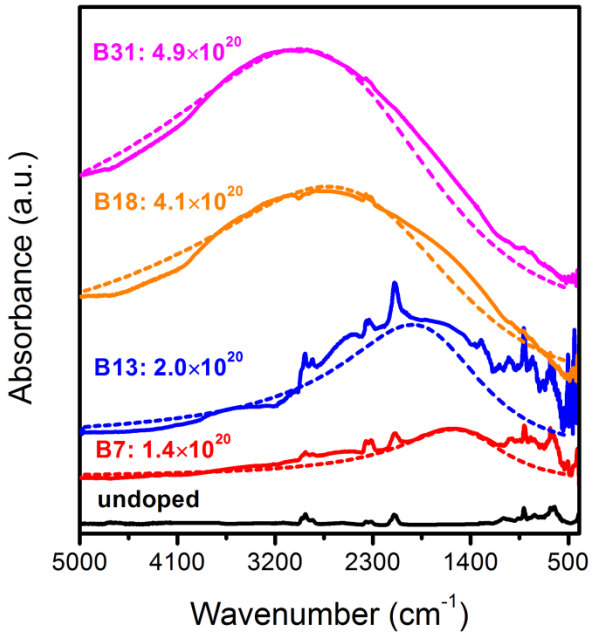

Figure 4.10. FTIR spectra of undoped and heavily B-doped Si NCs after HF vapor etching. The dash lines show the fitting of LSPR-induced absorption for each heavily B-doped Si NCs by using the Drude model. The free carrier concentrations obtained from the fitting are also indicated in the bracket.

Figure 4.11 shows the dependence of the bandgap narrowing on the ionized impurity concentration. It is seen that the narrowing of T_1 is basically consistent with that of T_0 as the ionized impurity concentration varies. This may be because heavy B doping introduces an impurity band close to the valence band at the Γ point. [53] In the meantime, the conduction band at both the Γ and X points moves toward the bandgap.[52,54] Therefore, the T_0 and T_1 transitions are

nearly equally affected. It is known that in bulk Si the bandgap narrowing (ΔE_g) is given as a function of the concentration (N) of ionized impurity:[51]

$$\Delta E_g = C_1 \left\{ \ln\left(\frac{N}{N_1}\right) + \sqrt{\left[\ln\left(\frac{N}{N_1}\right)\right]^2 + C_2} \right\}, \quad (4.2)$$

where N_1 is a critical parameter, indicating the onset of the bandgap narrowing. C_1 and C_2 are constants. Figure 4.11 shows the typical fit for the bandgap narrowing of heavily B-doped Si NCs by use of Eq. (4.2). The value of N_1 derived from the fitting is 1.8×10^{20} cm^{-3}. This means that the bandgap of Si NCs starts decreasing when the ionized B concentration is larger than 1.8×10^{20} cm^{-3}. Such a critical value is more than three orders of magnitude higher than that obtained for heavily B-doped bulk Si (1.3×10^{17} cm^{-3}).[55] The quantum confinement effect may cause the energy levels of B to be deeper in the bandgap for Si NCs than bulk Si.[56,57] Therefore, a much larger B concentration is needed to form an impurity band extending to the valence band and narrow the bandgap in Si NCs than in bulk Si. Moreover, C_1 increases from 6.7 for B-doped bulk Si to 270 for heavily B-doped Si NCs, indicating that the bandgap shrinks more significantly in Si NCs than in bulk Si. This may be due to the fact that a number of unionized B atoms give rise to increased disorder in Si NCs, causing the dispersion of impurity energy levels to increase.[58,59] Therefore, the shrinking of the bandgap of Si NCs is enhanced.

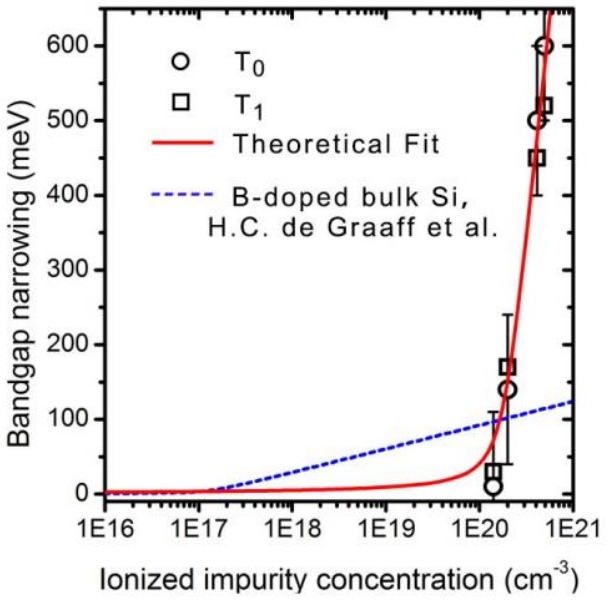

Figure 4.11. Bandgap narrowing associated with the indirect transition (T_0) and direct transition (T_1) obtained in heavily B-doped Si NCs. Graaff et al.' results for bandgap narrowing in heavily B-doped bulk Si[55] are shown for comparision.

After heavy B doping the Fermi level (E_f) should enter the original valence band, leading to the degeneracy of the valence band.[60] The free carrier (hole) concentration (p) is related to the energy difference between the Fermi level and original valence-band edge ($E_v - E_f$) as[60]

$$p = \frac{2(2\pi m_h k_0 T)^{3/2}}{h^3} \frac{2}{\sqrt{\pi}} \int_0^\infty \frac{x^{1/2}}{1+e^{\left(x-\frac{E_v-E_f}{k_0 T}\right)}} dx \ , \qquad (4.3)$$

where m_h is the effective mass of a hole, T is temperature, h is Planck constant, k_0 is Boltzmann constant. We work out that E_v-E_f are ~ 0.15, 0.19, 0.31 and 0.35 eV when Si NCs are doped with ~ 7%, 13%, 18% and 31% B, respectively.

The position of Fermi level and valence band edge may be investigated by using ultraviolet photoelectron spectroscopy (UPS). Figure 4.12 shows the schematic of photoemission spectroscopy for both undoped and B heavy-doped Si NCs. Free electrons with certain kinetic energy (E_{kin}) generated by external photoelectric effect depends on the exciting photon energy ($h\nu$), the ionization energy (E_{ion}) (or the work function (Φ_s)), the binding energy (E_b) of the excited electron, and inelastic scattering processes in the sample. The resulting spectrum (the pink area in Figure 4.12) is a superposition of the primary electrons with a E_{kin} distribution mirroring (in first order approximation) the density of states in the valence band (the grey area in Figure 4.12) of the sample, and the secondary electron continuum. For the undoped Si NC sample in Figure 4.12(a), the Fermi level (E_f) is located at the middle of the bandgap between the conduction band (CB) and valence band (VB). So the fastest electrons of this spectrum will be primary electrons that emitted directly from the valence-band edge, having $E_{kin}= h\nu - E_{ion}$. The slowest electrons will be secondary electrons that are just able to make out of the sample, having $E_{kin}= 0$ eV. While for the heavily B-doped Si NC sample in Figure 4.12(b), the fastest electrons will be those emitted directly from the Fermi level, having $E_{kin}= h\nu - \Phi_s$ because E_f has entered the orignal valence band (VB (ori)). The slowest electrons will still be secondary electrons, having $E_{kin}= 0$ eV. Therefore, a shift of the E_{kin} associated with the fasted electtrons (ΔE_{kin}) towards the lower kinetic energy region in the spectrum of Si NCs would be expected after heavy B doping, which can be expresed as $\Delta E_{kin} = (E_{VB(ori)} - E_f)$. With the increase of the B doping level, both the Fermi level and the original valence band move downward, resulting in the further shift of E_{kin} towards the lower kinetic energy region, which can be expressed as $\Delta E_{kin} = (E_{VB(ori)} - E_{VB}) + (E_{VB} - E_f)$, as shown in Figure 4.12(c).

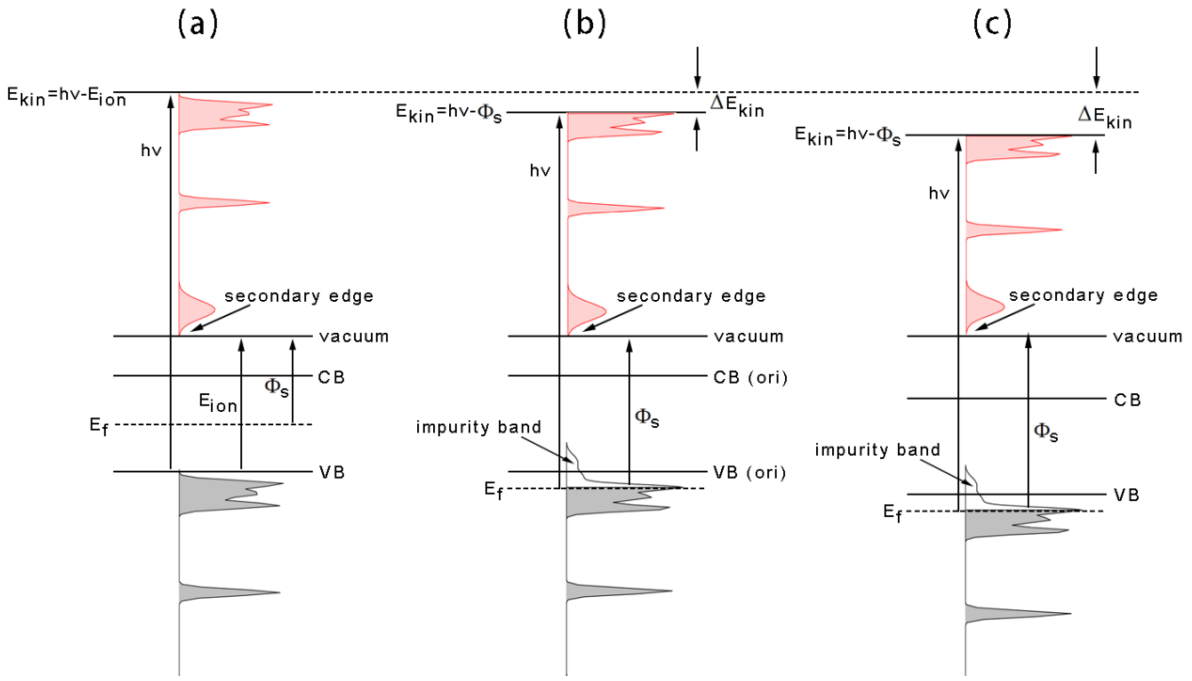

Figure 4.12. Schematic of photoemission spectroscopy of (a) undoped and (b), (c) heavily B-doped Si NC samples. The B doping level increases from (b) to (c).

To examine the shift of the Fermi level into the valence band we have carried out UPS measurements for both undoped and heavily B-doped Si NCs. The results are shown in Figure 4.13. The UPS spectra are obtained by using a 21.2 eV He-Ia source with an applied bias voltage of −9.8 eV to separate the secondary electron edges between a sample and the spectrometer. It is seen that the secondary electron backgrounds of all Si NCs cut off at 13.6 eV, as indicated by the dash line in Figure 4.13(a). Therefore, we can evaluate the position of the Fermi level from the change of the valence-band edge.[61] Inset of Figure 4.13(a) shows the magnified spectra in the Si valence-band-edge region. Ideally, the valence-band edges should be infinitely abrupt. However, due to limited instrument resolution and thermal effect they are broadened. The actual positions of the edges can be determined as the centers of the slope, as shown in Figure 4.13(b).[62] For

undoped Si NCs we obtain that the valence band edge cuts off at 29.7 eV. The ionization energy of undoped Si NCs is thus calculated to be 5.1 eV (Figure 4.12(a)), which is 0.2 eV larger than that of bulk Si (4.9 eV).[63] This is in good agreement with the valence band shift induced by quantum confinement effect.[64] With the B doping level increases to 31% the valence band edge monotonically shifts from 29.7 eV to 29.1 eV. The shift of the valence-band edge (ΔE_{kin}) and $E_v - E_f$ obtained from Eq. (3) are compared in Figure 4.13(c). It is found that ΔE_{kin} agrees with $E_v - E_f$. when the ionized impurity concentration is $< 2\times10^{20}$ cm^{-3}. This suggests the redshift of the valence band edge is basically due to the move of the Fermi level into the original valence band (Figure 4.12(b)). As the ionized impurity concentration increases to be $>2\times10^{20}$ cm^{-3}, ΔE_{kin} significantly exceeds $E_v - E_f$. For Si NCs doped with B at the highest concentration of 31%, the obtained ΔE_{kin} is 0.6 eV, which is nearly two times larger than $E_v - E_f$. This indicates that the original valence band edge also moves downward in addition to the Fermi level moving into the original valence band (Figure 4.12(c)). The decrease of the original valence band edge is possibly due to the tensile strain induced by heavy B doping.[23,65,66]

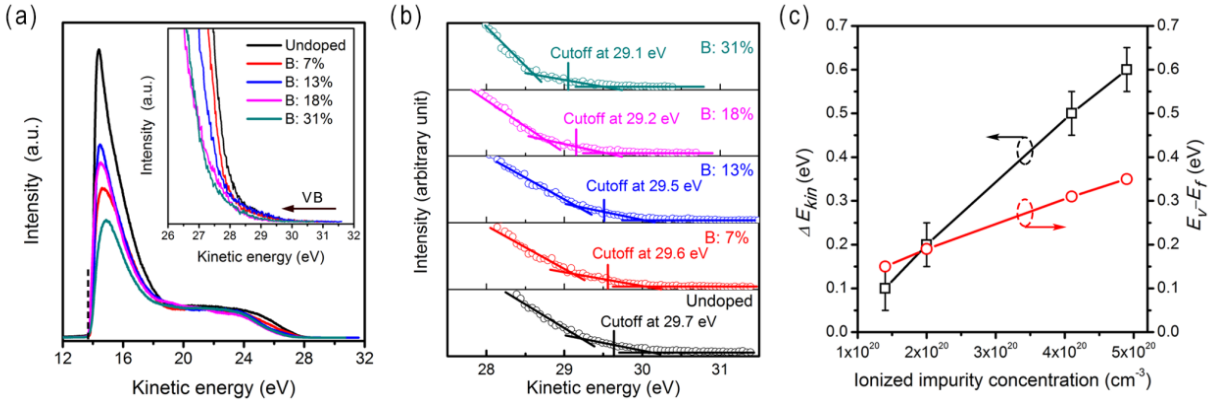

Figure 4.13. (a) UPS spectra of undoped and heavily B-doped Si NCs. The inset shows the magnified spectra in the Si valence-band-edge region. (b) The valence-band edges of undoped and heavily B-doped Si NCs taken

as the center of the slope indicated by the verticle lines. (c) Comparision of the shift of valence band edge (ΔE_{kin}) and E_v-E_f calculated from Eq. 4.3.

If the move of the conduction band toward the bandgap was less significant than that of the Fermi level into the original valence band, the widening of the indirect/direct (optical) bandgap (the increase of E_0/E_1), i.e., the so-called Burstein-Moss shift,[67] would be observed. Since we actually observe the decrease of both E_0 and E_1 after heavy B doping, the conduction band ought to significantly move toward the bandgap as the Fermi level enters the original valence band, as schematically shown in Figure 4.14. With the increase of the B concentration, the B-induced impurity band becomes more extended to occupy larger part of the original bandgap. In the meantime, the conduction band more significantly moves toward the bandgap, while the Fermi level basically remains within the top region of the original valence band. This explains the continuous red-shift of the optical absorption with the increase of the B concentration. Because the B-induced impurity band is merged with the original valence band after heavy B doping, free holes above the Fermi level are largely from the B-induced impurity band. The collective oscillation of these free holes should occur under external excitation, leading to LSPR.[29]

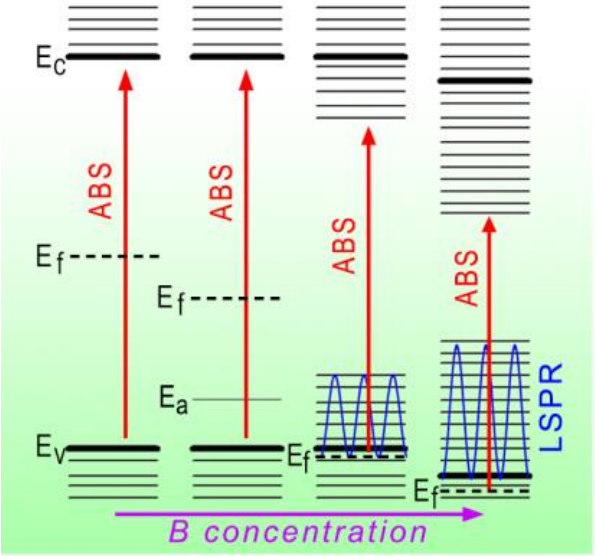

Figure 4.14. Evolution of the Si NC band structure with the increase of the doping level of B. The B concentration increases from left to right. ABS, absorption onset; E_c, conduction band edge; E_v, valence band edge; E_f, Fermi energy level; E_a, impurity energy level.

4.5 Conclusions

In summary, tunable plasmonic properties and colloidal stability without the use of ligands are demonstrated for heavily B-doped Si NCs. Ionized B atoms induce a negative potential at the NC surface, which is proposed to be responsible for the colloidal stability of Si NCs in solvent. Heavily B-doped Si NC colloids are found to be stable in air for months, making them suitable for the device processing in ambient atmosphere. The effect of heavy B doping on the band structure of Si NCs has been explored by optical absorption. It is found that heavy B doping significantly decreases the energies of both the indirect and direct electronic transitions in Si NCs. This decrease could be interpreted by the move of the conduction band toward the bandgap, which could be more significant than that of the Fermi level into the valence band. The

plasmonic and sub-interband absorption of Si NCs enabled by heavy B doping is located in the infrared regime in the current work, which should be helpful to the development of novel Si-based optoelectronic structures and devices.[68]

4.6 References

[1] Liu, X.; Swihart, M. T. Heavily-Doped Colloidal Semiconductor and Metal Oxide Nanocrystals: An Emerging New Class of Plasmonic Nanomaterials. *Chem. Soc. Rev.* **2014**, *43*, 3908-3920.

[2] Naik, G. V.; Shalaev, V. M.; Boltasseva, A. Alternative Plasmonic Materials: Beyond Gold and Silver. *Adv. Mater.* **2013**, *25*, 3264-3294.

[3] Faucheaux, J. A.; Stanton, A. L. D.; Jain, P. K. Plasmon Resonances of Semiconductor Nanocrystals: Physical Principles and New Opportunities. *J. Phys. Chem. Lett.* **2014**, *5*, 976-985.

[4] Luther, J. M.; Jain, P. K.; Ewers, T.; Alivisatos, A. P. Localized Surface Plasmon Resonances Arising From Free Carriers in Doped Quantum Dots. *Nat. Mater.* **2011**, *10*, 361-366.

[5] Manthiram, K.; Alivisatos, A. P. Tunable Localized Surface Plasmon Resonances in Tungsten Oxide Nanocrystals. *J. Am. Chem. Soc.* **2012**, *134*, 3995-3998.

[6] Buonsanti, R.; Llordes, A.; Aloni, S.; Helms, B. A.; Milliron, D. J. Tunable Infrared Absorption and Visible Transparency of Colloidal Aluminum-Doped Zinc Oxide Nanocrystals. *Nano Lett.* **2011**, *11*, 4706-4710.

[7] Kanehara, M.; Koike, H.; Yoshinaga, T.; Teranishi, T. Indium Tin Oxide Nanoparticles with Compositionally Tunable Surface Plasmon Resonance Frequencies in the Near-IR Region. *J. Am. Chem. Soc.* **2009**, *131*, 17736-17737.

[8] Rowe, D. J.; Jeong, J. S.; Mkhoyan, K. A.; Kortshagen, U. R. Phosphorus-Doped Silicon Nanocrystals Exhibiting Mid-Infrared Localized Surface Plasmon Resonance. *Nano Lett.* **2013**, *13*, 1317-1322.

[9] Zhou, S.; Pi, X.; Ni, Z.; Ding, Y.; Jiang, Y.; Jin, C.; Delerue, C.; Yang, D.; Nozaki, T. Comparative Study on the Localized Surface Plasmon Resonance of Boron- and Phosphorus-Doped Silicon Nanocrystals. *ACS Nano* **2015**, *9*, 378-386.

[10] Schimpf, A. M.; Knowles, K. E.; Carroll, G. M.; Gamelin, D. R. Electronic Doping and Redox-Potential Tuning in Colloidal Semiconductor Nanocrystals. *Acc. Chem. Res.* **2015**, *48*, 1929-1937.

[11] Kramer, N. J.; Schramke, K. S.; Kortshagen, U. R. Plasmonic Properties of Silicon Nanocrystals Doped with Boron and Phosphorus. *Nano Lett.* **2015**, *15*, 5597-5603.

[12] Habas, S. E.; Platt, H. A. S.; van Hest, M. F. A. M.; Ginley, D. S. Low-Cost Inorganic Solar Cells: From Ink to Printed Device. *Chem. Rev.* **2010**, *110*, 6571-6594.

[13] Williams, B. A.; Mahajan, A.; Smeaton, M. A.; Holgate, C. S.; Aydil, E. S.; Francis, L. F. Formation of Copper Zinc Tin Sulfide Thin Films from Colloidal Nanocrystal Dispersions via Aerosol-Jet Printing and Compaction. *ACS Appl. Mater. Interfaces* **2015**, *7*, 11526-11535.

[14] Pi, X. D.; Zhang, L. Yang, D. R. Enhancing the Efficiency of Multicrystalline Silicon Solar Cells by the Inkjet Printing of Silicon-Quantum-Dot Ink. *J. Phys. Chem. C* **2012**, *116*, 21240–21243.

[15] Kim, B. H.; Onses, M. S.; Lim, J. B.; Nam, S.; Oh, N.; Kim, H.; Yu, K. J.; Lee, J. W.; Kim, J. H.; Kang, S. K.; Lee, C. H.; Lee, J.; Shin, J. H.; Kim, N. H.; Leal, C.; Shim, M.; Rogers, J. A. High-Resolution Patterns of Quantum Dots Formed by Electrohydrodynamic Jet Printing for Light-Emitting Diodes. *Nano Lett.* **2015**, *15*, 969-973.

[16] Luther, J. M.; Law, M.; Song, Q.; Perkins, C. L.; Beard, M. C.; Nozik, A. J. Structural, Optical and Electrical Properties of Self-Assembled Films of PbSe Nanocrystals Treated with 1,2-ethanedithiol. *ACS Nano* **2008**, *2*, 271-280.

[17] Heath, J. R.; Shiang, J. J. Covalency in Semiconductor Quantum Dots. *Chem. Soc. Rev.* **1998**, *27*, 65-71.

[18] Murray, C. B.; Norris, D. J.; Bawendi, M. G. Synthesis and Characterization of Nearly Monodisperse CdE (E = S, Se, Te) Semiconductor Nanocrystallites. *J. Am. Chem. Soc.* **1993**, *115*, 8706-8715.

[19] Veinot, J. G. C. Synthesis, Surface Functionalization, and Properties of Freestanding Silicon Nanocrystals. *Chem. Commun.* **2006**, 4160-4168.

[20] Mangolini, L.; Kortshagen, U. Plasma-Assisted Synthesis of Silicon Nanocrystal Inks. *Adv. Mater.* **2007**, *19*, 2513-2519.

[21] Yin Y.; Alivisatos, A. P. Colloidal Nanocrystal Synthesis and the Organic–Inorganic Interface. *Nature.* **2005**, *437*, 664-670.

[22] Norris, D. J.; Efros, A. L.; Erwin, S. C. Doped Nanocrystals. *Science* **2008**, *319*, 1776-1779.

[23] Zhou, S.; Pi, X. D.; Ni, Z. Y.; Luan, Q. B.; Jiang, Y. Y.; Jin, C. H.; Nozaki, T.; Yang, D. Boron- and Phosphorus-Hyperdoped Silicon Nanocrystals. Part. Part. Syst. Charact. **2014**, *32*, 213–221.

[24] Erwin, S. C.; Zu, L.; Haftel, M. I.; Efros, A. L.; Kennedy, T. A.; Norris, D. J. Doping Semiconductor Nanocrystals. *Nature* **2005**, *436*, 91-94.

[25] Law, M.; Luther, J. M.; Song, O.; Hughes, B. K.; Perkins, C. L.; Nozik, A. J. Structural,

Optical, and Electrical Properties of PbSe Nanocrystal Solids Treated Thermally or with Simple Amines. *J. Am. Chem. Soc.* **2008**, *130*, 5974-5985.

[26] Chen, T.; Skinner, B.; Xie, W.; Shklovskii, B. I.; Kortshagen, U. R. Carrier Transport in Films of Alkyl-Ligand-Terminated Silicon Nanocrystals. *J. Phys. Chem. C* **2014**, *118*, 19580-19588.

[27] Talapin, D. V.; Murray, C. B. PbSe Nanocrystal Solids for N- and P-Channel Thin Film Field-Effect Transistors. *Science* **2005**, *310*, 86-89.

[28] Zabet-Khosousi, A.; Dhirani, A. A. Charge Transport in Nanoparticle Assemblies. *Chem. Rev.* **2008**, *108*, 4072-4124.

[29] Pi, X. D.; Delerue, C. Tight-Binding Calculations of the Optical Response of Optimally P-Doped Si Nanocrystals: A Model for Localized Surface Plasmon Resonance. *Phys. Rev. Lett.* **2013**, *111*, 177402.

[30] Wheeler, L. M.; Neale, N. R.; Chen, T.; Kortshagen, U. R. Hypervalent Surface Interactions for Colloidal Stability and Doping of Silicon Nanocrystals. *Nat. Commun.* **2013**, *4*, 2197-2206.

[31] Zhou, S.; Ding, Y.; Pi, X.; Nozaki, T. Doped Silicon Nanocrystals from Organic Dopant Precursor by a $SiCl_4$-Based High Frequency Nonthermal Plasma. *Appl. Phys. Lett.* **2014**, *105*, 183110.

[32] Gresback, R.; Nozaki, T.; Okazaki, K. Synthesis and Oxidation of Luminescent Silicon Nanocrystals from Silicon Tetrachloride by Very High Frequency Nonthermal Plasma. *Nanotechnology* **2011**, *22*, 305605.

[33] Zou, J.; Kauzlarich, S. Functionalization of Silicon Nanoparticles via Silanization: Alkyl, Halide and Ester. *J. Clust. Sci.* **2008**, *19*, 341-355.

[34] Nozaki, T.; Sasaki, K.; Ogino, T.; Asahi, D.; Okazaki, K. Microplasma Synthesis of Tunable Photoluminescent Silicon Nanocrystals. *Nanotechnology* **2007**, *18*, 235603

[35] Mangolini, L.; Thimsen, E.; Kortshagen, U. High-Yield Plasma Synthesis of Luminescent Silicon Nanocrystals. *Nano Lett.* **2005**, *5*, 655-659.

[36] Pi, X.; Li, Q.; Li, D.; Yang, D. Spin-Coating Silicon-Quantum-Dot Ink to Improve Solar Cell Efficiency. *Solar Energy Mater. Solar Cells* **2011**, *95*, 2941-2945.

[37] Pi, X. D.; Gresback, R.; Liptak, R. W.; Campbell, S. A.; Kortshagen, U. Doping Efficiency, Dopant Location, and Oxidation of Si Nanocrystals. *Appl. Phys. Lett.* **2008**, *92*, 123102.

[38] Niesar, S.; Pereira, R. N.; Stegner, A. R.; Erhard, N.; Hoeb, M.; Baumer, A.; Wiggers, H.; Brandt, M. S.; Stutzmann, M. Low-Cost Post-Growth Treatments of Crystalline Silicon Nanoparticles Improving Surface and Electronic Properties. *Adv. Fun. Mat.* **2012**, *22*, 1190-1198.

[39] Erogbogbo, F.; Liu, T.; Ramadurai, N.; Tuccarione, P.; Lai, L.; Swihart, M. T.; Prasad, P. N.

Creating Ligand-Free Silicon Germanium Alloy Nanocrystal Inks. *ACS Nano* **2011**, *5*, 7950-7959.

[40] Holman, Z. C.; Kortshagen, U. R. Nanocrystal Inks without Ligands: Stable Colloids of Bare Germanium Nanocrystals. *Nano Lett.* **2011**, *11*, 2133-2136.

[41] Pi, X. D.; Mangolini, L.; Campbell, S. A.; Kortshagen, U. Room-Temperature Atmospheric Oxidation of Si Nanocrystals after HF Etching. *Phys. Rev. B* **2007**, *75*, 085423.

[42] Sato, K.; Fukata, N.; Hirakuri, K. Doping and Characterization of Boron Atoms in Nanocrystalline Silicon Particles. *Appl. Phys. Lett.* **2009**, *94*, 161902.

[43] Tomio, K.; Masataka, H. Coordination Number of Doped Boron Atoms in Photochemically-Deposited Amorphous Silicon Studied by X-Ray Photoelectron Spectroscopy. *Jpn. J. Appl. Phys.* **1986**, *25*, L75-L77.

[44] Sugimoto, H.; Fujii, M.; Imakita, K.; Hayashi, S.; Akamatsu, K. Phosphorus and Boron Codoped Colloidal Silicon Nanocrystals with Inorganic Atomic Ligands. *J. Phys. Chem. C* **2013**, *117*, 6807-6813.

[45] Gresback, R.; Murakami, Y.; Ding, Y.; Yamada, R.; Okazaki, K.; Nozaki, T. Optical Extinction Spectra of Silicon Nanocrystals: Size Dependence upon the Lowest Direct Transition. *Langmuir* **2013**, *29*, 1802-1807.

[46] Holman, Z. C.; Kortshagen, U. R. Absolute Absorption Cross Sections of Ligand-Free Colloidal Germanium Nanocrystals. *Appl. Phys. Lett.* **2012**, *100*, 133108.

[47] Corkish, R.; Green, M. A. Band Edge Optical Absorption in Intrinsic Silicon: Assessment of the Indirect Transition and Disorder Models. *J. Appl. Phys.* **1993**, *73*, 3988-3996.

[48] Tauc, J. Optical Properties and Electronic Structure of Amorphous Ge and Si. *Mat. Res. Bull.* **1968**, *3*, 37-46.

[49] Meier, C.; Gondorf, A.; Luettjohann, S.; Lorke, A.; Wiggers, H. Silicon Nanoparticles: Absorption, Emission, and the Nature of the Electronic Bandgap. *J. Appl. Phys.* **2007**, *101*, 103112.

[50] Delerue, C.; Allan, G.; Lannoo, M. Theoretical Aspects of the Luminescence of Porous Silicon. *Phys. Rev. B* **1993**, *48*, 11024-11036.

[51] Klaassen, D. B. M.; Slotboom, J. W.; Degraaff, H. C. Unified Apparent Bandgap Narrowing in N-Type and P-Type Silicon. *Solid-St. Electron.* **1992**, *35*, 125-129.

[52] Wagner, J.; del Alamo, J. A. Bandgap Narrowing in Heavily Doped Silicon: A Comparison of Optical and Electrical Data. *J. Appl. Phys.* **1988**, *63*, 425-429.

[53] Viña, L.; Cardona, M. Effect of Heavy doping on the Optical Properties and the Band Structure of Silicon. *Phys. Rev. B* **1984**, *29*, 6739-6751.

[54] Teeffelen, S. V.; Persson, C.; Eriksson, O.; Johansson, B. Doping-Induced Bandgap Narrowing in Si Rich N- and P-Type $Si_{1-x}Ge_x$. *J. Phys.: Condens. Matter* **2003**, *15*, 489.

[55] Slotboom, J. W.; Degraaff, H. C. Measurements of Bandgap Narrowing in Si Bipolar-Transistors. *Solid-St. Electron.* **1976**, *19*, 857-862.

[56] Nakamura, T.; Adachi, S.; Fujii, M.; Sugimoto, H.; Miura, K.; Yamamoto, S. Size and Dopant-Concentration Dependence of Photoluminescence Properties of Ion-Implanted Phosphorus- and Boron-Codoped Si Nanocrystals. *Phys. Rev. B* **2015**, *91*, 165424.

[57] Pi, X. D.; Chen, X. B.; Yang, D. R. First-Principles Study of 2.2 nm Silicon Nanocrystals Doped with Boron. *J. Phys. Chem. C* **2011**, *115*, 9838-9843.

[58] Suergers, C.; Wenderoth, M.; Loeser, K.; Garleff, J. K.; Ulbrich, R. G.; Lukas, M.; v Loehneysen, H. Electronic Disorder of P- and B-Doped Si at the Metal-Insulator Transition Investigated by Scanning Tunnelling Microscopy and Electronic Transport. *New J. Phys.* **2013**, *15*, 055009.

[59] Blase, X.; Bustarret, E.; Chapelier, C.; Klein, T.; Marcenat, C. Superconducting Group-IV Semiconductors. *Nat. Mater.* **2009**, *8*, 375-382.

[60] Sze, S. M. Physics of Semiconductor Devices; John Wiley & Sons: New York, **1969**; pp 151-156.

[61] Hao, P. H.; Hou, X. Y.; Zhang, F. L.; Wang, X. Energy Band Lineup at the Porous-Silicon/Silicon Heterointerface Measured by Electron Spectroscopy. *Appl. Phys. Lett.* **1994**, *64*, 3602-3604.

[62] Park, Y.; Choong, V.; Gao, Y.; Hsieh, B. R.; Tang, C. W. Work Function of Indium Tin Oxide Transparent Conductor Measured by Photoelectron Spectroscopy. *Appl. Phys. Lett.* **1996**, *68*, 2699-2701.

[63] Melnikov, D. V.; Chelikowsky, J. R. Electron Affinities and Ionization Energies in Si and Ge Nanocrystals. *Phys. Rev. B* **2004**, 6*9*, 113305.

[64] Van Buuren, T.; Dinh, L. N.; Chase, L. L.; Siekhaus, W. J.; Terminello, L. J. Changes in the Electronic Properties of Si Nanocrystals as a Function of Particle Size. *Phys. Rev. Lett.* **1998**, *80*, 3803-3806.

[65] Kůsová, K.; Hapala, P.; Valenta, J.; Jelínek, P.; Cibulka, O.; Ondič, L.; Pelant, I. Direct Bandgap Silicon: Tensile-Strained Silicon Nanocrystals. *Adv. Mater. Interfaces.* **2014**, *1*, 1300042.

[66] Hong, K-H.; Kim, J.; Lee, S-H.; Shin, J K. Strain-Driven Electronic Band Structure Modulation of Si Nanowires. *Nano Lett.* **2008**, *8*, 1335-1340.

[67] Kamat, P. V.; Dimitrijevic, N. M.; Nozik, A. J. Dynamic Burstein-Moss Shift in Semiconductor Colloids. *J. Phys. Chem.* **1989**, *93*, 2873-2875.

(68] Rogalski, A. Infrared Detectors: Status and Trends. *Prog. Quantum Electron.* **2003**, *27*, 59-210.

Chapter 5: Low-cost Synthesis of Doped Silicon Nanocrystals and Their Application in Hybrid Photovoltaics *

***** Portions of this chapter are adapted from the publication authored by Shu Zhou, Yi Ding, Xiaodong Pi, and Tomohiro Nozaki in Applied Physics Letters. (*Applied Physics Letters,* 105, 183110, (2014))

5.1 Abstract

Doped silicon nanocrystals (Si NCs) are of great interest in demanding low-cost nano-devices because of the abundance and nontoxicity of Si. Here we demonstrate a cost-effective gas phase approach to successfully synthesize phosphorous (P) -doped Si NCs in which the precursors used, i.e. $SiCl_4$, trimethyl phosphite (TMP), are both safe and economical. It is found that the TMP-enabled P-doping does not change the crystalline structure of Si NCs. The surface of P-doped Si NCs is terminated by both Cl and H. The Si-H bond density at the surface of P-doped Si NCs is found to be much higher than that of undoped Si NCs. The X-ray photoelectron spectroscopy and electron spin resonance results suggest P atoms are doped into the substitutional site of the Si-NC core and electrically active in Si NCs. Unintentional impurities such as carbon contained in TMP are not introduced into Si NCs. The use of these doped Si NCs in hybrid solar cells results in slight increase of open-circuit voltage (V_{oc}), but significant drop of short-circuit current density (J_{sc}), due to the donor-induced recombination of free charged carriers in the bulk absorber.

5.2 Introduction

The doping of bulk silicon (Si) has boosted semiconductor industry in a variety of fields including microelectronics[1], optoelectronics[2] and photovoltaics[3]. The key role that dopants act in bulk Si has encouraged research on doping Si NCs for controllable electrical and optical properties[4-9]. Despite the wide potential applications in nano-devices[10], the synthesis of doped Si NCs is always critical. Nonthermal plasma has been well established in the past few years for synthesizing free-standing doped Si NCs[11-14]. The great flexibility of nonthermal plasma technique in tuning the size and dopant concentration of Si NCs has enabled distinct electrical and optical properties. Localized surface plasmon resonance that are known limited to noble metals in the past, has been recently demonstrated in nonthermal plasma synthesized Boron (B)- and Phosphorous (P)-doped Si NCs, respectively[13, 15]. Nevertheless, it is always neglected that most of the precursors used in nonthermal plasma for synthesizing doped Si NCs by now (SiH_4, PH_3, B_2H_6 et al.) are either toxic or expensive. This will seriously offset the priority of Si (e.g. abundance and nontoxicity). Effort has thus been initialed by using $SiCl_4$ in place of SiH_4 because $SiCl_4$ is much safer and more economical than SiH_4. We have previously shown that high-quality Si NCs can be produced by using $SiCl_4$-based nonthermal plasma[16-17]. The employment of these Si NCs from $SiCl_4$-based plasma on Si NCs/polymer hybrid solar cells leads to reduced cost and improved performance, signifying the advantages of Si NCs on hybrid solar cells[18]. However, question still remains whether toxic and expensive dopant precursors (PH_3, B_2H_6 et al.) can also be substituted by less toxic and more economical ones. In this context, organic dopant precursors may be well positioned because they are usually safe and economical[19-20]. However, the fact that dopant and carbon (C) are both contained in organic dopant precursor gives rise to other questions. Will the use of organic dopant precursor change

the crystalline structure and surface chemistry of Si NCs? Will C be unintentionally introduced into Si NCs when organic dopant precursor is used? If Si NCs are indeed doped by using organic dopant precursor, are the dopants electrically activated in Si NCs?

In this chapter, we address the above-mentioned important questions and carry out the first studies of doping Si NCs by using organic dopant precursor through a $SiCl_4$-based high frequency nonthermal plasma. Of all dopants in Si, P is one of the most employed. Therefore, trimethyl phosphite (TMP, $P(OCH_3)_3$) is selected as a model organic dopant precursor to synthesize P-doped Si NCs. Additionally, it is known that organic/inorganic hybrid photovoltaics exhibit great advantages of synthetic variability, light weight, clean, flexible, and low cost roll to roll fabrication process. Given the abundanance and nontoxicity of Si, we investigate Si NCs/polymer hybrid photovolatics by using these lost-cost synthesized Si NCs.

5.3 Experimental Methods

The $SiCl_4$-based nonthermal plasma employed to synthesize undoped Si NCs was realized by introducing $SiCl_4$, Ar and H_2 into the plasma system, respectively. The dopant precursor (TMP) was carried into the plasma system by Ar, resulting in P-doped Si NCs. In principle, the P concentration in Si NCs is determined by the ratio (R_p) of flow rate of TMP to that of $SiCl_4$, which is also adopted to label the samples. The flow rate of TMP was adjusted in the range from 0 to 200 standard cubic centimeters per minute (sccm), while that of $SiCl_4$ or H_2 was maintained at 2 or 40 sccm. The total flow rates for both undoped and P-doped Si NCs were fixed at 700 sccm, leading to a pressure of 400 Pa. We should point out that the flow rate of TMP recorded by the mass flow controller includes the flow rate of the carrier gas (Ar). The power coupled into

the plasma for both undoped and P-doped Si NCs were about 200 W. Transmission electron microscopy (TEM) (FEI Tecnai G2 F20 S-TWIN) and Raman scattering measurement (Seki Technotron STR750) were employed to characterize the crystalline structure of undoped and P-doped Si NCs. X-ray photoelectron spectroscopy (XPS) (Kratos AXIS Ultra DLD) was used to study the chemical composition of all Si NCs. The location and electrical activity of P in Si NCs was investigated by electron spin resonance (ESR) (JEOL RE-3X). Fourier Transform infrared (FTIR) microscopy (JASCO, 6100) was used to examine the surface chemistry of all Si NCs.

For fabricating solar cells, all Si NCs were etched in air for 24 h to remove surface chlorine by hydrofluoric acid (HF) vapor. After etching Si NCs were transfered immediately into a N_2 purged glovebox. Blend of Si NCs/ polythieno[3,4-b]-thiophene-co-benzodithiophene (PTB7) with a concentration of 20 mg/mL was prepared in chlorobenzene.

Commercial ITO glass with sheet resistance of 15 Ω/□ and thickness of 250 nm was used as the substrate. The ITO electrodes were patterned by using photolithography. (poly (3,4-ethylenedioxylenethiophene):poly (styrenesulphonic acid)) (PEDOT:PSS, CLEVIOS PH 1000, Heraeus) was spin cast on the patterned ITO substrate at 4000 rpm for 1 min. Si NC/polymer blend solutions were stirred for 24 h and then spin-coated on PEDOT:PSS layer at 1200 round per minute (rpm). Finally, Al electrode with thickness of 100 nm was evaporated through a shadow mask (active area 4.6 mm^2). Photocurrent density–voltage (J–V) curves were measured with a Keithley 2400 Digital Source Meter. Incident light density is checked before every measurement by using a standard silicon photodiode.

5.4 Results and Discussion

5.4.1 TMP-Enabled Doping of Si NCs

The structure properties of undoped Si NCs and P-doped Si NCs with various P concentrations are first characterized by transmission electron microscopy (TEM) and Raman scattering measurement. Figure 1a, b, and c representatively show the TEM results of P-doped Si NCs with the highest P concentration (R_p: 100) in this work. The low-resolution TEM image (Figure 5.1(a)) suggests ~ 8 nm sphere-like P-doped Si NCs are synthesized. We do not see significant change of NC size when Si NCs are undoped. The diamond structure of P-doped Si NCs is evidenced by the poly-crystalline diffraction rings in the selective area energy diffraction (SAED) image (Figure 5.1(b)). The high-resolution TEM image clearly shows the lattice fringe of a P-doped Si NC (Figure 5.1(c)). The lattice spacing obtained from Figure 5.1(c) is 0.314 nm, coinciding with that of the (111) plane of a Si crystal well. This implies that the P-doping hardly changes the lattice spacing because the size of a P atom is similar to that of a Si atom. Figure 5.1(d) shows the Raman spectra of undoped and P-doped Si NCs (R_p: 100). The typical first order vibration mode of the Si-Si bond in a Si crystal locating at about 520 cm^{-1} is highlighted in both undoped and P-doped Si NCs. It is found that the Raman spectra in the range below 600 cm^{-1} can be well-fitted by four peaks (inset of Figure 5.1(d)), which are located at about 300, 380, 480 and 520 cm^{-1}. Among these four peaks, the peaks at 300, 380 and 480 cm^{-1} are related to longitudinal acoustic (LA), longitudinal optical (LO) and transverse optical (TO_1) modes of the amorphous Si, respectively, while the peak at about 520 cm^{-1} is from the transverse optical (TO_2) mode of the Si crystal[21]. It is seen that the vibration modes of the amorphous Si slightly increases in P-doped Si NCs. This may be due to the incorporation of dopants into Si NCs[21]. In addition, another peak at about 950 cm^{-1} is observed in both undoped and P-doped Si NCs, which is the characteristic of the second order vibration mode of the Si-Si bond in a Si crystal[22]. Clearly, no

C-related vibration modes are found in the Raman spectrum of P-doped Si NCs. This implies that negligible C has been unintentionally introduced into P-doped Si NCs.

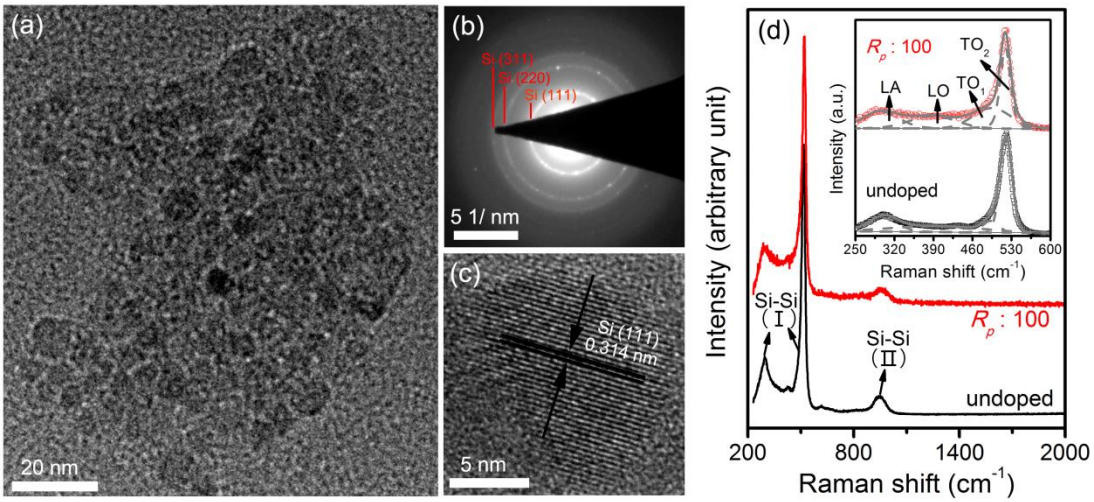

Figure 5.1. (a) Low magnification transmission electron microscopy (TEM) image of P-doped Si NCs. (b) Corresponding selected area electron diffraction (SAED) image of P-doped Si NCs. (c) High magnification TEM image of a P-doped Si NC. The ratio of flow rate of TMP to that of $SiCl_4$ (R_p) is 100 for P-doped Si NCs. (d) Raman spectra of undoped and P-doped Si NCs (R_p: 100). Inset shows the fitted Raman spectra of undoped and P-doped Si NCs. Both undoped and P-doped Si NCs are fitted by four peaks, which are located at about 300, 380, 480 and 520 cm^{-1}, respectively.

Evidence for doping P into Si NCs can be obtained by analyzing the chemical composition of P-doped Si NCs. Figure 5.2 shows the XPS results of undoped and P-doped Si NCs (R_p: 20 and R_p: 100) after they are exposed to air for 6 days. All the spectra have been calibrated by the C 1s peak at 284.5 eV. Figure 5.2(a) shows the high resolution P 2p spectra of undoped and P-doped Si NCs. It is seen clearly that no peaks related to P present in undoped Si NCs. While in P-doped Si NCs, a much prominent peak at about 129 eV ascribed to the P-Si bond is observed.

This peak increases and broadens as the P concentration increases. Additionally, an unconspicuous peak at about 135 eV due to the P-O bond is also found in P-doped Si NCs. The P-O bond is much less pronounced than the P-Si bond, though the Si NCs have been oxidized in air for 6 days. The observed P-Si bond suggests that there are P atoms being doped into Si NCs. We can estimate the P concentration of Si NCs by integrating the P-related peak intensity and Si-related peak intensity in conjunction with the atom-specific relative sensitivity factor. The P concentrations are calculated to be about 6 at. % for the R_p: 20 sample and 10 at. % for the R_p: 100 sample, respectively.

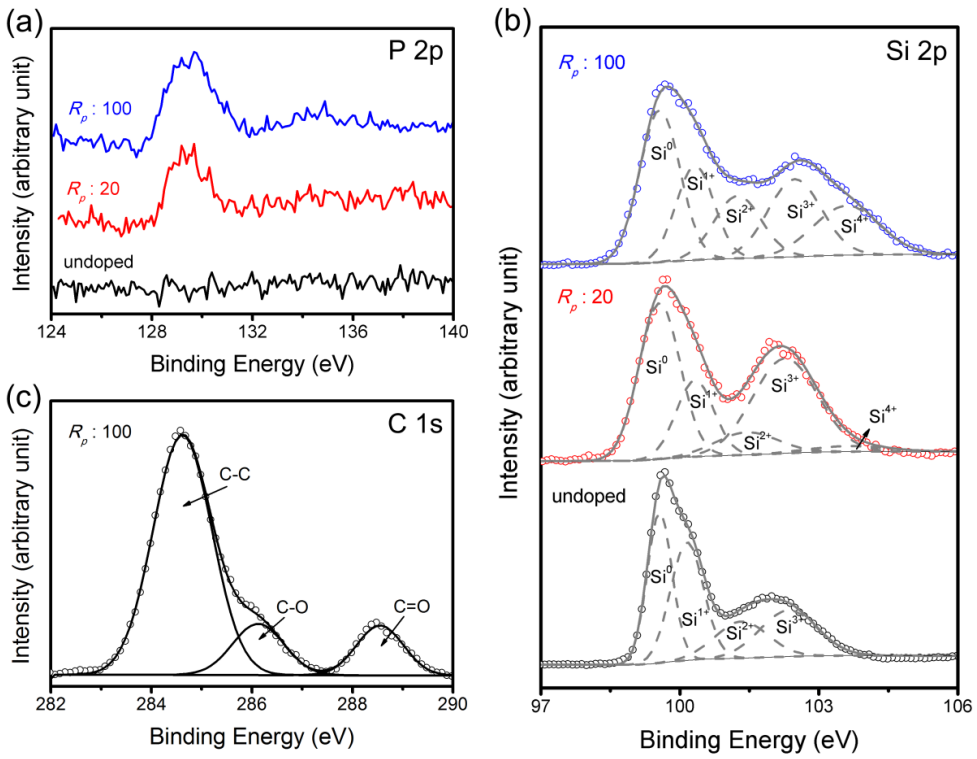

Figure 5.2. (a) Si 2p and (b) P 2p XPS spectra of undoped and P-doped Si NCs. The ratio of flow rate of TMP to that of $SiCl_4$ (R_p) are 20 and 100 for P-doped Si NCs. (c) C 1s XPS spectrum of P-doped Si NCs (R_p : 100). XPS measurements are carried out after Si NCs are exposed to air for 6 days.

The effect of P-doping on the chemical structure of Si NCs in terms of oxidation can also be investigated by XPS. Figure 5.2(b) shows the high resolution Si 2p spectra of undoped and P-doped Si NCs. The Si 2p spectrum of undoped Si NCs is decomposed into four constituent peaks related to the neutral state (Si^0) and three oxidation states in Si (Si^{1+}, Si^{2+}, Si^{3+}). While the Si 2p spectra of P-doped Si NCs are fitted by the abovementioned four peaks together with a fifth peak correlates to the highest oxidation state in Si (Si^{4+}). The peak position of Si^{1+}, Si^{2+}, Si^{3+} and Si^{4+} are fixed at about 0.95, 1.75, 2.48 and 3.9 eV above Si^0, respectively[23]. The atomic fraction (N) of each Si state can be obtained by integrating the corresponding peak intensity. We can work out the ratio of O to Si within the XPS detection depth by

$$\mathrm{O/Si} = \sum_{i=0}^{4} i\, N_{\mathrm{Si}^{i+}} \,/\, 2\sum_{i=0}^{4} N_{\mathrm{Si}^{i+}}, \qquad (5.1)$$

where $N_{\mathrm{Si}^{i+}}$ is the atomic fraction of Si^{i+}. The calculated values of O/Si for undoped Si-NC sample, the R_p: 20 sample and the R_p: 100 sample are 0.64, 0.75 and 0.87, respectively. The increase of O/Si with the P concentration clearly shows that the oxidation of Si NCs is indeed enhanced by P-doping. It is known that the oxidation of Si NCs follows the Cambrerra-Mott mechanism, in which the oxidation rate is correlated to the electron concentration of Si NCs[12, 14]. The increase of oxidation rate induced by P-doping suggests that the electron concentration of P-doped Si NCs is higher than that of undoped Si NCs. Therefore, we think that P has been electrically actively doped into Si NCs by using TMP.

Figure 5.2(c) shows the C 1s peak of Si NCs doped with the highest P concentration (R_p: 100). It is found that the C 1s peak can be well-fitted by three constituent peaks at 284.5, 286.2 and 288 eV. The main peak at 284.5 eV is due to the C-C bond caused by hydrocarbon surface contaminations. The other two peaks at 286.2 and 288 eV are assigned to C-O and C=O bond,

respectively. We do not observe C-Si bond (~ 283 eV) related peak in P-doped Si NCs, consistent with the conclusion drawn from the Raman results in Figure 5.1(d).

Figure 5.3 shows the ESR results of both undoped and P-doped Si NCs (R_p: 20 and R_p: 100). The ESR measurements were performed with an X-band ESR spectrometer at 300 K. It is seen that a single narrow resonance with a linewidth of about 1.5 mT at g=2.006 emerges in undoped Si NCs, due to the non-bonding electrons on the three-coordinated Si atoms, named Si dangling bonds at the NC surface[7]. For the R_p: 20 sample, there are two resonances arising in the ESR spectrum. These two resonances can be separated by simulating the ESR spectra. The obtained g-values of these two resonances from the simulating are 2.006 and 1.998, respectively. The g=2.006 resonance is also due to the Si dangling bonds at the surface of Si NCs, while the new broad g=1.998 resonance is a typical signal in P-doped Si NCs, originating from the exchange-coupled P atoms at the substitutional site of a Si-NC core[7]. The g=1.998 resonance has also been observed in intermediated and high P concentration doped bulk Si[24]. The linewidth of the P-induced resonance is about 8 mT, which is quite larger than that of the Si dangling bonds induced resonance. This broadening is consistent with the material doping, possibly generated by the spin-spin interactions between direct bonds of two or more closely-spaced P atoms at high P concentration. In the spectrum of the R_p: 100 sample, the P-induced broad resonance increases in intensity and dominates over the dangling bond induced resonance, similar to Stegner et al.'s observation on surface oxidized P-doped Si NCs[7]. The linewidth of the P-induced resonance slightly decreases from 8 mT to 6.5 mT as the concentration of P increases because of the formation of impurity band in P-doped Si NCs.[24] The same variation of linewidth has also been observed in P-doped bulk Si when the conduction electron concentration in Si is in the range of

10^{19} cm^{-3}.[24] Therefore, we conclude that the Si NCs are heavily doped by electrically activated P atoms.

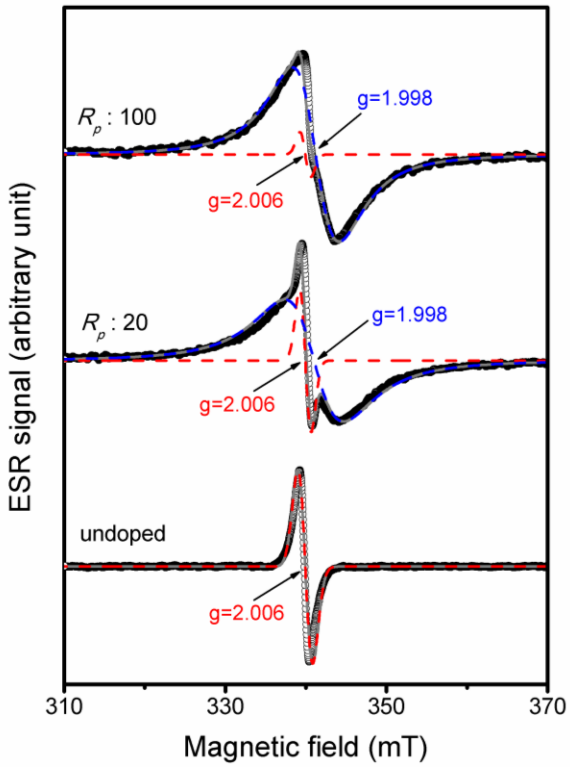

Figure 5.3. Electron spin resonance (ESR) spectrum obtained from undoped and P-doped Si NCs (black open dots) and simulated spectrum (grey solid lines) consist of two resonances at g=2.006 (red dotted line) and g=1.998 (blue dotted line). The ratio of flow rate of TMP to that of $SiCl_4$ (R_p) are 20 and 100 for P-doped Si NCs. ESR measurements are performed at room temperature and all NCs are measured without exposure to air.

In order to determine if the use of TMP leads to any change of the surface chemistry of Si NCs, both undoped Si NCs and Si NCs doped with the highest P concentration (R_p: 100) are examined by FTIR spectroscopy. The FTIR spectroscopy measurements were performed on the Si-NC film casted from the suspension formed by dispersing dry Si-NC powder in

chlorobenzene. Figure 5.4 shows the obtained FTIR spectra of undoped and P-doped Si NCs. The most notable peaks arising in all spectra are basically related to Si with H, Cl and O bonds. The FTIR spectrum of as-synthesized undoped Si NCs in Figure 5.4(a) clearly shows the absorption band of Si-Cl_x bonds at ~ 560 cm^{-1} and that of Si-Si-H_x bonds at ~ 860 and 2100 cm^{-1}.[16] This is rational giving the synthesis method in a $SiCl_4/H_2$ plasma. Besides, a prominent Si-O-Si absorption band at ~ 1050 cm^{-1} and a small O-Si-H_x absorption band at ~ 2250 cm^{-1} are also found in the spectrum.[16] The arising of O-related absorption for Si NCs without exposure to air may be due to residual moisture or contamination from etching of the quartz reactor wall.[16] Small absorption bands of C-H_x at ~ 2930 cm^{-1} are typically from the residual ligands at the surface of Si NCs[15] as they are not observed in the FTIR spectrum of dry Si-NC powders.

Figure 5.4(b) shows the FTIR spectrum of as- synthesized P-doped Si NCs (Rp: 20). The remarkable difference is the increase of the Si-Si-H_x peak at ~ 860 cm^{-1}. The Si-Si-H_x peak at ~ 2100 cm^{-1} also slightly increases. Both the Si-Cl_x and Si-O-Si peak remain unchanged. This suggests the Si-H bond density at the surface of Si NCs is increased by using TMP. Figure 5.4(c) shows the spectrum of as-synthesized P-doped Si NCs (Rp: 100). A further increase of the Si-Si-H_x peak at 860 cm^{-1} is observed as the P concentration increases. After the same R_p: 100 sample is shortly exposed to air for 3 min, a broad O-H peak[16] appears at ~ 3300 cm^{-1} and both the Si-O-Si peak and the O-Si-H_x peak increase clearly, as shown in Figure 5.4(d). However, the Si-Cl_x peak disappears definitely. It looks that the surface Cl of Si NCs can be quickly removed by oxidation. Figure 5.4(e) shows the FTIR spectrum after P-doped Si NCs are dry-etched by HF vapor in air for 5 h. It is seen that the Si-O-Si peak decreases significantly and the O-Si-H_x peak is hardly identified. By contrast, the Si-Si-H_x peaks increase. The weak Si-O-Si peak after etching the surface oxides indicates that little oxygen from TMP is incorporated into Si NCs.

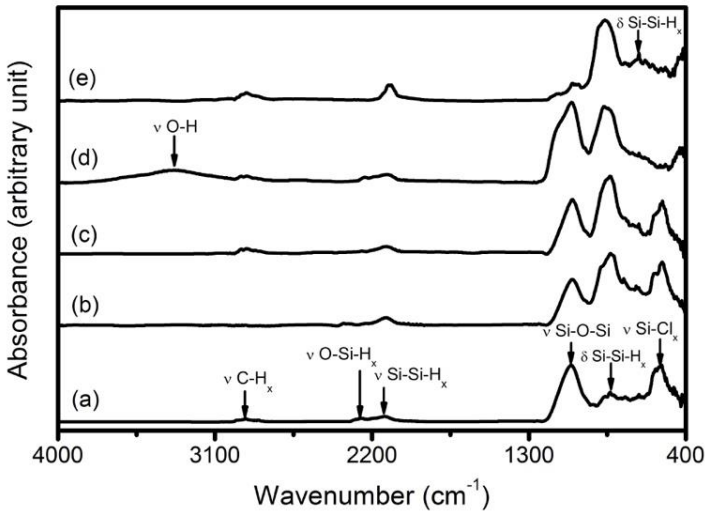

Figure 5.4. FTIR spectra for (a) as-synthesized undoped Si NCs, (b) as-synthesized P-doped Si NCs (R_p: 20), (c) as-synthesized P-doped Si NCs (R_p: 100), (d) P-doped Si NCs (R_p: 100) after exposed to air for 3 min, and (e) P-doped Si NCs (R_p: 100) after HF vapor etching for 5 h.

Previous investigation on the thermal stability of TMP by Holber et al.[25] shows that the decomposition of TMP gives atomic P and gaseous CO and H_2 via a methoxy (OCH_3) intermediate. This quite agrees with our XPS results in Figure 5.2(a). We find that the TMP-enabled P-doping of Si NCs can be well-understood by assuming a similar decomposition of TMP in the plasma. The atomic P from the decomposition of TMP is adsorbed onto the surface of Si NCs through collision, leading to the doping of Si NCs.[14] The further decomposition of methoxy shall increase the atomic H density in the plasma. It turns out that the Si-H bond density at the surface of P-doped Si NCs is augmented.[26] Due to the volatilization of CO, unintentional impurities such as C contained in TMP are not introduced into Si NCs. We believe that the current finding on TMP-enabled P-doping of Si NCs will open up possibilities for the use of other organic dopant precursors in doping Si NCs.

5.4.2 Si NCs/Polymer Hybrid Photovoltaics

In this section we investgate Si NCs/PTB7 hybrid solar cells because PTB7 is one of the most promising and widely studied donor materials and well-studied in our group. Figure 5.5(a) shows the TEM image of an undoped Si NC after the HF etching. The size of Si NC obtained from the TEM image is ~ 6 nm, indicating ~ 1 nm thick silicon oxides have been removed during the etching. The chemical structure of PTB7 is shown in Figure 5.5(b). The dispersing of PTB7 in selected solvent such as chloribenzen gives optical transparent colloid, as shown in Figure 5.5(c). Therefore, chloribenzen is also employed as the solvent for preparing blend of Si NCs/PTB7. Figure 5.5(d) representatively shows the optical absorption of Si NCs, PTB7 and Si NCs/PTB7 blend. It is clear that Si NC/PTB7 blend displays combined optical absorption of both the Si NCs and PTB7 in the range of 300–800 nm over a large part of the solar spectrum, which is demanded for high photocurrents. The hybrid solar cell is fabricated via a layer-by-layer solution process. The configuration of the solar cell is shown in Figure 5.5(e), whch can also be seen in the corresponding cross-sectional TEM image in Figure 5.5(f). The average thickness of the PEDOT:PSS (hole transportation layer), Si NCs/PTB7 (active layer) and Al electrode are ~ 30 nm, 70 nm and 40 nm, respectively. Figure 5.5(g) shows the J-V characteristic of the hybrid solar cell under dark condition and AM1.5 one sun illumination (100 mW/cm^2). The solar cell shows a short-circuit current density (J_{sc}) of 8 mA/cm^2, an open-circuit voltage (V_{oc}) of 0.55 V, a fill factor (FF) of 33%, resulting in a conversion efficiency (PCE) of 1.51% at 100 mW/cm^2 under 1 sun illumination.

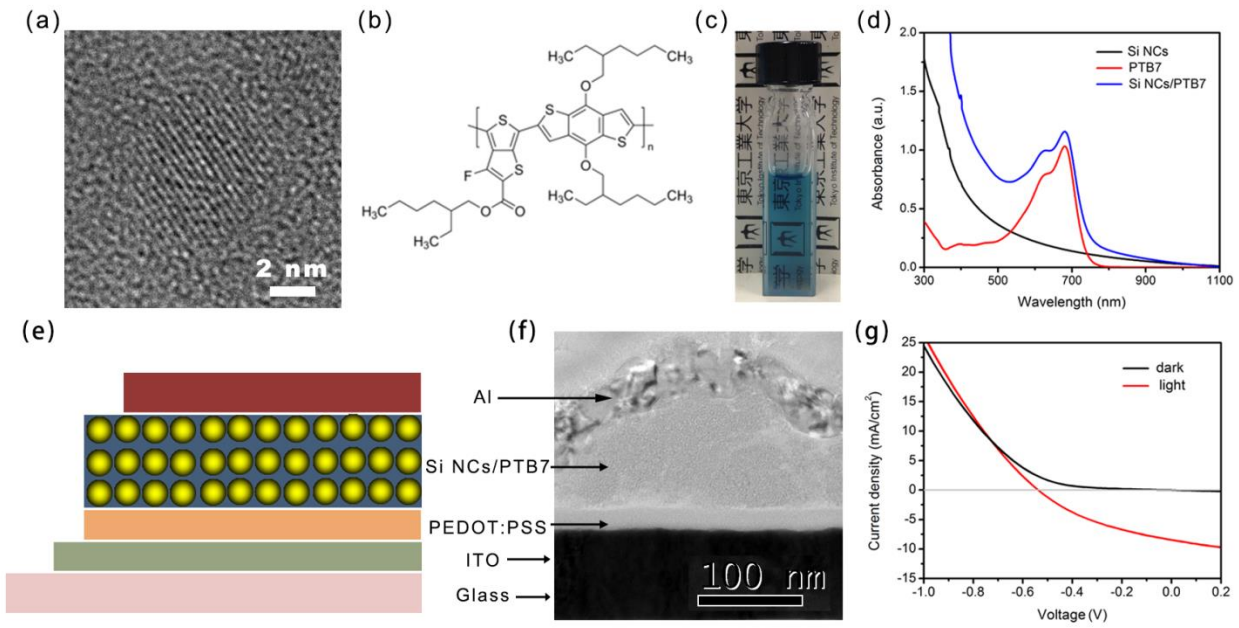

Figure 5.5. (a) TEM image of an undoped Si NC. (b) Chemical strcuture of PTB7. (c) Photograph of PTB7 colloid in CB. (d) UV-vis absortion spetra of Si NCs, PTB7 and Si NCs/PTB7 blend. (e) Configuration of the Si NCs/PTB7 hybrid solar cell. (f) Cross-sectional TEM image of a Si NCs/PTB7 hybrid solar cell structure. (g) J-V characterisics of a Si NCs/PTB7 bybrid solar cell in dark and under 1 sun illumination.

We have studied the influence of light illumination on the solar cell performance. Figure 5.6 typically shows the current density-voltage (J-V) characterisics of a Si NCs/PTB7 bybrid solar cell under 0.5, 1, and 2 sun illumination, respectively. It is seen that as the light illumination increaes from 0.5 sun to 1 sun, and to 2 sun, the J_{sc} increases from 5 to 8, and to 14 mA/cm^2, respectively. However, the V_{oc} just increases from 0.53 to 0.55, and to 0.57 V.

The J_{sc}, V_{oc}, FF and PCE under AM 1.5 at a variety of calibrated intensities ranging from 50 to 200 mW/cm^2 are summarized in Figure 5.7. Both the J_{sc} and V_{oc} increases linearly as the light intensity increases. This is quite similar to the result obtained in all polymer bulk-heterojunction

solar cells.[27] Such a linear dependence indicates that charge-carrier losses in the absorber bulk are mainly due to limited charge transport properties caused by trapping-induced recombination.[28] In contrast to J_{sc} and V_{oc}, FF decreases with the increase of the light intensity. It is known that FF is related to both R_s (series resistance) and R_{sh} (shunt resistance) in a complex way.[29] We have found that both R_s and R_{sh} drop significantly at higher light intensity,. The change of R_s and R_{sh} is essentially in agreement with the decrease of FF at higher light intensity. The efficiency of hybrid solar cell decreases as the light intensity increases. This indicates both R_s and R_{sh} influence the efficiency of our devices negatively.

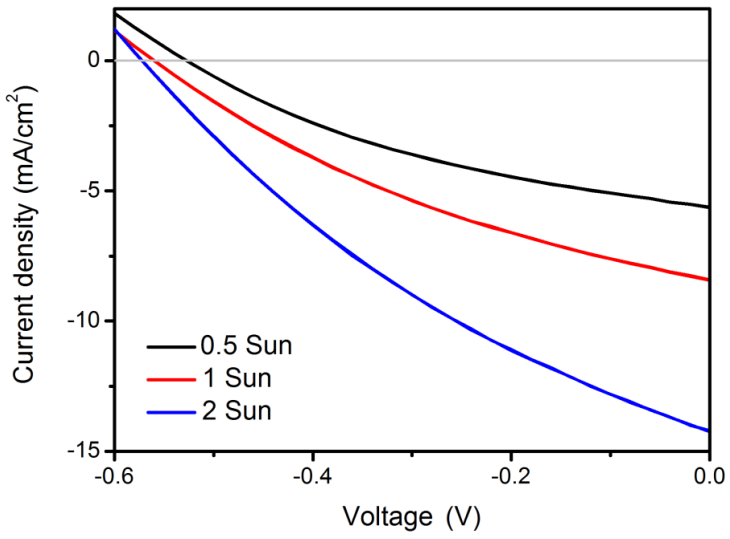

Figure 5.6. I-V characteristics of a Si NCs/PTB7 bybrid solar cell under 0.5, 1, and 2 sun illumination, respectively.

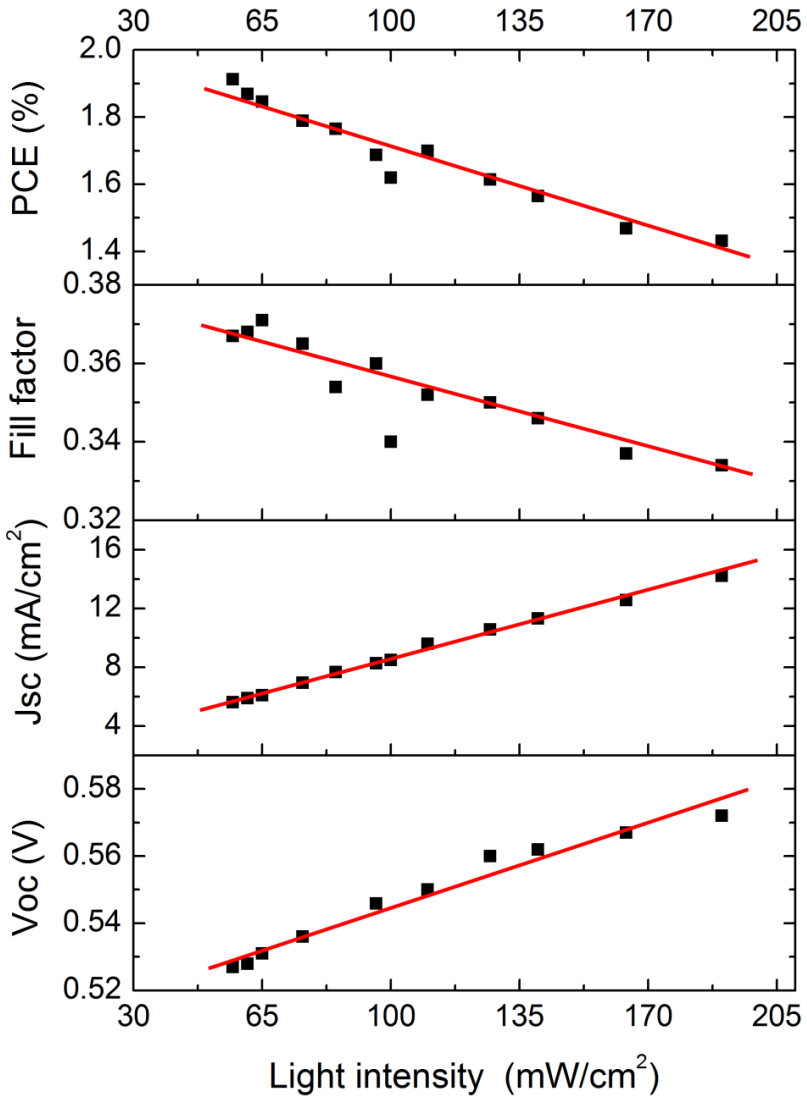

Figure 5.7. Dependence of the Voc, Jsc, FF, and PCE of a Si NCs/PTB7 hybrid solar cell on the light intensity. The red line gives the linear fit for each plot.

We have also carried out the research of P-doped Si NCs in hybrid solar cells. Figure 5.8(a) shows the I-V results of the solar cells by using Si NCs with various P concentrations. It is seen that the V_{oc} slightly increases from 0.55 to 0.57 V when Si NCs are doped with P (R_p:20). The actual increase of V_{oc} is possibly due to the move of Fermi level towards the conduction band

caused by P-doping. However, the PCE decreases from 1.2% to 0.7% because of the more pronounced drop of J_{sc} from 7 to 3 mA/cm^2. As the P concentration increases to R_p:100, both the V_{oc} and J_{sc} remarkablely decrease, resulting in a further dramatical drop of the PCE. This means the P donor gives rise to strong recombination of charged carriers generated in the bulk absorber. Similar results could also be obtained by studying the influence of P-doping on the photoluminescence (PL) of Si NCs. More than one order of magnitude drop of the PL intensity is observed after the P-doping in Figure 5.8(b). Clearly, it is the P-doping induced recombination quenching the PL as well as the photocurrent in solar cells.

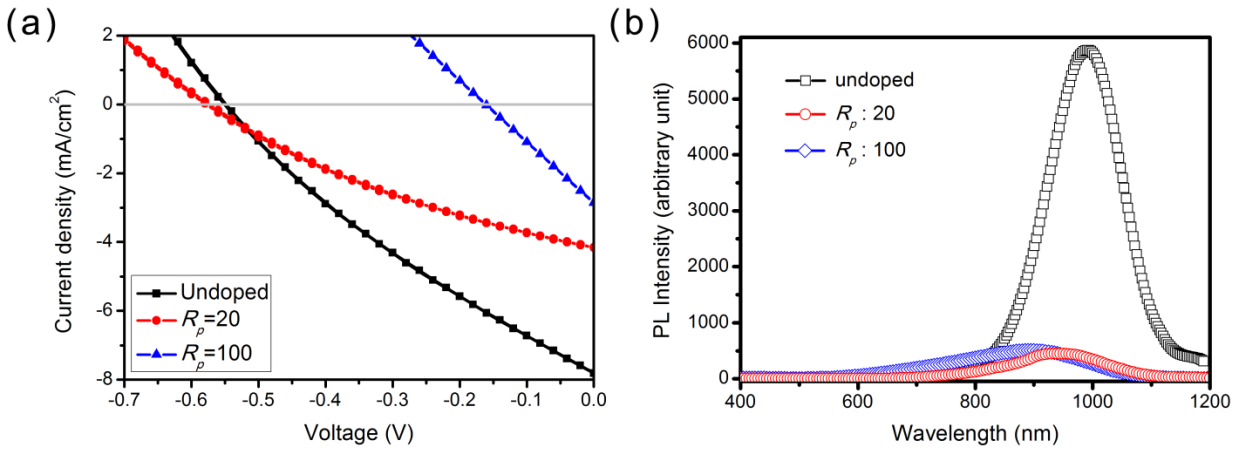

Figure 5.8. (a) I-V characterisics of undoped Si NCs/PTB7 and P-doped Si NCs/PTB7 hybrid solar cells. (b) PL spectra of undoped and P-doped Si NCs. The ratio of flow rate of TMP to that of $SiCl_4$ (R_p) are 20 and 100 for P-doped Si NCs.

5.5 Conclusions

In summary, we have successfully doped P into the substitutional site of Si NCs by using novel organic dopant precursor (TMP) through a $SiCl_4$-based high frequency nonthermal plasma. We find that the TMP-enabled P-doping does not change the crystallinity of Si NCs. The

diamond structure of Si NCs remains. Unintentional impurities such as carbon contained in TMP are not introduced into Si NCs. The surface of P-doped Si NCs is found to be terminated by both Cl and H. The use of TMP leads to increased Si-H bond density at the surface of Si NCs, while the surface Si-Cl bond density is hardly changed. The enhanced oxidation in XPS spectra and P-related ESR resonance suggest P atoms are electrically active in Si NCs. Organic/inorganic hybrid solar cells have been fabricated by using PTB7 and low-cost Si NCs synthesized from $SiCl_4$ and TMP. The P-doping can slightly enhance the V_{oc} at a low concentration. However, the strong recombination of charged carriers caused by trap states and donor impurities in Si NCs give rise to significant loss of photocurrent, resulting in degradation of the solar cell performance.

5.6 References

[1] Yu, X.; Chen, J.; Ma, X.; Yang, D. Impurity Engineering of Czochralski Silicon, *Mater. Sci. Eng., R* **2013**, *74*, 1-33.

[2] Soref, R. A. Silicon-Based Optoelectronics, *Proc. IEEE* **1993**, *81*, 1687-1706 (1993).

[3] Green, M. A. Recent Developments in Photovoltaics, *Solar Energy* **2004**, *76*, 3-8.

[4] Mimura, A.; Fujii, M.; Hayashi, S.; Kovalev, D.; Koch, F. Photoluminescence and Free-Electron Absorption in Heavily Phosphorus-Doped Si Nanocrystals, *Phys. Rev. B* **2000**, *62*, 12625-12627.

[5] Fujio, K.; Fujii, M.; Sumida, K.; Hayashi, S.; Fujisawa, M.; Ohta, H. Electron Spin Resonance Studies of P and B Codoped Si Nanocrystals, *Appl. Phys. Lett.* **2008**, *93*, 021920.

[6] Sugimoto, H.; Fujii, M.; Imakita, K.; Hayashi, S.; Akamatsu, K. Phosphorus and Boron Codoped Colloidal Silicon Nanocrystals with Inorganic Atomic Ligands, *J. Phys. Chem. C* **2013**, *117*, 6807-6813.

[7] Stegner, A. R.; Pereira, R. N.; Klein, K.; Lechner, R.; Dietmueller, R.; Brandt, M. S.; Stutzmann, M.; Wiggers, H. Electronic Transport in Phosphorus-Doped Silicon Nanocrystal Networks, *Phys. Rev. Lett.* **2008**, *100*, 026803.

[8] Stegner, A. R.; Pereira, R. N.; Lechner, R.; Klein, K.; Wiggers, H.; Stutzmann, M.; Brandt, M. S. Doping Efficiency in Freestanding Silicon Nanocrystals from the Gas Phase: Phosphorus Incorporation and Defect-Induced Compensation, *Phys. Rev. B* **2009**, *80*, 165326.

[9] Wolf, O.; Dasog, M.; Yang, Z.; Balberg, I.; Veinot, J. G. C.; Millo, O. Doping and Quantum Confinement Effects in Single Si Nanocrystals Observed by Scanning Tunneling Spectroscopy, *Nano Lett.* **2013**, *13*, 2516-2521.

[10] Gresback, R.; Kramer, N. J.; Ding, Y.; Chen, T.; Kortshagen, U. R.; Nozaki, T. Controlled Doping of Silicon Nanocrystals Investigated by Solution-Processed Field Effect Transistors, *ACS Nano* **2014**, *8*, 5650-5656.

[11] Mangolini, L.; Thimsen, E.; Kortshagen, U. High-Yield Plasma Synthesis of Luminescent Silicon Nanocrystals, *Nano Lett.* **2005**, *5*, 655-659.

[12] Pi, X. D.; Gresback, R.; Liptak, R. W.; Campbell, S. A.; Kortshagen, U. Doping Efficiency, Dopant Location, and Oxidation Of Si Nanocrystals, *Appl. Phys. Lett.* **2008**, *92*, 123102.

[13] Rowe, D. J.; Jeong, J. S.; Mkhoyan, K. A.; Kortshagen, U. R. Phosphorus-Doped Silicon Nanocrystals Exhibiting Mid-Infrared Localized Surface Plasmon Resonance, *Nano Lett.* **2013**, *13*, 1317-1322.

[14] Zhou, S.; Pi, X. D.; Ni, Z. Y.; Luan, Q. B.; Jiang, Y. Y.; Jin, C. H.; Nozaki, T.; Yang, D. Boron- and Phosphorus-Hyperdoped Silicon Nanocrystals, *Part. Part. Syst. Charact.* **2015**, *32*, 213-221.

[15] Zhou, S.; Pi, X. D.; Ni, Z. Y.; Ding, Y.; Delerue, C.; Yang, D.; Nozaki, T. Comparative Study on the Localized Surface PlasmonResonance of Boron- and Phosphorous-Doped Silicon Nanocrystals, *ACS Nano* **2015**, *9*, 378-386.

[16] Gresback, R.; Nozaki, T.; Okazaki, K. Synthesis and Oxidation of Luminescent Silicon Nanocrystals from Silicon Tetrachloride by Very High Frequency Nonthermal Plasma, *Nanotechnology* **2011**, *22*, 305605.

[17] Gresback, R.; Murakami, Y.; Ding, Y.; Yamada, R.; Okazaki, K.; Nozaki, T. Optical Extinction Spectra of Silicon Nanocrystals: Size Dependence upon the Lowest Direct Transition, *Langmuir* **2013**, *29*, 1802-1807.

[18] Ding, Y.; Gresback, R.; Liu, Q. M.; Zhou, S.; Pi, X. D.; Nozaki, T. Silicon Nanocrystal Conjugated Polymer Hybrid Solar Cells with Improved Performance, *Nano Energy* **2014**, *9*, 25-31.

[19] Neumayer, D. A.; Ekerdt, J. G. Growth of Group III Nitrides. a Review of Precursors and Techniques, *Chem. Mater.* **1996**, *8*, 9-25.

[20] Zanella, P.; Rossetto, G.; Brianese, N.; Ossola, F.; Porchia, M.; Williams, J. O. Organometallic Precursors in the Growth of Epitaxial Thin-Films of Groups III-V Semiconductors by Metal Organic-Chemical Vapor-Deposition, *Chem. Mater.* **1991**, *3*, 225-242.

[21] Li, K. H.; Shen, W. Z. Uniformity and Bandgap Engineering in Hydrogenated Nanocrystalline Silicon Thin Films by Phosphorus Doping for Solar Cell Application, *J. Appl. Phys.* **2009**, *106*, 063505.

[22] Parker, J. H.; Feldman, D. W.; Ashkin, M. Raman Scattering by Silicon and Germanium, *Phys. Rev.* **1967**, *155*, 712-714.

[23] Himpsel, F. J.; McFeely, F. R.; Talebibrahimi, A.; Yarmoff, J. A.; Hollinger, G. Microscopic Structure of the SiO_2/Si Interface, *Phys. Rev. B* **1988**, *38*, 6084-6096.

[24] Quirt, J. D.; Marko, J. R. Absolute Spin Susceptibilities and Other ESR Parameters of Heavily Doped n-Type Silicon. I. Metallic Samples, *Physical Review B* **1972**, *5*, 1716-1728.

[25] Holbert, A. W.; Batteas, J. D.; Wong-Foy, A.; Rufael, T. S.; Friend, C. M. Passivation of Fe(110) via Phosphorus Deposition: the Reactions of Trimethylphosphite, *Surf. Sci.* **1998**, *401*, L437-L443.

[26] Mangolini, L.; Kortshagen, U. Selective Nanoparticle Heating: Another Form of Nonequilibrium in Dusty Plasmas, *Phys. Rev. E* **2009**, *79*, 026405.

[27] Mandoc, M. M.; Veurman, W.; Koster, L. J. A.; de Boer, B.; Blom, P. W. M. Origin of the Reduced Fill Factor and Photocurrent in MDMO-PPV:PCNEPV All-Polymer Solar Cells, *Adv. Fun. Mater.* **2007**, *17*, 2167-2173.

[28] Gao, F.; Li, Z.; Wang, J.; Rao, A.; Howard, I. A.; Abrusci, A.; Massip, S.; McNeill, C. R.; Greenham, N. C. Trap-Induced Losses in Hybrid Photovoltaics, *ACS Nano* **2014**, *8*, 3213-3221.

[29] Riedel, I.; Parisi, J.; Dyakonov, V.; Lutsen, L.; Vanderzande, D.; Hummelen, J. C. Effect of Temperature and Illumination on the Electrical Characteristics of Polymer–Fullerene Bulk-Heterojunction Solar Cells, *Adv. Fun. Mater.* **2004**, *14*, 38-44.

Chapter 6: Conclusions and Outlook for Future Work

6.1 Conclusions

The thesis concentrates on freestanding B- and P-doped Si NCs that are synthesized by nonthermal plasma. Tunable dopant concentration in a fairly wide range is achieved by modulating the fractional flow rate of dopant precursor in the plasma. Understanding the incorporation of dopants as well as the dopant-supported novel properties is highlighted. We have studied the dopant concentration, dopant location, doping efficiency and doping mechanism in B- and P-doped Si NCs. The novel properties, especially the optical properties, enabled by B and P doping have been extensively investigated. The current work lays solid foundation for future applications based on doped Si NCs.

In chapter 2, we demonstrate that Si NCs can be hyperdoped with B and P to concentrations exceeding their solubility limit in Si by means of nonthermal plasma. Despite the hyperdoping the diamond structure of Si NCs remains without the introduction of new phases. There are both electrically active B and P in hyperdoped Si NCs. Importantly, we have answered the intriguing question why Si NCs can be hyperdoped. It is found that hyperdoping is in fact made possible mainly by the kinetics in the nonthermal plasma synthesis of Si NCs. The differences in the doping efficiency and dopant distribution between B and P can be understood by assuming that the doping of Si NCs is mainly controlled by kinetics, in which the collision between Si NCs and B/P atoms and the binding energy of B/P at the NC surface are critical.

In chapter 3, we experimentally show that mid-infared LSPR can be obtained from both B- and P-doped Si NCs. In addition to the demonstration of the LSPR of B-doped Si NCs for the first time, we have innovatively compared the LSPR between B- and P-doped Si NCs. The LSPR

energy of B-doped Si NCs is higher than that of P-doped Si NCs because B produces free carriers more efficiently than P. It is both experimentally and computationally shown that the so-called Drude model traditionally used to describe the LSPR of noble metal NCs also works for the LSPR of semiconductor NCs if the dielectric screening and carrier effective mass of semiconductor NCs are considered. Significantly, electronic properties such as dopant activation and free carrier behavior are elucidated by investigating the LSPR of doped Si NCs with the synergy of experiments and calculations. We clearly demonstrate that B-doped Si NCs are better positioned for the practical use of LSPR than P-doped Si NCs. This is an important step for advancing the Si-NC-based plasmonics.

In chapter 4, we highlight that the B heavydoping can provide both tunable plasmonic properties and colloidal stability for Si NCs in air, making them suitable for device processing in ambient atmosphere. The optical absorption of heavily B-doped Si NCs reveals that the heavy B doping not only changes the concentration of free carriers that are confined in Si NCs but also modifies the band structure of Si NCs. After heavy B doping both indirect and direct electronic transition energies remarkably decrease in Si NCs because the heavy B doping induced movement of the conduction band toward the band gap could be more significant than that of the Fermi level into the valence band. We propose that the LSPR of heavily B-doped Si NCs originates from free holes above the Fermi level, which are largely from the B-induced impurity band. Our results are important for the application of plasmonic Si NCs on advanced optoelectronics. On one hand, uniform and dense thin films with plasmonic properties can be inexpensively fabricated by using printing because of the capability of heavily B-doped Si NCs for wet-chemical processing. On another hand, the plasmonic and sub-interband absorption of Si

NCs enabled by heavy B doping is now located in the infrared regime, which should be helpful to the development of novel Si-based optoelectronic structures and devices.

In chapter 5, we have successfully doped P into the substitutional site of Si NCs by using novel organic dopant precursor (TMP) through a $SiCl_4$-based high frequency nonthermal plasma. The main concerns associated with the the quality of doped Si NCs (e.g. crystallinity, dopant electrical activity, surface chemistry, unintentional impurities et al.) which is critical for the applications on nano-devices have been addressed. It is found that the TMP-enabled P-doping does not change the crystallinity of Si NCs. The diamond structure of Si NCs remains. Unintentional impurities such as carbon contained in TMP are not introduced into Si NCs. The surface of P-doped Si NCs is found to be terminated by both Cl and H. The use of TMP leads to increased Si-H bond density at the surface of Si NCs, while the surface Si-Cl bond density is hardly changed. The enhanced oxidation in XPS spectra and P-related ESR resonance suggest P atoms are electrically active in Si NCs. Organic/inorganic hybrid solar cells have been fabricated by using PTB7 and low-cost Si NCs synthesized from $SiCl_4$ and TMP. It is found that P-doping can slightly enhance the V_{oc} at a low concentration because of the move of Fermi level towards conduction band. However, both trap states and donor impurities in Si NCs cause strong recombination of charged carriers generated in the bulk absorber, resulting in significant loss of photocurrent.

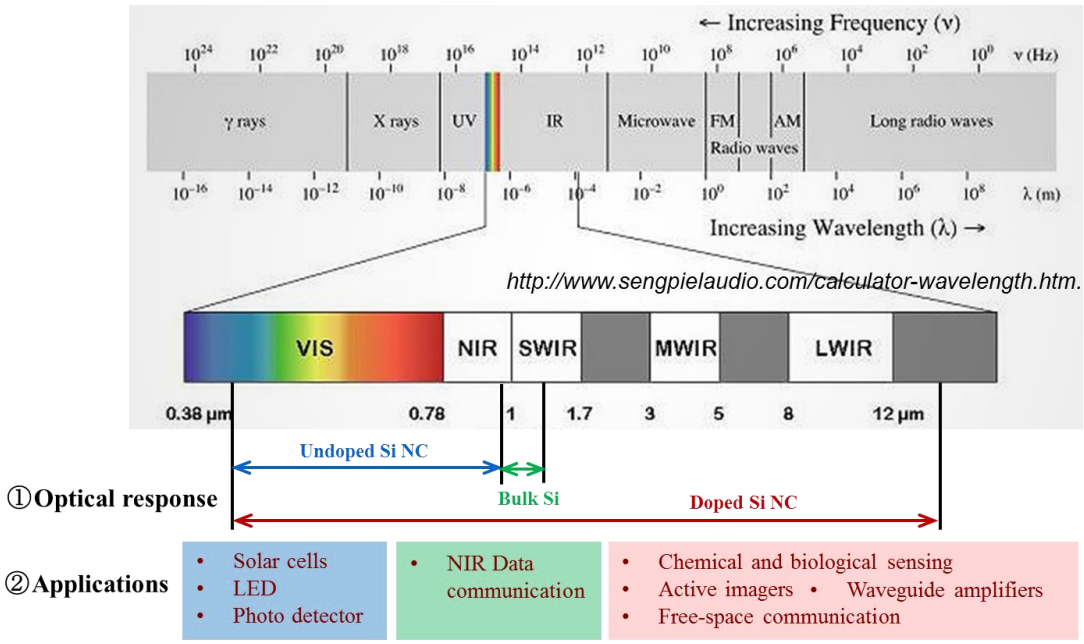

Figure 6.1. Optical responce of bulk Si, undoped Si NCs and doped Si NCs and correspoding poential applications in the visible, near-infrared and mid-infrared range.

6.2 Outlook for Future Work

Hyperdoping Si NCs with B and P has enabled distinct optical and electrical properties that intrinsic Si NCs do not possess. Clearly the observation of localized surface plasmon resonance in B- and P-doped Si NCs is one of the most intriguing things. In contrast to noble metal and metal oxide NCs the LSPR energies for doped Si NCs are all located in the mid-infrared region. Although integrated silicon photonic devices for near-IR data communications applications are well-known and are attracting great interest, its potential in the mid-IR region has so far remained unexplored. There are many potential applications for silicon photonics in the mid-IR range such as chemical and biological sensing, waveguide amplifiers, active imagers, laser radar transceivers, multiwavelength light sources and invisible-fence alarm systems, as well as

free-space communications.[1] Applications of plasmonic Si NCs in these areas are worth exploring in the future.

In addition, effort to move the LSPR energy of doped Si NCs towards the visible region is needed. It is known that the activation efficiencies of B and P in Si NCs are currently low (1%~6% for B and 0.1%~0.9% for P). This means a great deal of dopants in Si NCs is deactivated and unable to produce free carriers. Mechanism that deactivates the dopant in Si NCs is complex and currently not so clear. If this part of dopants can be activated, the free carrier concentration should be significantly improved, giving rise to shift of LSPR energy towards near-infrared or visible region.

Metal-insulator transition (MIT) has been proved to occur to P-doped Si NCs films at a critical concentration higher than 10^{20} cm^{-3}.[2] Because B can more efficiently produce free carriers than P in Si NCs, it is reasonable that metal-insulator transition also occurs to B-doped Si NCs. Besides, the excellent dispersity of B-doped Si NCs in polar solvent facilitates the fabrication of high quality NC films which is critical for carrier transport. Therefore, it is believed that MIT occurs to B-doped Si NCs much easier than P-doped Si NCs. Further study needs to be carried out to clarify this point.

Additionally, it has been reported in bulk Si that superconductivity can be induced when boron is locally introduced into silicon at concentrations above its equilibrium solubility.[3] In this thesis we have shown in nanoscale form of Si that Si NCs can be doped with even higher concentrations of B or P. Despite the sufficient high dopant concentration, another main challenge to obtain nanostructured superconductor is to create a well electrically coupled NC solid.[4] Generaly, most solids are assembled from colloidal NCs that are insulated from each other

by organic ligands. Hovever, thanks to the excellent colloidal stability enabled by heavy B doping, this has readily been confronted in Si NC solid without the use of ligands. Therefore, it is highly expected that superconductivity arises at a higher transition temperature in Si NC solids after heavy B doping.

It is now clear that there is a great deal of dopants being introduced into Si NCs. However, the direct observation of the exact location of these dopants in Si NCs is still lacking. The knowledge of the location of these dopants is critical for the understanding of doping mechanism in the nanometer-sized scale. Current techniques such as in situ TEM, atom probe tomography (APT), annular-dark-field scanning transmission electron microscopes (ADF-STEM) and electron energy-loss spectrum (EELS) enable dynamic processes involving direct observation and characterization of individual impurity atoms and impurity distributions within semiconductor nanostructures.[5] As research on impurity incorporation in Si NCs continues to advance, it becomes increasing important to imgaing the location and distribution of dopant in heavily-doped Si NCs directly.

The performance of Si NCs/polymer hybrid photovoltaics is not so high at this moment. It is believed that defects such as dangling bonds are typical roadblocks to high-efficieny photovoltaics. Pursue of defect-free Si NCs for a variety of devices including photodiodes, transistors and photovoltaics will not stop. Introduce of plasmonic structure would be another promising route to solution-processed devices such as organic-inorganic hybrid solar cells.[6]

6.3 References

[1] Soref, R. Mid-infrared Photonics in Silicon and Germanium. *Nat. Photon.* **2010**, *4*, 495-497.

[2] Chen, T.; Reich, K. V.; Kramer, N. J.; Han, F.; Kortshagen, U.; Shklovskii, B. I. Metal–insulator transition in films of dopedsemiconductor nanocrystals. *Nat. Mater.* **2016**, *15*, 299-303.

[3] Bustarret, E.; Marcenat, C.; Achatz, P.; Kacmarcik, J.; Levy, F.; Huxley, A.; Ortega, L.; Bourgeois, E.; Blase, X.; Debarre, D.; Boulmer, J. Superconductivity in Doped Cubic Silicon. *Nature* **2006**, *444*, 465-468.

[4] Pavlo, Z.; Philippe, G. Superconductivity in Films of Pb/PbSe Core/Shell Nanocrystals, *ACS Nano* **2012**, *6*, 8094-8104.

[5] Holmberg, V. C.; Helps, J. R.; Mkhoyan, K. A.; Norris, D. J. Imaging Impurities in Semiconductor Nanostructures, *Chem. Mater.* **2013**, *25*, 1332-1350.

[6] Arinze, E. S.; Qiu, B.; Nyirjesy, G.; Thon, S. M. Plasmonic Nanoparticle Enhancement of Solution-Processed Solar Cells: Practical Limits and Opportunities, *ACS Photonics* **2016**, *3*, 158-173.

Appendix

A.1 Summary of characterization methods

Table A.1 Summary of characterization methods.

Charaterization technique	Instruments	Details
Transmission electron microscopy (TEM)	FEI Tecnai G2 F20 S-TWIN	pp 22,50,86,115
High-angle annular dark field (HAADF)	FEI Titan G2 80-200 w/ Chemi STEM	pp 22,50,86
X-ray diffraction (XRD)	X'Pert PRO	pp 22,51
Raman spectroscopy	Senterra BRUKER	pp 22,51
X-ray photoelectron spectroscopy (XPS)	Kratos AXIS Ultra DLD	pp 22,51,87,115
Chemical titration	-	pp 21,50,86
Fourier transform infrared (FTIR) spectroscopy	JASCO FT/IR-6100	pp 51,87,115
Zeta-potential	Zetasizer Nano-ZS (Malvern Instrument)	pp 87
Ultra-violet photoelectron spectroscopy (UPS)	Kratos AXIS Ultra DLD	pp 87
Scanning electron microscopy (SEM)	Hitachi S4000	pp 87
Atomic force microscopy (AFM)	Shimadzu SPM-9600	pp 87
UV-VIS spectroscopy	Shimadzu UV-2000	pp 87
Electron spin resonance (ESR)	JEOL RE-3X	pp 115

Photocurrent density–voltage (J–V) measurement	Keithley 2400 Digital Source Meter	pp 115

A.2 Theoretical current density

We can estimate the current density from the solar spectrum and the external quantum efficiency (EQE) as follows:

We first write

$$\text{Solar irradiation} = f(\lambda) \ , \tag{A.1}$$

$$\text{EQE} = g(\lambda) \ , \tag{A.2}$$

where λ is the wavelength.

Then the current density generated in the solar cell can be expressed as

$$\text{Current density} = \text{EQE} \times (\text{Total power of photons/ Energy of one photon})$$

$$= g(\lambda) \times \int \frac{f(\lambda) e d\lambda}{h\nu/\lambda} \tag{A.3}$$

$$= \frac{e}{h\nu} \int f(\lambda) g(\lambda) \lambda d\lambda \tag{A.4}$$

where e is electron charge, h is planck constant, ν is the speed of light.

From the AM1.5 standard spectrum and EQE, we obtain the current density is ~10 mA/cm^2 for the current (Si NCs/PTB7) solar cell. If we assume the average EQE to be ~ 100%, the

theoretical current density could be increased to be ~ 20 mA/cm^2. This may be realized by optimizing the solar cell structure, optical gap of Si NCs and the polymer.

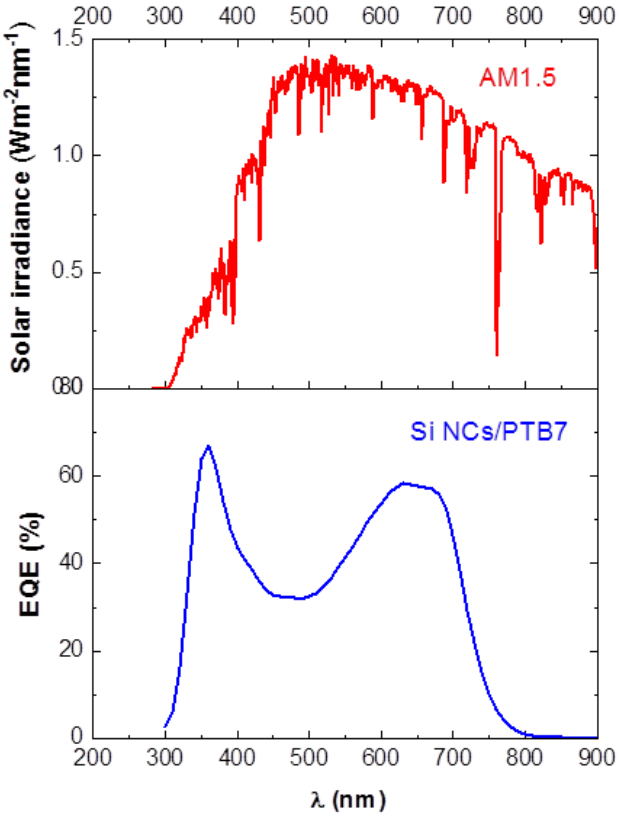

Figure A.1. AM1.5 standard solar spectrum and typical EQE spectrum of Si NCs/PTB7 hybrid solar cells.

A.3 Nonthermal plasma method

Table A.2 Advantages of nonthermal plasma method in the synthesis of Si NCs compared with other process.

	Wet chemistry[1-3]	Laser pyrolysis[4-5]	Sputtering[6-8]	Nonthermal plasma[9-12]
Size	1-100 nm	1-100 nm	1-50 nm	1-100 nm
Crystallinity	crystal/ amorphous	crystal/ amorphous	crystal/ amorphous	crystal/ amorphous
Surface chemistry	Yes	No	No	H/Cl
Doping	No	No	n/p type	n/p type
Production rate per hour	Milligram	Milligram	Milligram	Gram
Synthesis cycle	Long	-	-	< 1 h
Energy consuming	-	< 100 W	< 100 W	< 100 W
High temperature process	Yes	Yes	Yes	No

A.4 References

[1] Tilley, R. D.; Warner, J. H.; Yamamoto, K.; Matsui, I.; Fujimori, H. Micro-emulsion synthesis of monodisperse surface stabilized silicon nanocrystals. *Chem. Commu.* **2005**, 1833-1835.

[2] Bley, R. A.; Kauzlarich, S. M. A Low-Temperature Solution Phase Route for the Synthesis of Silicon Nanoclusters. *J. Am. Chem. Soc.* **1996**, *118*, 12461-12462.

[3] Holmes, J. D.; Ziegler, K. J.; Doty, R. C.; Pell, L. E.; Johnston, K. P.; Korgel, B. A. Highly Luminescent Silicon Nanocrystals with Discrete Optical Transitions. *J. Am. Chem. Soc.* **2001**, *123*, 3743-3748.

[4] Li, X. G.; He, Y. Q.; Talukdar, S. S.; Swihart, M. T. Process for Preparing Macroscopic Quantities of Brightly Photoluminescent Silicon Nanoparticles with Emission Spanning the Visible Spectrum. *Langmuir* **2003**, 19, 8490-8496.

[5] Li, X. G.; He, Y. Q.; Swihart, M. T. Surface Functionalization of Silicon Nanoparticles Produced by Laser-Driven Pyrolysis of Silane Followed by HF−HNO3 Etching. *Langmuir* **2004**, 20, 4720-4727.

[6] Fujii, M.; Toshikiyo, K.; Takase, Y.; Yamaguchi, Y.; Hayashi, S. Below Bulk-Band-Gap Photoluminescence at Room Temperature from Heavily P- and B-Doped Si Nanocrystals. *J. Appl. Phys.* **2003**, 94, 1990-1995.

[7] Mimura, A.; Fujii, M.; Hayashi, S.; Kovalev, D.; Koch, F. Photoluminescence and Free-Electron Absorption in Heavily Phosphorus-Doped Si Nanocrystals. *Phys. Rev. B* **2000**, 62, 12625-12627..

[8] Minoru, F.; Hiroshi, S.; Kenji, I. All-Inorganic Colloidal Silicon Nanocrystals-Surface Modification by Boron and Phosphorus Co-Doping. *Nanotechnology* **2016**, 27, 262001.

[9] Mangolini, L. Synthesis, Properties, and Applications of Silicon Nanocrystals. *J. Vac. Sci. Tech. B* **2013**, 31, 020801.

[10] Mangolini, L.; Thimsen, E.; Kortshagen, U. High-Yield Plasma Synthesis of Luminescent Silicon Nanocrystals. *Nano Lett.* **2005**, *5*, 655-659.

[11] Zhou, S.; Pi, X.; Ni, Z.; Luan, Q.; Jiang, Y.; Jin, C.; Nozaki, T.; Yang, D. Boron- and Phosphorus-Hyperdoped Silicon Nanocrystals. *Part. Part. Syst. Cha.* **2015**, 32, 213-221.

[12] Gresback, R.; Nozaki, T.; Okazaki, K. Synthesis and Oxidation of Luminescent Silicon Nanocrystals from Silicon Tetrachloride by Very High Frequency Nonthermal Plasma. *Nanotechnology* **2011**, 22, 305605.